

COPY

4

AD-A221 768

GL-TR-90-0062

Seismic Surveillance - Nuclear Test Ban Verification

Eystein S. Husebye
Bent O. Ruud

University of Oslo
Department of Geology
PO Box 1047 Blindern
N-0316 Oslo 3, Norway

26 February 1990

Scientific Report #1

Approved for public release; distribution unlimited

05

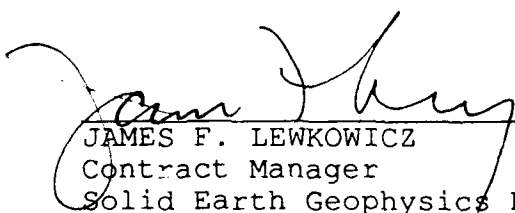
GEOPHYSICS LABORATORY
AIR FORCE SYSTEMS COMMAND
UNITED STATES AIR FORCE
HANSCOM AIR FORCE BASE, MASSACHUSETTS 01731-5000

SPONSORED BY
Defense Advanced Research Projects Agency
Nuclear Monitoring Research Office
ARPA ORDER NO.5299

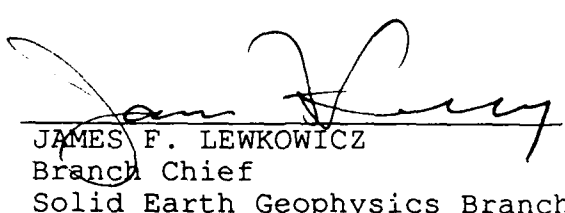
MONITORED BY
Geophysics Laboratory
AFOSR Grant 89-0259

The views and conclusions contained in this document are those of the authors and should not be interpreted as representing the official policies, either expressed or implied, of the Defense Advanced Research Projects Agency or the U.S. Government.

This technical report has been reviewed and is approved for publication.

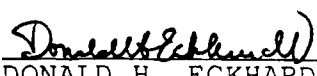


JAMES F. LEWKOWICZ
Contract Manager
Solid Earth Geophysics Branch
Earth Sciences Division



JAMES F. LEWKOWICZ
Branch Chief
Solid Earth Geophysics Branch
Earth Sciences Division

FOR THE COMMANDER



DONALD H. ECKHARDT, Director
Earth Sciences Division

This report has been reviewed by the ESD Public Affairs Office (PA) and is releasable to the National Technical Information Service (NTIS).

Qualified requestors may obtain additional copies from the Defense Technical Information Center. All others should apply to the National Technical Information Service.

If your address has changed, or if you wish to be removed from the mailing list, or if the addressee is no longer employed by your organization, please notify GL/IMA, Hanscom AFB, MA 01731-5000. This will assist us in maintaining a current mailing list.

Do not return copies of this report unless contractual obligations or notices on a specific document requires that it be returned.

REPORT DOCUMENTATION PAGE

Form Approved
 OMB No. 0704-0188

1a. REPORT SECURITY CLASSIFICATION Unclassified		1b. RESTRICTIVE MARKINGS	
2a. SECURITY CLASSIFICATION AUTHORITY		3. DISTRIBUTION/AVAILABILITY OF REPORT Approved for public release; Distribution unlimited	
2b. DECLASSIFICATION/DOWNGRADING SCHEDULE		5. MONITORING ORGANIZATION REPORT NUMBER(S) GL-TR-90-0062	
4. PERFORMING ORGANIZATION REPORT NUMBER(S)		7a. NAME OF MONITORING ORGANIZATION Geophysics Laboratory	
6a. NAME OF PERFORMING ORGANIZATION University of Oslo	6b. OFFICE SYMBOL (if applicable)	7b. ADDRESS (City, State, and ZIP Code) Hanscom AFB Massachusetts 01731-5000	
6c. ADDRESS (City, State, and ZIP Code) Department of Geology, P.O.Box 1047, Blindern, N-0316 OSLO 3, NORWAY		9. PROCUREMENT INSTRUMENT IDENTIFICATION NUMBER AFOSR - 89 - 0259	
8a. NAME OF FUNDING/SPONSORING ORGANIZATION DARPA	8b. OFFICE SYMBOL (if applicable) NMRO	10. SOURCE OF FUNDING NUMBERS	
8c. ADDRESS (City, State, and ZIP Code) 1400 Wilson Blvd. Arlington, VA 22209 - 2308		PROGRAM ELEMENT NO. 61101E	PROJECT NO. 9A10
		TASK NO. DA	WORK UNIT ACCESSION NO. AE
11. TITLE (Include Security Classification) Seismic surveillance - nuclear test ban verification			
12. PERSONAL AUTHOR(S) E.S. Husebye; B.O. Paul			
13a. TYPE OF REPORT Scientific Report #1	13b. TIME COVERED FROM 1 Jan 89 TO 31 Dec 89	14. DATE OF REPORT (Year, Month, Day) 1990 February 26	15. PAGE COUNT 138
16. SUPPLEMENTARY NOTATION			
17. COSATI CODES		18. SUBJECT TERMS (Continue on reverse if necessary and identify by block number)	
FIELD	GROUP	SUB-GROUP	Robust seismic event location schemes; crustal structure mapping in the NORESS siting area, S.Scandia and Fennoscandia; Tele seismic coda analysis, P-to-Rg scattering in the NORESS siting area
19. ABSTRACT (Continue on reverse if necessary and identify by block number)			
<p>The research performed under the grant, during the period 1 January 1989 through 31 December 1989, can be divided into three main topics: i) robust seismic event location schemes; ii) crustal structure mapping; and iii) teleseismic P-coda scattering analysis.</p> <p>In section 2 we present new techniques for fast and robust event location. In case of available arrival times from a network of seismograph network (aperture up to 10-15 deg) a variant of Geiger's method for fitting arrival times to travel time tables, gave average location errors less than 1 deg in the teleseismic distance range. In another study, the location schemes are tied to the slowness vector as easily derived from arrays and 3-component stations, namely azimuth error minimization and slowness vector summation on a sphere for N arbitrary positioned stations.</p> <p>In section 3 we deal with mapping of crustal structures in various parts of Fennoscandia where the 3 seismic arrays NORESS, ARCESS and FINESA are sited. The starting point is the NORESS site area using relative Pn-arrival times in combination with a modified ACH inversion scheme. Due to the small aperture of NORESS the mapping</p>			
20. DISTRIBUTION/AVAILABILITY OF ABSTRACT <input checked="" type="checkbox"/> UNCLASSIFIED/UNLIMITED <input checked="" type="checkbox"/> SAME AS RPT <input type="checkbox"/> DTIC USERS		21. ABSTRACT SECURITY CLASSIFICATION Unclassified	
22a. NAME OF RESPONSIBLE INDIVIDUAL James Lewkowicz		22b. TELEPHONE (Include Area Code) (617) 377 3222	22c. OFFICE SYMBOL GL/LWH

depth range is also of the same order, namely 3 km. The major result is that the area is relatively homogeneous (rhyolite/granite) except for an intrusive gabbro body in the NE quadrant which appears to be roughly mushroom shaped thinning towards the array center. In the next study, we have used all available seismic reflection and refraction profiling results for S. Scandia so as to produce a crustal thickness map for this area. The crustal thinning associated with the Oslo Rift is pronounced, of the order of 3-5 km, and thus may explain some of the regional wavefield complexities as observed at the nearby NORESS array. Observed arrival times of local seismic crustal phases like Pg, Sg (Lg) and sub-crustal phases Pn and Sn from the Fennoscandian seismograph network are easily extracted from computer files at the national seismological center in Helsinki. Using a conjugate gradient scheme we have made a tomographic estimate of sub-Moho lateral velocity variation along with event hypocenter parameters presuming crustal thicknesses to be known. The most prominent P and S velocity anomalies are found in the northwest (in-land Lofoten) and southwest (Møre) of Norway, and for shear waves also in central Finland.

In section 4 NORESS P-wave coda of 75 s duration from 8 teleseismic events of widely different azimuths have been examined using both array and 3C analysis techniques. Although source-end scattering could not be separated from the source pulse per se, we favor the hypothesis of long source duration supported by observed slow beam amplitude decay rates. The majority of receiver-end scattering contributions appears to be P-to-Rg conversions in both forward and backward modes from two nearby areas with pronounced topographic reliefs, namely Bronkeberget (Dist~10 km, Azi~80 deg) and Skreikampen (Dist~30 km, Azi~225 deg). The scattering is multiple in the sense that both the primary and secondary phases from the source region contribute to the Rg-scattering. P-to-S scattering constitute a significant part of the receiver-end scattering in the later part of the coda but is more diffuse than Rg. P-to-P scattering is weak and mostly confined to the immediate vicinity of the array.

FIRST ANNUAL TECHNICAL REPORT

1 Jan 1989 - 31 Dec 1989

ARPA Order: # 5299, Amendment 18

Program Code:

Name of Grantee: University of Oslo, Norway

Effective Date of Contract: 01 Jan 1989

Contract Expiration Date: 31 Dec 1990

Grant Number: AFOSR-89-0259

Principal Investigators: Eystein S. Husebye 47-2-456647
Bent O. Ruud 47-2-456678

Program Manager: James F. Lewkowicz
(617) 861-3028

Short Title of Work: Seismic Surveillance - Nuclear Test Ban Verification



The views and conclusions contained in this document are those of the authors and should not be interpreted as necessarily representing the official policies or endorsements, either expressed or implied, of the Defense Advanced Research Projects Agency or the U.S. Government

Sponsored by
Defense Advanced Research Projects Agency
DARPA Order No. 5299, Amendment 18
Monitored by AFOSR Under Grant No. AFOSR-89-0259

University of Oslo
Department of Geology
P.O. Box 1047, Blindern
N-0316 Oslo 3
Norway

Accession For	
NTIS GRA&I	<input checked="" type="checkbox"/>
DTIC TAB	<input checked="" type="checkbox"/>
Unannounced	<input type="checkbox"/>
Justification	
By _____	
Distribution/	
Availability Codes	
Dist	
A-1	

TABLE OF CONTENTS

1	Summary	1
2	Novel event location techniques	
2.1	Teleseismic epicentre locations from arrival times at regional networks	3
2.2	Robust and reliable techniques for epicenter location using time and slowness observations	8
3	Crustal structure mapping	
3.1	Exploring the upper crystalline crust: A joint interpretation of 3D imaging and reflection profiling at the NORESS array	18
3.2	The South Scandinavian crust - Structural complexities from seismic reflection and refraction profiling	29
3.3	Tomographic estimates of sub-Moho seismic velocities in Fennoscandia and structural implications	69
4	Scattering - NORESS teleseismic coda analysis	
4.1	Teleseismic P-coda analyzed by three-component and array techniques - deterministic location of topographic P-to-Rg scattering near the NORESS array	93
5	Research implications - Future work	121

SUMMARY

The project is aimed at seismic surveillance as part of on-going efforts for improving nuclear test ban verification capabilities. The problem is complex in the sense that underground explosions are most efficiently monitored by seismic means, but that the distinction between signals emitted by natural earthquakes and explosions remains unclear. In other words, seismic wave propagation in a heterogeneous Earth may easily mask specific source signatures.

In section 2 we present new techniques for fast and robust event location. In case of available arrival times from a network of seismograph network (aperture up to 10-15°) a variant of Geiger's method for fitting arrival times to travel time tables, gave average location errors less than 1° in the teleseismic distance range. In another study, the location schemes are tied to the slowness vector as easily derived from arrays and 3-component stations, namely azimuth error minimization and slowness vector summation on a sphere for N arbitrary positioned stations. These new techniques have already proved useful for fast event location, and thus help to sort out the numerous reportings from the many seismograph stations distributed globally.

In section 3 we deal with mapping of crustal structures in various parts of Fennoscandia where the 3 seismic arrays NORESS, ARCESS and FINESA are sited. The starting point is the NORESS site area using relative Pn-arrival times in combination with a modified ACH inversion scheme. Due to the small aperture of NORESS the mapping depth range is also of the same order, namely 3 km. The major result is that the area is relatively homogeneous (rhyolite/granite) except for an intensive gabbro body in the NE quadrant which appears to be roughly mushroom shaped thinning towards the array center. In the next study, we have used all available seismic reflection and refraction profiling results for S. Scandia so as to produce a crustal thickness map for this area. The crustal thinning associated with the Oslo Rift is pronounced, of the order of 3-5 km, and thus may cause some of the regional wavefield complexities as observed at the nearby NORESS array.

Observed arrival times of local seismic crustal phases like Pg, Sg (Lg) and sub-crustal phases Pn and Sn from the Fennoscandian seismograph network are easily extracted from computer files at the national seismograph center in Helsinki. Using a conjugate gradient scheme we have made a tomographic estimate of sub-Moho lateral velocity variation along with event hypocenter parameters presuming crustal thicknesses to be known. The most prominent P and S velocity anomalies are found in the northwest (in-land Lofoten) and southwest (Møre) of Norway, and for shear waves also in central Finland. Structural information of the above kind is essential for wavefield modelling of the mentioned array recordings. For example, some of the observed anomalies in array azimuths and apparent velocities might be explained by structural information as opposed to purely empirical corrections. Anyway, the results reported here are to our knowledge the most detailed published so far for this region.

In section 4 NORESS P-wave coda of 75 s duration from 8 teleseismic events of widely different azimuths have been examined using both array and 3C analysis techniques. Although source-end scattering could not be separated from the source pulse per se, we favor the hypothesis of long source duration supported by observed slow beam amplitude decay rates. The majority of receiver-end scattering contributions appears to be P-to-Rg conversions in both forward and backward modes from two nearby areas with pronounced topographic reliefs, namely Bronkeberget (Dist~10 km, Azi~80°) and Skreikampen (Dist~30

km, Azi~225°). The scattering is multiple in the sense that both the primary and secondary phases from the source region contribute to the Rg-scattering. P-to-S scattering constitute a significant part of the receiver-end scattering in the later part of the coda but is more diffuse than Rg. P-to-P scattering is weak and mostly confined to the immediate vicinity of the array. These results are interesting on two accounts, firstly we have pin-pointed two specific scattering sources contributing significantly to the P-wave coda at the NORESS array and secondly by invoking the principle of reciprocity we may expect similar scattering mechanisms to be responsible for scattering near the seismic source.

Teleseismic epicentre locations from arrival times at regional networks

B. O. Ruud

Geology Department, University of Oslo, PO Box 1047 Blindern, N-0316 Oslo 3, Norway

SUMMARY

Arrival time reportings from local and regional networks can be used for preliminary epicentre location of teleseismic events via slowness and azimuth estimation. Robust techniques for doing so are presented, and their relative performance tested on ISC listed *P* arrival times of Fennoscandian stations (aperture ca. 10°). For the 10 events analysed, the most efficient technique, a variant of Geiger's method for fitting arrival times to traveltime tables, gave average location errors of less than 1° for distances from 15° to 85°.

Key words: arrival times, epicentres, teleseismics.

1 INTRODUCTION

The increasing daily flow of arrival times readings into seismological centres complicates the process of regrouping into event families necessary for precise earthquake location. This work is much facilitated when preliminary epicentre locations are available from national and local centres. While epicentre locations are often reported for local events, distant phases are usually given with no indication of source location. The phase association problem for globally distributed stations can thus be very difficult, but for a regional subset of stations the problem is easier to handle because arrival times for a given event will be within a shorter time interval. This requires the solution of a well-known problem in network and array operation, i.e. that of locating earthquakes based on azimuth and slowness estimates (see also Cassidy *et al.* 1989). In this paper, we investigate methods capable of giving robust preliminary epicentre locations from arrival times of stations distributed over an area of aperture of about 10° or less.

2 METHODS FOR NETWORK SLOWNESS VECTOR ESTIMATION

The problem of locating earthquakes far outside the area of available stations is generally very unstable using only *P* phases as demonstrated by Buland (1976) and Thurber (1985). This is due to a lack of data that makes the normal equations almost singular. However, by assuming a fixed depth (or by determining source depth by depth phases) the problem is manageable in the range 15°–85° because distances in this range have a one-to-one correspondance with slowness (see Fig. 1a). For other distances, the first

arrivals will be *P_n*, *P_{diff}*, or *PKP*, all with almost constant slowness which ensures poor distance resolution. Differential traveltimes like *PP*–*P* or *S*–*P* can give precise distance estimates (Ruud *et al.* 1988), but such methods are not discussed here.

The idea of using azimuth and slowness estimates from arrival times at a local seismic network is not new, see for example Kelly (1964) and Otsuka (1966). The simplest approach is to assume a plane wavefront and a local flat-earth approximation and solve for the least-squares estimate of the horizontal slowness vector.

2.1 Method 1: plane wavefront

The equation for a plane wavefront as a function of latitude ϕ and longitude λ can be written

$$t(\phi, \lambda) = t(\phi_0, \lambda_0) + (\lambda - \lambda_0) \cos \phi_0 u_E + (\phi - \phi_0) u_N \quad (1)$$

where u_E and u_N are the east and north components of the horizontal slowness vector and (ϕ_0, λ_0) is a reference point in the array. Since the equation is linear in the unknowns $t(\phi_0, \lambda_0)$, u_E and u_N , standard linear inverse methods can be applied. Azimuth

$$\gamma_0 = \arctan(u_E/u_N)$$

and slowness

$$\left. \frac{\partial t}{\partial \Delta} \right|_{\Delta_0} = |u| = \sqrt{u_E^2 + u_N^2}$$

relative to the reference point are then found.

This approach is satisfactory for arrays/networks with aperture up to about 100 km, depending of the accuracy of

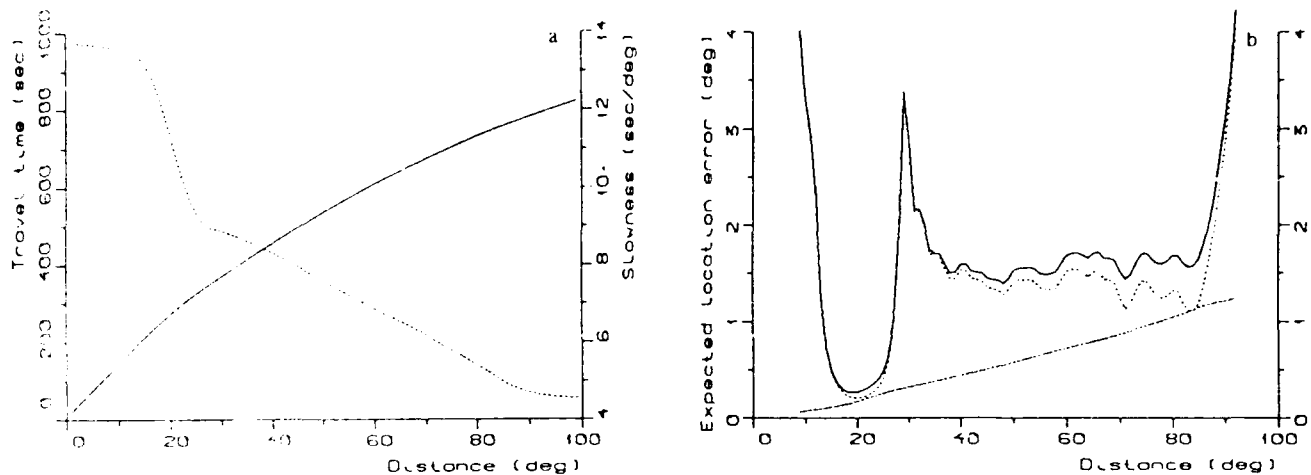


Figure 1. (a) *P*-wave traveltime (solid curve) and slowness (dashed curve) for surface focus. Data are from Herrin's (1968) tables. (b) Expected location error due to an uncertainty in the horizontal slowness vector of $0.1 \text{ s degree}^{-1}$ for *P* phase. The lower curve is for azimuth and the middle curve for slowness error. The upper curve is the total location error.

the arrival time measurements. For larger arrays, slowness variations over the area of the network, wavefront curvature due to finite epicentral distance, and distortion from the flat-earth transformation require other schemes.

2.2 Method 2: curved wavefront based on Taylor expansion

Various methods have been proposed to remedy the deficiencies of the plane wavefront technique. Most of these are based on representations of the wavefront as second or higher order polynomial surfaces in Cartesian or spherical coordinates. Also non-integer powers of latitude-longitude coordinates have been tried (Husebye 1969).

Although these methods are capable of representing many kinds of curved surfaces, the estimated surface will not necessarily resemble the wavefront expected from a point source in a spherical symmetric earth model. In order to obtain reliable estimates, the number of free parameters should also be kept as low as possible.

The least ambiguous assumption to make about the arrival time is that it is a function of epicentral distance only (t_0 ; fixed depth). To account for smooth variations in the slowness over the network, the wavefront could be approximated by a second-order Taylor expansion formula in the arrival time $t(\Delta)$:

$$t(\Delta) = t(\Delta_0) + \left. \frac{\partial t}{\partial \Delta} \right|_{\Delta_0} (\Delta - \Delta_0) + \frac{1}{2} \left. \frac{\partial^2 t}{\partial \Delta^2} \right|_{\Delta_0} (\Delta - \Delta_0)^2. \quad (2)$$

In order to calculate the distance for each station a 'trial' epicentre, defined by its distance Δ_0 and azimuth γ_0 relative to the reference point, is used. Distance Δ is a non-linear function of the epicentre coordinates (Δ_0, γ_0) so an iterative technique is necessary to solve for a least-squares estimate of the unknowns. The epicentre coordinates are updated for each iteration and provided that the algorithm converges to the correct solution, the method is exact in azimuth while a second-order approximation is made for distance. In addition to the epicentre coordinates there are three

unknown parameters; $t(\Delta_0)$, $\partial t / \partial \Delta|_{\Delta_0}$, and $\partial^2 t / \partial \Delta^2|_{\Delta_0}$. Some of these parameters are unnecessary under certain assumptions. For instance, fixed values might be used for $\partial^2 t / \partial \Delta^2|_{\Delta_0}$ (almost constant for many phases and distance ranges) or for Δ_0 if distance is large compared to aperture.

Note that, so far, no assumptions have been made about the type of phase used (except that it must be the same for all stations) or the velocities in the earth model. The next step is to use the estimated slowness and convert it into distance using traveltime tables or earth velocity models. Thus, proper phase identification must be made, but in principle the slowness and azimuth estimates discussed above are independent of phase type. Relatively large discrepancies are sometimes found between the parameter Δ_0 , depending on wavefront curvature, and the distance corresponding to the estimated slowness. This is not unexpected when distance is large compared to aperture or if only few readings with large errors are available. Since distance found from slowness conversion is far more reliable, Δ_0 is here considered as a parameter necessary to represent a realistic wavefront and not as the final distance estimate.

2.3 Method 3: fitting arrival times directly to traveltime tables or earth models

In many cases, the first *P* phase is easily identified as such and the possible advantage of a phase-independent slowness estimate is not relevant. Also, the known coupling between Δ , $\partial t / \partial \Delta$ and $\partial^2 t / \partial \Delta^2$ due to the information accumulated in traveltime tables (or earth velocity models), should be utilized to reduce the number of unknowns. This could be done by adding certain constraints to the model and solving for just one of these three distance-dependent parameters. If we choose to use $t(\Delta_0)$, Δ_0 and γ_0 as unknowns, we are in fact back to the traditional earthquake location scheme originally due to Geiger (1910). The equation for the wavefront can then be written as

$$t(\Delta) = t_0 + T(\Delta) \quad (3)$$

where t_0 is origin time and $T(\Delta)$ denotes the traveltimes derived from tables or an earth model. As with method 2, distance depends on the epicentre coordinates given by distance Δ_0 and azimuth γ_0 relative to the reference point. This representation is preferred because it seems to improve convergence compared to spherical coordinates when solving this non-linear inverse problem with a Gauss-Newton iteration method (see also Thurber 1985). Appendix A shows how the partial derivatives of t are calculated with this epicentre representation.

2.4 Error analysis

Formal error analysis can be carried out as usual for least-squares estimation. What is given here is only a simplified analysis, with emphasis on how errors propagate from observations via azimuth and slowness into location errors. Discussion of array location capabilities can also be found in Gjøystdal, Husebye & Rieber-Mohn (1973).

The accuracy of the estimated slowness vector depends on the array geometry and the accuracy of the arrival times. As a rough approximation, the slowness uncertainty δu is equal to the time uncertainty divided by the aperture, (i.e. the diameter of the least circle surrounding all stations) provided that the network is not too elongated. For instance, a network of 10° aperture with relative arrival time errors of 1 s, would give slowness errors of the order of $0.1 \text{ s degree}^{-1}$. Precision may improve with many stations, but aperture is still the main parameter controlling slowness accuracy.

Azimuth errors are slowness dependent and is greatest for near vertical incidence (low slowness). The azimuth uncertainty $\delta\gamma$ is given by

$$\delta\gamma = \frac{\delta u}{|u|}$$

(in radians). Thus, for a certain phase, the expected azimuth error is a function of distance through the slowness. The location error δe_γ due to an azimuth error is scaled by a distance dependent term:

$$\delta e_\gamma = \sin \Delta \delta\gamma.$$

When slowness is converted into distance, the distance uncertainty δe_Δ is controlled by the phase-dependent parameter $\partial^2 t / \partial \Delta^2$, i.e. the slope of the slowness curve in Fig. 1(a). The relation here is

$$\delta e_\Delta = \frac{\delta u}{|\partial^2 t / \partial \Delta^2|}.$$

The total epicentre location error will then be

$$\delta e_{\text{tot}} \approx \sqrt{\delta e_\Delta^2 + \delta e_\gamma^2}.$$

In Fig. 1(b), δe_γ , δe_Δ and δe_{tot} are shown for the P phase. Computations were made using Herrin tables and $\delta u = 0.1 \text{ s degree}^{-1}$.

In addition, there are bias errors due to velocity anomalies. This is a whole subject on its own and may often be the final factor controlling location precision. However, the effect is likely to be most serious for small arrays, and can to a large degree be corrected for by introducing station delays and/or regional location calibrations. For instance,

the average slowness vector deviation at the NORSAR array was reduced from 0.5 to $0.1 \text{ s degree}^{-1}$ using an interpolation scheme based on 93 'master events' (Bertheussen 1976).

3 RESULTS FROM REAL DATA TESTS

The three methods have been tested on arrival times listed in ISC bulletins. A total of 10 events within appropriate distance ranges and with a reasonable number of P -phase readings for stations in the Fennoscandia were selected randomly. The epicentre solutions as reported by ISC are listed in Table 1, and the stations used for each event are given in Table 2. Testing was first attempted using all reporting stations in Norway, Sweden, Finland and Denmark, but after some experiments it was found that the results actually improved by restricting stations only to Sweden and Finland, constituting the core of the Baltic shield, which is likely to be a more laterally homogeneous region (see also Noponen 1974). The stations are distributed in the ranges 60° – 70°N and 12° – 28°E .

The plane wave solution was used as a starting point for the iterative non-linear least-squares estimation of method 2 and 3. Weighting and damping according to reasonable *a priori* information as described by Jordan & Sverdrup (1981) and Jackson & Matsu'ura (1985) were used to stabilize the inversion. Convergence was assured through the use of so-called spacer gradient steps (see Luenberger 1973).

For each event, the reference point was taken as the arithmetic mean of the station coordinates, and the

Table 1. Events used in tests. The regions of the events are: 1; Greece, 2; Carlsberg Ridge, 3; Kodiak Islands, 4; Pakistan, 5; K sh , Japan, 6; Marianas Islands, 7; Tadzhikistan, USSR, 8; Greece, 9; Afghanistan, 10; Ecuador.

Event No.	Date	Origin time	Latitude (deg N)	Longitude (deg E)	Depth (km)	m_s
1	6 Jul 1980	05:34:42.9	39.25	22.89	23	5.0
2	6 Jul 1980	14:20:25.6	5.59	61.54	19	5.4
3	6 Jul 1980	18:45:31.1	56.59	-154.24	27	4.9
4	10 Jul 1980	19:32:32	35.60	72.06	4	4.6
5	11 Jul 1980	02:43:01.7	30.25	131.23	47	4.8
6	11 Jul 1980	09:41:57	19.99	117.44	8	5.3
7	11 Jul 1980	11:47:23.8	40.18	70.55	8	5.2
8	4 Mar 1981	21:58:07.2	38.24	23.26	32	5.8
9	2 May 1981	16:04:54.6	36.40	71.15	217	5.5
10	6 May 1981	21:36:07.2	-1.95	-80.99	36	5.8

Table 2. Stations used in analysis. These are all stations in Sweden and Finland listed in the bulletins for the selected events.

Station	Event No.									
	1	2	3	4	5	6	7	8	9	10
APP								*	*	*
HES	*	*	*	*	*	*	*	*	*	*
KEV	*	*	*	*	*	*	*	*	*	*
KIR	*	*	*	*	*	*	*	*	*	*
KJF	*	*	*	*	*	*	*	*	*	*
NER	*	*	*	*	*	*	*	*	*	*
SLL								*	*	*
SOD	*	*	*	*	*	*	*	*	*	*
SUF								*	*	*
TBY								*	*	*
UMF	*	*	*	*	*	*	*	*	*	*
UPP	*	*	*	*	*	*	*	*	*	*

Table 3. Estimated azimuths, slownesses and distances for the Table 1 events. The θ line for each event gives the azimuth and distance of the epicentre relative to the reference point. The slowness is found from Herrin's (1968) tables for given distance and source depth. For method 1 and 2, the slowness is estimated directly and the corresponding distances are found from tables assuming surface focus, while for method 3 it is the other way round. 'Loc. err.' is the total epicentre location error using the estimated azimuths and distances, and 'RMS' is the root mean square of the time residuals after estimation. For the agencies rms residuals have been calculated from the bulletin residuals after subtracting an average for each event.

Event No	Method	Azimuth (deg)	Slowness (sec/deg)	Distance (deg)	Loc. err. (deg)	RMS (sec)
1	Agency	178.82	9.35	24.94	-	0.71
	Met. 1	176.40	9.45	24.52	1.10	2.06
	Met. 2	178.81	9.65	23.85	1.14	0.70
	Met. 3	178.77	9.50	21.42	0.52	0.33
2	Agency	135.11	6.51	65.21	-	0.54
	Met. 1	133.97	6.91	59.16	6.14	2.84
	Met. 2	135.55	6.49	65.70	0.65	0.28
	Met. 3	135.41	6.54	61.90	0.41	0.52
3	Agency	357.75	6.91	59.19	-	0.37
	Met. 1	355.62	7.01	57.85	2.26	0.91
	Met. 2	356.33	6.95	58.72	1.30	0.22
	Met. 3	356.68	6.97	58.41	1.18	0.41
4	Agency	109.34	8.23	41.11	-	1.84
	Met. 1	119.08	9.07	26.38	14.74	4.17
	Met. 2	109.50	8.53	36.76	4.35	1.35
	Met. 3	110.19	8.26	40.70	0.69	2.02
5	Agency	59.96	6.11	70.66	-	0.21
	Met. 1	61.73	6.19	69.99	1.79	1.16
	Met. 2	60.32	6.12	70.78	0.36	0.09
	Met. 3	60.38	6.13	70.65	0.39	0.10
6	Agency	59.35	1.91	85.88	-	0.54
	Met. 1	53.76	1.87	86.49	1.10	0.65
	Met. 2	59.99	1.89	86.17	0.70	0.32
	Met. 3	59.69	1.83	87.19	1.35	0.36
7	Agency	107.20	8.53	36.67	-	0.14
	Met. 1	107.43	9.22	25.46	11.21	3.67
	Met. 2	107.20	8.52	36.85	0.18	0.08
	Met. 3	107.22	8.51	36.97	0.30	0.09
8	Agency	174.57	9.35	24.93	-	0.56
	Met. 1	173.59	9.30	21.87	0.43	2.26
	Met. 2	175.02	9.51	24.07	0.90	0.47
	Met. 3	174.56	9.55	21.28	0.65	0.55
9	Agency	107.56	8.15	40.38	-	0.46
	Met. 1	110.31	8.96	27.31	13.16	3.78
	Met. 2	105.37	8.22	41.31	1.05	0.29
	Met. 3	108.04	8.18	41.87	1.53	0.35
10	Agency	279.27	4.57	96.85	-	0.71
	Met. 1	282.05	4.59	86.17	11.06	1.19
	Met. 2	279.63	4.61	93.51	3.37	0.76
	Met. 3	280.03	4.61	91.91	4.96	0.77

estimated azimuths, slownesses and distances relative to this point are given in Table 3.

As expected, it is clear from the large location errors and rms residuals of method 1 that the plane wave and flat-earth approximation is not suitable for a network of this size. Still, azimuth estimates are quite good (errors less than 3°), while slowness errors seems to be azimuth dependent (small to the north and south and larger to the east and west).

For most events, method 2 gives very good estimates with small rms residuals. The largest location error is for event 4 which also has the largest rms. In this case, the parameters

$\partial^2 t / \partial \Delta^2|_{\Delta_0}$ and Δ_0 attain unlikely values when adjusting to the apparently poor observational data. Thus, method 2 could be unstable for data with large errors.

As expected, method 3 handles the 'erroneous' data of event 4 better than method 2 due to fewer free parameters. Also this method accounts for variations in $\partial^2 t / \partial \Delta^2$ over the network, most important for distances less than 30°. The largest location error here is for event 10 and is due to distance error. Fig. 1(b) indicates that this is to be expected for distances beyond 85°. The location error for event 9 is mainly due to the fact that this is an intermediate depth earthquake. As seen from the table, the slowness estimate here is actually better than for method 2, although the latter coincidentally gives a better epicentre location when zero depth is assumed. The largest errors in slowness are found for distances less than 30° and could be due to regional variations in the upper mantle P velocities. The Herrin tables used are adjusted to fit traveltimes of the central US for regional distances (Herrin 1968).

4 CONCLUSIONS

Using P arrival times reported from a network with aperture less than 10° we are able to locate epicentres to within 1.5° in the distance range 15°–85°. Possible exceptions are deep earthquakes or distances close to 30° (see Fig. 1b). Estimates can probably be improved by using empirical time corrections or location calibrations not attempted here.

The largest contribution to the location error comes from the distance estimate. As azimuth is expected to be very accurate (within 1°) for all distances and phases, except core phases, other information could be utilized to resolve distance ambiguity. This includes seismicity information and differential traveltimes.

Of the three methods tested, a variant of Geiger's method for fitting arrival times directly to traveltime tables gave the most stable results. This method relies on proper phase identification, so the phase-independent method 2 may be valuable for initial investigations. The plane wave method is obviously only suited for very small networks/arrays, but may in this case be preferable due to its simplicity.

ACKNOWLEDGMENTS

I would like to thank Prof. E. S. Husebye who drew my attention to the teleseismic location problem and for his unfailing willingness to discuss this subject. Also the services of NTN/NORSAR (Kjeller) where this work was carried out is much appreciated. This research is supported by the Defence Advanced Research Projects Agency under AFOSR Grant AFOSR-89-0259 monitored by the Air Force Geophysical Laboratory.

REFERENCES

- Berteussen, K. A., 1976. The origin of slowness and azimuth anomalies at large arrays, *Bull. seism. Soc. Am.*, **66**, 719–741.
- Buland, R., 1976. The mechanics of locating earthquakes, *Bull. seism. Soc. Am.*, **66**, 173–187.
- Cassidy, F., Christoffersson, A., Husebye, E. S., & Ruud, B. O., 1989. Robust and reliable techniques for epicentre locations using time and slowness observations, *Bull. seism. Soc. Am.*, submitted.

- Geiger, L., 1910. Herdbestimmung bei Erdbeben aus den Ankunftszeiten, *K. Gesell. Wiss. Goett.*, **4**, 331-349.
- Gjøystdal, H., Husebye, E. S., & Rieber-Mohn, D., 1973. One-array and two-array location capabilities, *Bull. seism. Soc. Am.*, **63**, 549-569.
- Herrin, E., 1968. Seismological tables for *P* phases, *Bull. seism. Soc. Am.*, **58**, 1193-1241.
- Husebye, E. S., 1969. Direct measurement of $dT/d\Delta$, *Bull. seism. Soc. Am.*, **59**, 717-727.
- Jackson, D. D. & Matsu'ura, M., 1985. A Bayesian approach to nonlinear inversion, *J. geophys. Res.*, **90**, 581-591.
- Jordan, T. H., & Sverdrup, K. A., 1981. Teleseismic location techniques and their application to earthquake clusters in the south-central Pacific, *Bull. seism. Soc. Am.*, **71**, 1105-1130.
- Kelly, E. J., 1964. Limited network processing of seismic signals, *Rep. ESD-TDR-64-369*, Lincoln Lab., Massachusetts Institute of Technology.
- Luenberger, D. G., 1973. *Introduction to Linear and Nonlinear Programming*, Addison-Wesley Publishing Company, Reading, Massachusetts.
- Noponen, I., 1974. Seismic ray direction anomalies caused by deep structure in fennoscandia, *Bull. seism. Soc. Am.*, **64**, 1931-1941.
- Otsuka, M., 1966. Azimuth and slowness anomalies of seismic waves measured on the Central California Seismographic Array, part I, observations, *Bull. seism. Soc. Am.*, **56**, 223-239.
- Ruud, B. O., Husebye, E. S., Ingate, S. F., and A. Christofferson, 1988. Event location at any distance using seismic data from a single, three-component station, *Bull. seism. Soc. Am.*, **78**, 308-325.
- Thurber, C. H., 1985. Nonlinear earthquake location: theory and examples, *Bull. seism. Soc. Am.*, **75**, 779-790.

APPENDIX

In order to apply the Gauss-Newton iteration technique for the least-squares estimation in method 2 and 3, it is necessary to calculate the partial derivatives of $t(\Delta)$ with respect to the parameters to be estimated. As distance Δ is a function of Δ_0 and γ_0 , we have (for method 3)

$$\frac{\partial t}{\partial \Delta_0} = \frac{\partial T}{\partial \Delta} \frac{\partial \Delta}{\partial \Delta_0}$$

and

$$\frac{\partial t}{\partial \gamma_0} = \frac{\partial T}{\partial \Delta} \frac{\partial \Delta}{\partial \gamma_0} \quad (\text{A1})$$

Denoting the distance and azimuth from the reference point to the i th station as d_i and z_i respectively, we find by considering the triangle formed by the epicentre, the reference point and this station

$$\cos \Delta = \cos \Delta_0 \cos d_i + \sin \Delta_0 \sin d_i \cos (z_i - \gamma_0). \quad (\text{A2})$$

Deriving this with respect to Δ_0 and γ_0 we find

$$\frac{\partial \Delta}{\partial \Delta_0} = \{\sin \Delta_0 \cos d_i - \cos \Delta_0 \sin d_i \cos (z_i - \gamma_0)\} / \sin \Delta \quad (\text{A3})$$

and

$$\frac{\partial \Delta}{\partial \gamma_0} = -\sin \Delta_0 \sin d_i \sin (z_i - \gamma_0) / \sin \Delta. \quad (\text{A4})$$

These relations are also used when calculating the derivatives for method 2.

ROBUST AND RELIABLE TECHNIQUES FOR EPICENTER LOCATION USING TIME AND SLOWNESS OBSERVATIONS

BY FRANCES CASSIDY, ANDERS CHRISTOFFERSSON, FYSTEIN S. HUSEBYE,
AND BENT O. RUUD

ABSTRACT

The ever-increasing flow of parameterized and waveform data into various kinds of seismological centers cannot be managed properly unless preliminary epicenter locations are available. Here we demonstrate robust and flexible techniques for fast and reliable event location using the *P* slowness vector, which is easily derived from arrival times and/or waveform data from arrays, networks, and/or single-site three-component stations. Location schemes are tied to 1) azimuth minimization and 2) slowness vector summation on a sphere using slowness from *N* arbitrarily positioned stations. The advantage of using azimuth alone is that no assumption is needed of phase type, distance range, or structure (travel-time tables). The viability of our location techniques are demonstrated using a variety of *P* recordings from networks and three-component stations.

INTRODUCTION

The problem of precisely locating earthquakes has intrigued seismologists for decades and still does. The various approaches published are, with few exceptions, related to Geiger's (1910) iterative, least-squares method on the basis of *P*-wave travel-time observations (e.g., see Jordan and Sverdrup, 1981; Pavlis, 1986). Notable extensions of the Geiger scheme are those of Julian (1973) who also included slowness estimates from array stations, and those of Aki and Lee (1976) and Spencer and Gubbins (1980) who devised novel techniques for jointly estimating hypocenter and earth structure parameters. Arrays and single three-component stations can provide fast although less precise epicenter/hypocenter locations (e.g., see Bratt and Bache, 1988; Ruud *et al.*, 1988).

The topic of this paper is that of novel schemes for automated, preliminary event locations on the basis of *P*-wave slowness vector estimates from local/regional networks of conventional stations, arrays, and/or digital three-component stations. It reflects a rather pressing problem at many seismological centers, namely, an increasing daily flow of *P* arrival reportings from regionally and globally distributed stations from which grouping into event families is a prerequisite to undertaking formal event location procedures. This process is by no means trivial and, in addition, is work-intensive but is much facilitated for events for which preliminary epicenter locations are available. An illustrative example here is NEIC/USGS which receives daily between 1000 to 2000 *P* arrival readings, out of which only about 60 per cent are associated with specific hypocenter solutions. The relatively low association percentage partly reflects a formal constraint of four reportings for defining an event location. Today, an increasing number of 'smart', digital three-component stations are deployed on a global scale. By 'smart' we mean that real-time processing is used for the detection of incoming signals and the novel three-component processing schemes of Christoffersson *et al.* (1988) and Roberts *et al.* (1989) could easily be incorporated for extracting the *P* slowness vector as well. Note that the epicenter location techniques developed here are tested on signal parameters derived off-line, as demonstrated in Figure 1.

EPICENTER LOCATION WITH TIME/SLOWNESS OBSERVATIONS

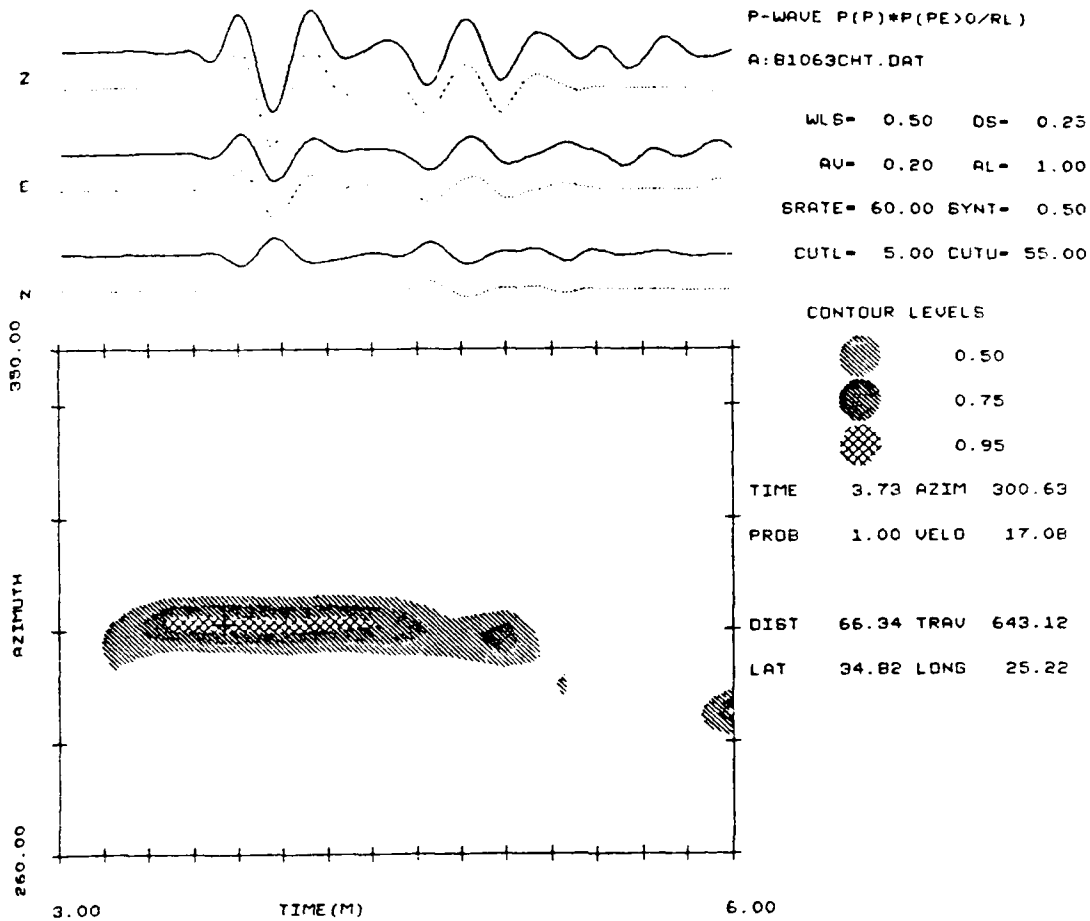


FIG. 1. Extraction of Slowness Vector. Signal from the magnitude $m = 6.0$ Greek earthquake (Event 3, Table 2), recorded at the 3-component station at Chaingmai (18.8N, 99.0E). The plotted contours are probability levels as a function of time and azimuth using a 0.50 min time window (WLS) and a time step (DS) of 0.25 min. The data are velocity filtered (CUTL, CUTU) from 5-55 km/sec, and the probability threshold in filtering the original traces (SYNT) is 0.5. TIME, AZIM, PROB, and VELO values read at cross in figure are given at the right. Also shown are estimated latitude and longitude (LAT, LONG) and travel time (TRAV). Other notations: AV = smoothing parameter; AL = azimuth interval in degrees; SRATE = sampling rate (min).

DATA AVAILABILITY

Before presenting and discussing techniques for fast epicenter locations, a few words on the data at hand for this task are necessary. We differentiate here between observations provided by local/regional networks, arrays, and three-component stations, although the common denominator here is estimates of the P -wave slowness vector, S . Note that in practice S is replaced by its corresponding epicentral distance via standard travel-time tables. Furthermore the S vector often does not have a stringent definition and may be interpreted as apparent velocity, $dT/d\Delta$ or distance.

1. Local/regional networks (aperture 1 to 15 degrees): Reported P -wave parameters are arrival time T_i , amplitude and period for the i th station. T_i observations are transformed to an S estimate using a modified Husebye (1969) scheme as detailed by Ruud (1990).

2. Arrays: Same as above but the S estimate is either tied to the detecting beam location or obtained directly from $f-k$ analysis or variants thereof.
3. Three-component stations: Same as above but S is obtained via an estimate of the P -wave incidence (polarization) angle.

The precision in S -estimates depends on network/array aperture and, for three-component stations, on wavelength. For small arrays apparent wavelength is important and should preferably be less than aperture (Harris, 1982). For local, regional, and core phases the epicentral distance estimates corresponding to S conversions via travel-time tables are often poor due to small time gradients in these ranges. If secondary phases can confidently be identified, differential travel times like $dT(Pn - Pg)$, $dT(PKP - PP)$, etc., would provide accurate distance estimates at the above troublesome ranges. For a three-component station, a 1° error in vertical incidence angle is roughly equivalent to a 4° error in distance at teleseismic ranges. Azimuth errors scale differently and peak at 90° distance.

In the above list of observational data we have included S from digital three-component stations, as this parameter can easily and reliably be extracted using an appropriate analyzing scheme (see Fig. 1). However, Harris (1982) and Bratt and Bache (1988) consider such observations of marginal interest due to a claimed poor precision in S estimates, even in comparison to small aperture (3 km) arrays like NORESS. It suffices here to refer to a recent study by Ruud *et al.* (1988) who found that slowness (azimuth) estimates derived from NORESS and single three-component station records were of similar precision for even small events ($SNR > 2$) at local/regional distances. At teleseismic ranges small arrays suffer from increases in apparent wavelength, while for three-component stations the horizontal energy decreases but for adequate SNRs do not impair the S -estimate *per se*.

FAST EPICENTER LOCATION TECHNIQUES

In this section we present event location schemes on the basis of extracted P -wave signal parameters as outlined above. Epicenter locations for azimuth observations alone are described first, and then slowness vector location. However, before doing so, we comment on direct slowness estimation for P arrival times as reported by local/regional networks.

Network Arrival Times—Wavefront Fitting

Using spherical coordinates, polynomial wavefront fitting is feasible for P arrival times across a network of stations of aperture say in the range of 1 to 15° and hence by derivations can be estimated. The advantage of using networks for S estimation is that their large apertures give precise results with both azimuth and distance errors within a few degrees. A potential problem is that individual stations occasionally report different phases, say Pg and Pn at local distances and $PKP(DF)$ and $PKP(BC)$ in the core window.

Azimuth Location—Angle Minimization

The idea here is to minimize the square differences between observed azimuth (α_i) at N stations and those tied to the unknown epicenter location ($\hat{\phi}$, $\hat{\lambda}$), namely:

$$F = \sum_{i=1}^N [(\alpha_i - G_i(\hat{\phi}, \hat{\lambda}))^2]. \quad (1)$$

EPICENTER LOCATION WITH TIME/SLOWNESS OBSERVATIONS

G_i is defined as:

$$G_i = \sin^{-1} \left[\frac{\sin(\hat{\phi}) \sin(\hat{\lambda}_i)}{\sin(\Delta_i)} \right], \quad (2)$$

where Δ_i is the epicentral distance for the i th station.

Estimates of the standard error of the epicenter estimate can be derived from its covariance matrix (σ_e^2 reflects the variance of the observed azimuths);

$$\text{cov}(\hat{\phi}, \hat{\lambda}) \approx \sigma_e^2 \mathbf{B}^{-1} / (N - 2) \quad (3)$$

where asterisk denotes transpose:

$$\mathbf{B} = \frac{1}{N} \sum_{i=1}^N \begin{bmatrix} A_i \\ B_i \end{bmatrix} \begin{bmatrix} A_i \\ B_i \end{bmatrix}^* \quad (4)$$

and

$$A_i = \frac{\partial G_i}{\partial \hat{\phi}} \quad \text{and} \quad B_i = \frac{\partial G_i}{\partial \hat{\lambda}}. \quad (5)$$

Details on $\partial G_i / \partial \hat{\phi}$ and $\partial G_i / \partial \hat{\lambda}$ are given in the Appendix.

The advantage of using the azimuth part of \mathbf{S} is simply that this parameter is independent of phase type and thus distance range and travel-time tables. In other applications, azimuth from mainly two arrays have been used in conjunction with arrival-time observations in Geiger-type inversion schemes for estimating ϕ, λ (e.g., see Gjøystdal *et al.* 1973; Bratt and Bache, 1988). Our preference for using azimuth alone from several stations (three-component recordings) is that a precise preliminary location is feasible, which subsequently can be used for phase identification and association. The latter is often a problem at international seismological data centers.

Slowness Vector Location—Vector Summing

In addition to bearing, \mathbf{S} contains information on epicenter distance, that is, after conversion to distance via standard travel-time tables. Such a conversion is in practice only valid in the teleseismic window due to small gradients in the travel-time curve at other distance ranges unless additional information is provided. Now, the strategy adapted for epicenter locations using slowness is by means of vector summing based on a method developed by Fisher (1953) for combining observations of position (epicenter) on a sphere (see also Irving, 1964). The optimum event location or center of gravity for N dispersed epicenter ($\hat{\phi}, \hat{\lambda}$) observations is calculated from the vector sum of unit vectors of the N observed directions. Each of these directions is specified by its 3 direction cosines, namely:

$$\begin{aligned} \text{North} \quad l &= \cos(\hat{\phi}) \cos(\hat{\lambda}); \\ \text{South} \quad m &= \cos(\hat{\phi}) \sin(\hat{\lambda}); \\ \text{Vertical} \quad z &= \sin(\hat{\phi}). \end{aligned} \quad (6)$$

The best estimate of the average direction is then a vector sum of the individual directions:

$$L = \frac{1}{R} \sum_{i=1}^N l_i; \quad M = \frac{1}{R} \sum_{i=1}^N m_i; \quad Z = \frac{1}{R} \sum_{i=1}^N z_i \quad (7)$$

where

$$R^2 = \left[\sum_{i=1}^N l_i \right]^2 + \left[\sum_{i=1}^N m_i \right]^2 + \left[\sum_{i=1}^N z_i \right]^2 \quad (8)$$

Then, the mean epicenter location is given by:

$$\tan(\hat{\phi}) = M/L \sin(\hat{\lambda}) = Z \quad (9)$$

Fisher showed that the probability, P , of a point being located between ϕ and $\phi + d\phi$ is:

$$P d\phi = \frac{\kappa}{2 \sin h(\kappa)} e^{\kappa \cos(\phi)} \sin(\phi) d\phi, \quad (10)$$

where κ determines the precision of the points. The best estimate of κ , the so-called precision factor, k , is:

$$k = \frac{N - 1}{N - R} \quad (11)$$

Also, an accuracy measure of the mean direction can be calculated for a particular probability level, $(1 - P)$. The 95 per cent confidence radius is given by:

$$a_{95} = \frac{140}{\sqrt{kN}} \quad (12)$$

and a 65 per cent radius (corresponding to the standard error in Gaussian distributions) is:

$$a_{65} = \frac{67.5}{\sqrt{kN}} \quad (13)$$

These measures would be useful in comparing locations based on slowness with those reported by NEIC, besides serving as a confidence ellipse estimate.

DATA ANALYSIS AND RESULTS

In order to demonstrate the location performances of the above techniques, S vectors were extracted from three-component records at 1 to 90° distances using the Christoffersson *et al.* (1988) technique. A practical problem encountered was that access to digital records from well-separated stations was not easy and data

EPICENTER LOCATION WITH TIME/SLOWNESS OBSERVATIONS

quality was occasionally poor. For some stations the orientations of the horizontal components appear to be off by 15 to 20°. Nonetheless, results to be presented demonstrate the viability of our location schemes.

Explosion—Geophone Record Analysis

During the Fennolara seismic refraction experiment (Lund and Prodehl, 1985) a number of three-component geophones were deployed. In addition to the profiling shots, a nuclear explosion at Semipalatinsk was also recorded by chance. Two of these events have been subjected to "location" analysis, and details on the outcome are given in Table 1.

Event 1: Since epicenter distances were within a few degrees, only azimuth location was feasible. Despite an anomalous observation (station 134, 19.4°) the net mislocation is around 6 km, which is considered very good as the epicenter distance range is 200 to 400 km.

Event 2: The aperture of the geophone line was too small compared to epicentral distance for basing the location on azimuth only. However, using the slowness vectors the estimated epicenter is about 1° off.

Teleseismic Events

We have here analyzed two sets of observations, three-component broadband recordings on NEIC/ORFEUS CD ROMs and the corresponding *P* arrival times

TABLE 1
FENNOLARA PROFILE RESULTS

Station	Event 1: Fennolara Shot (58.47N, 17.38E)			Event 2 Semipalatinsk Explosion (49.89N, 78.89E)						
	Velocity (km/ sec)	Azimuth (deg)	dAzi (deg)	Velocity (km/ sec)	Δ (deg)	d Δ (deg)	Azimuth (deg)	dAzi (deg)	Latitude (°N)	Longitude (°E)
14	7.9	15.8	-4.8	13.5	42.4	5.4	67.3	-5.4	49.4	88.8
17	12.2	19.8	-1.9	13.9	45.6	8.7	79.2	6.4	41.1	84.5
44	6.8	33.6	2.4	12.5	31.0	-5.6	75.3	1.3	52.4	70.9
47	6.8	35.6	2.1	13.6	42.6	6.0	79.2	3.8	43.5	82.6
75	7.1	83.2	7.5	12.9	35.7	-0.5	79.2	3.8	48.4	76.1
86	8.4	110.9	-0.5	13.0	37.6	1.5	67.3	-6.8	53.0	85.9
89	6.8	118.9	0.2	11.4	24.6	-12.6	67.7	-9.9	57.7	62.1
95	7.6	134.8	0.7	13.3	40.3	4.2	65.4	-11.0	52.5	90.9
110	7.8	152.6	-2.4	12.8	34.9	-1.0	77.2	0.2	50.4	77.6
134	8.7	148.6	-19.4	11.7	25.6	-10.0	71.3	-6.8	58.4	67.9
146	8.8	174.9	2.6	signal clipped						

Estimated epicenter: Azimuth (Sec 3.2): 58.43 N (S.E. 0.04 N); 17.53 E (S.E. = 0.12 E); Slowness (Sec 3.3): 50.82 N; 78.85 E ($a_{cs} = 1.60$); ($a_{gs} = 2.77$).

Three-component field geophone recordings from the Fennolara deep seismic profiling experiment used in location experiments: Event 1 is a Fennolara shot (dynamite charge of 800 kg), and event 2, an underground nuclear explosion at Semipalatinsk (USSR) which happened to be recorded. In event 1, only the azimuth part of the *S* vector was used for epicenter location as *P_g*- and *P_n*-phase velocities do not provide acceptable distance estimates. The dAzi column gives the difference between the "true" and observed azimuths. For event 2, the *S* estimate for each station provides an epicenter estimate as listed, but using the vector summation scheme over all reporting stations, an acceptable epicenter location (error near 1°) is obtained. As before, dAzi and d Δ give differences between "true" and observed azimuth and distance estimates, respectively. Azimuth location is not feasible due to the small aperture of the line array.

for Fennoscandian stations as reported by ISC. The results in terms of both azimuth and slowness locations are given in Tables 2 and 3 and for "networking" in Tables 4 and 5. The following comments apply: slowness observations from a few three-component stations suffice for making fast and reliable (within a few degrees) epicenter determinations. More refined estimates are feasible by introducing slowness bias corrections and/or seismicity information. Likewise, networking, as demonstrated here using Fennoscandia *P* arrival times for slowness estimation, also provides reliable locations even on a stand-alone basis.

TABLE 2
STATIONS AND EVENTS USED FOR LOCATION BASED ON
NEIC/ORFEUS BROADBAND DATA

Station	Event 1 Banda Sea	Event 2 Ecuador	Event 3 Greece	Event 4 Afghanistan
ANM		×		
ANT			×	×
BCA			×	
CHT			×	×
CTA	×			×
GRF		×		×
GUM	×			
JAS		×		
KON		×	×	×
MAJ			×	×
NWA	×			×
SHI			×	
SCP		×	×	
SNZ	×			
TAT	×		×	×
ZOB		×		

Event 1: 13 Sep 80; OT 21:43:15.7; 4.1S 127.5E;
H = 29 km; *M* = 5.5.

Event 2: 6 May 81; OT 21:36:06.8; 1.9S 80.9W;
H = 33 km; *M* = 6.0.

Event 3: 4 Mar 81; OT 21:58:05.9; 38.2N 23.3E;
H = 29 km; *M* = 6.0.

Event 4: 2 May 81; OT 16:04:55.6; 36.4N 71.1E;
H = 229 km; *M* = 6.3.

* Station MAJ could not be used in slowness location because estimated velocity was too high (36 km/sec). The results of these location experiments are detailed in Table 3.

TABLE 3
EVENT LOCATIONS ON THE BASIS OF SLOWNESS AND AZIMUTH OBSERVATIONS

Event	Number of Stations	Range (degrees)	NEIC Location		Slowness Location		Azimuth Location		RCC SLOW (degrees)	Standard Error Azimuth	
			Latitude	Longitude	Latitude	Longitude	Latitude	Longitude		Latitude	Longitude
1	5	24-56	4.1S	127.5E	5.1S	125.9E	5.7S	127.7E	2.6	4.6	3.5
2	6	19-92	1.9S	80.9W	0.0S	82.1W	1.2S	79.1W	2.0	1.7	1.2
3	7(8)	7-84	38.2N	23.3E	41.0N	22.2E	39.3N	24.2E	2.2	1.1	3.6
4	8	30-91	36.4N	71.1E	35.0N	69.3E	34.4N	69.3E	3.2	4.1	8.6

Table 2 data are used. For the slowness location, error bounds are expressed in terms of the radius of the 65 per cent confidence circle (RCC).

EPICENTER LOCATION WITH TIME/SLOWNESS OBSERVATIONS

TABLE 4
FENNOSCANDIAN STATIONS USED FOR NETWORKING

Station	Event 1 Banda Sea	Event 2 Ecuador	Event 3 Greece	Event 4 Afghanistan
APP		W	W	W
BER			W	W
COP		W	W	W
HFS	A	W	W	W
KON			W	W
NB2			W	W
TBY		W	W	
UPP		W	W	W
SLL		W	W	W
KEV	A	E	E	E
KJF	A	E	E	E
KIR		E	E	E
NUR		E	E	E
UME		E	E	E
SOD	A	E	E	E
SUF		E	E	E

ISC bulletin reportings are used for events listed in Table 2. E and W denote stations used in defining eastern and western networks, respectively. For the Banda Sea event, a decomposition of Fennoscandian stations into two networks was not feasible due to the limited number of reporting stations. Those used for the Banda Sea event are denoted with A. Location results are detailed in Table 5.

TABLE 5
SUMMARY OF NETWORKING LOCATIONS

Event	Range (degrees)	NEIC Location		Western Stations		Eastern Stations		All Stations	
		Latitude	Longitude	Latitude	Longitude	Latitude	Longitude	Latitude	Longitude
1	94.4	4.1S	127.5E					1.5N	125.4E
2	93.9	1.9S	80.9W	9.8N	80.7W	1.39	81.7W	0.1N	80.4W
3	23.9	38.2N	23.3E	38.6N	25.5E	39.1N	22.6E	39.0N	23.8E
4	42.5	36.4N	71.1E	37.0N	71.9E	36.5N	71.2E	35.5N	71.7E

Event locations on basis of fitted waves front/slowness estimation (Ruud, 1990), using the Fennoscandian seismograph network for events and stations listed in Tables 2 and 4.

CONCLUSIONS

We have here demonstrated techniques for fast and reliable epicenter determination using slowness vector observations from station networks and individual three-component stations. The motivation for undertaking the work reported here is the need in many contexts of seismological data center operations for fast and reliable epicenter locations. As demonstrated, this can be achieved using generally accessible seismological observations, namely, parameterized and/or original waveform data. For actually reducing the workload at various kinds of seismological centers, the above location techniques must be operated in an automated mode. In the case of networking, this entails that suites of incoming *P* arrival times from many stations have to be grouped in time (event separation) and space (identifica-

tion of proper networks) before the respective epicenter locations can be estimated. Likewise, in the case of waveform data, and given detection times, the slowness vectors can easily be extracted together with standard parameters like onset time, etc., without analyst interference. Now, given a preliminary location, arrival times (from stations providing *S* observations) should be introduced for further constraining the epicenter location (see, e.g., Julian, 1973; Cassidy, 1989). Then it would be trivial to check whether *P* arrival reportings from other, conventional stations can be associated with the event in question to, say, within 10 to 20 sec of the expected arrival time. This time span is significantly shorter than it would be were a preliminary event location not available. The *P* arrival window is about 20 min, including core phases.

ACKNOWLEDGMENTS

This work has been supported by the Swedish Natural Science Research Council under Contract G-Gu 4788-105 (A.C., F.C.), the Norwegian Research Council for Sciences and Humanities (RNF/NAVF) under contract D.48.50.01 (E.S.H.), and the Defense Advanced Research Projects Agency under AFOSR-89-0259 (B.O.R.).

REFERENCES

- Aki, K. and W. H. K. Lee (1976). Determination of three-dimensional velocity anomalies under a seismic array using first *P* arrival times from local earthquakes; I. A homogeneous initial model, *J. Geophys. Res.* **81**, 4381-4399.
- Bratt, S. R. and T. C. Bache (1988). Locating events with a sparse network of regional arrays. *Bull. Seism. Soc. Am.* **78**, 780-798.
- Bullen, K. E. (1963). *An Introduction to the Theory of Seismology*, Cambridge University Press, Cambridge.
- Cassidy, F. (1989). Event location using 3-component station networks. *M.Sc. Thesis*, University of Uppsala, Sweden.
- Christoffersson, A., E. S. Husebye, and S. F. Ingate (1988). Wavefield decomposition using ML-probabilities in modeling single-site 3-component records, *Geophys. J.* **93**, 197-213.
- Fisher, R. A. (1953). Dispersion on a sphere, *Proc. Roy. Soc. London A*, **217**, 295-305.
- Geiger, L. (1910). Herdbestimmung bei Erbeben ans den Ankunftszeiten, *K. Gessel. Wiss. Goett.*, **4**, 331-349.
- Gjøystdal, H., E. S. Husebye, and D. Rieber-Mohn (1973). One-array and two-array location capabilities, *Bull. Seism. Soc. Am.* **63**, 549-569.
- Harris, D. B. (1982). Uncertainty in direction estimation: a comparison of small arrays and three-component stations. Lawrence Livermore National Lab., *Tech. Rep. UGID-19589*, Livermore, California.
- Husebye, E. S. (1969). Direct measurements of the $dT/d\Delta$, *Bull. Seism. Soc. Am.* **59**, 717-728.
- Irving, E. (1964). *Paleomagnetism and Its Application to Geological and Geophysical Problems*, Wiley, New York.
- Jordan, T. H. and K. A. Sverdrup (1981). Teleseismic location techniques and their application to earthquake clusters in the South-Central Pacific, *Bull. Seism. Soc. Am.* **71**, 1105-1130.
- Julian, B. R. (1973). Extension of standard event location procedures, *Seismic Discrimination Semiann. Tech. Sum.*, Lincoln Laboratory, Massachusetts Institute of Technology.
- Lund, C. E. and C. Prodehl (1985). Crustal structure of the Baltic Shield based on the 1979 Fennolora seismic refraction line, *Terra Cognita* **5**, (2-3), 157.
- Pavlis, G. L. (1986). Appraising earthquake hypocenter location errors: a complete, practical approach for single-event locations, *Bull. Seism. Soc. Am.* **76**, 1699-1717.
- Roberts, R. G., A. Christoffersson, and F. Cassidy (1989). Real time event detections, phase identification and source location estimation using single-station three-component seismic data, *Geophys. J.* **97**, 471-490.
- Ruud, B. O. (1990). Teleseismic epicenter locations from arrival times at a regional network, *Geophys. J.* (in press).

EPICENTER LOCATION WITH TIME/SLOWNESS OBSERVATIONS

Ruud, B. O., E. S. Husebye, A. Christoffersson, and S. F. Ingate (1988). Event location at any distance using seismic data from a single, three-component station, *Bull. Seism. Soc. Am.* **78**, 308-325.
 Spencer, C. and D. Gubbins (1980). Travel-time inversion for simultaneous earthquake location and velocity structure determination in laterally varying media, *Geophys. J. R. Astr. Soc.* **63**, 95-116.

DEPARTMENT OF GEOPHYSICS
 UNIVERSITY OF UPPSALA
 BOX 556
 S-75122 UPPSALA, SWEDEN
 (F.C., A.C.)

DEPARTMENT OF GEOLOGY
 UNIVERSITY OF OSLO
 BOX 1047
 0316 BLINDERN
 OSLO 3, NORWAY
 (E.S.H., B.O.R.)

Manuscript received 9 September 1988

APPENDIX

For estimating standard errors for azimuth minimization we need the ϕ , λ -derivatives of the G -function. Consider a spherical triangle $O(\varphi, \lambda)$, $Q(\hat{\varphi}, \hat{\lambda})$ and $P(0, 0) =$ North pole, where $\varphi = 90 - \phi$ and $\hat{\varphi} = 90 - \hat{\phi}$ denotes colatitude. The following relation holds:

$$\sin(\alpha) = \sin(\hat{\varphi})\sin(\hat{\lambda} - \lambda)/\sin\Delta$$

where α is azimuth, Δ is epicentral distance and $(\hat{\lambda} - \lambda)$ is the P angle. The relation between Δ and φ, λ is given by the classic distance formula (Bullen, 1963),

$$\cos(\Delta) = A\hat{A} + B\hat{B} + C\hat{C}$$

where $A = \sin(\varphi)\cos(\lambda)$, $B = \sin(\varphi)\sin(\lambda)$, $C = \cos(\varphi)$. Derivatives with respect to the epicenter parameters are obtained from:

$$dG = d\alpha = \frac{1}{\sin(\Delta)\cos(\alpha)} [\sin(\hat{\varphi} - \varphi)\cos(\hat{\varphi}) d\hat{\varphi} \\ + \sin(\hat{\varphi})\cos(\hat{\lambda} - \lambda) d\hat{\lambda} - \sin(\alpha)\cos(\Delta) d\Delta]$$

and

$$d\Delta = \frac{-1}{\sin(\Delta)} [[A \cos(\hat{\varphi})\cos(\hat{\lambda}) \\ + B \cos(\hat{\varphi})\sin(\hat{\lambda}) - \sin(\hat{\varphi})\cos(\varphi)] d\hat{\varphi} - [A\hat{B} + A\hat{A}] d\hat{\lambda}]$$

Combining these expressions leads to the derivatives $\partial G/\partial\hat{\phi}$ and $\partial G/\partial\hat{\lambda}$. Finally the axes of the $\hat{\phi}, \hat{\lambda}$ confidence ellipse can be estimated using standard procedures.

Exploring the upper crystalline crust: A joint interpretation of 3D imaging and reflection profiling at the NORESS array

B.O. Ruud¹ and E.S. Husebye^{1,2}

¹Dept. of geology, Univ. of Oslo, Norway

²Leave of absence from NORSAR

Abstract

P-wavefield complexities are easily seen in the NORESS array records despite its small aperture of 3 km. The siting area is well mapped geologically and is partly 'sampled' by a 2.5 km seismic reflection profile. Using this information in combination with tomographic mapping (ACH) on the basis of NORESS P_n -records, we have undertaken a structural mapping of the siting area down to ca 3 km. The major result is that the area is relatively homogeneous (rhyolite/granite) except for the north-east quadrant that is dominated by an intrusive gabbro body. The gabbro intrusion appears to be roughly mushroom shaped thinning towards the array center. Only the upper profiling reflector (ca 1.1 km) is accounted for by this model while deeper ones at ca 1.7 and 2.5 km do not have a counterpart in the 3D results. The small array aperture exclude mapping of more deep seated structural anomalies.

Introduction

Exploration geophysicists have a preference for seismic reflection profiling as the principal tool for remotely mapping subsurface structures which otherwise are accessible only through costly drilling operations. On the other hand, seismologists have a long tradition in using wide-angle reflection and refraction profiling techniques in their endeavor to map two-dimensionally the crust and lithosphere in ever increasing detail. With the advent of seismic tomography (e.g., see Aki et al, 1977) a new kind of mapping techniques has become very popular whenever observationally feasible. The reason for this is naturally the possibility of obtaining 3D velocity images of subsurface structures.

Mapping of structural heterogeneities pose a number of intriguing problems for the following reasons; petrological classifications are based mainly on mineralogy and textural criteria, seismic reflection surveys map vertical impedance contrasts (first order changes in physical properties), while 3D imaging is aimed at delineating velocity variations averaged over large volumes. In this context, the small aperture array (3 km) NORESS in S.-E. Norway is unique; the area is well mapped geologically, a short (2.5 km) seismic reflection profile crosses the array (see Fig. 1) and its 25 vertical sensors provide data adequate for inversion (imaging) experiments.

The topic of this paper is simply to investigate how the reflection profile and 3D imaging results compare and to make a joint interpretation of the two data sets.

Geology of the NORESS siting area

The array is situated on Precambrian rock in southeastern Norway, ca 20 km east of the northern truncation of the Oslo Graben structure. In Fig. 1 a small section of the geological maps (Skålvoll, 1988) covering the NORESS array region is reproduced. The area is dominated by granites and rhyolites with dominant strike southeast-northwest. Intruded in the granite and rhyolites are gabbro bodies in which physical properties (density and seismic velocity) sharply contrasts with those of the surrounding rocks. The intrusions might either be plug-shaped occasionally including geometrical 'mushrooming' at the top or sill-shaped (possibly dipping and gently folded). Subsurface geometries can only be hinted at, but as the rhyolites to the southwest and northeast are connected to the southeast (outside the map area), a reasonable hypothesis is the rocks beneath the NORESS array have been folded either into a synform or an antiform.

The reflection profiling survey

The profile was shot in 1983 as part of site localization for the NORESS array. Instrumentation used was the Texas Instrument DFS V, 24 geophones spaced 20 m apart (least offset 120 m). Profile length is 2.5 km and signals were generated with dynamite charges of 1.4 kg in 8 m deep boreholes at 40 m intervals. During processing (CMP stacking) terrain corrections and crooked profile line corrections were introduced. For details see Mykkeltveit (1987).

The main outcome of the profiling experiment is according to Mykkeltveit (see also Fig. 2), the existence of 3 clear reflectors within the upper 1 sec TWT interval, namely (i) dipping reflector at 0.37 sec TWT (ca 1.1 km) at the northern end of the profile continuing up to near surface at the southern end, (ii) dipping reflector at 0.55 sec TWT (ca 1.7 km) in the central part of the profile, and (iii) apparently horizontal reflector at 0.80 sec TWT (ca 2.5 km). Mykkeltveit (1987) tentatively interprets the uppermost reflector as a granite/gabbro interface dipping northwards at about 20°.

3D inversion method and results

The data used for this experiment were extracted by measuring the exact arrival time of special features in the seismograms such as the maximum/minimum amplitude of a peak/trough near the onset of the signal. Only events with very good SNR were selected and the times were determined with precision well below the sampling interval using natural cubic spline interpolation between samples. By comparing data estimates from several pair of events at the same locations, very high consistency was found, indicating a precision better than 2 msec near the onset of strong signals. A total of 582 relative arrival times from 24 events with a reasonably good

azimuth coverage were used in the inversion. Interestingly, with this kind of timing precision array azimuth and apparent velocities can be estimated very accurately, that is with 1-2° and 0.1-0.2 km/sec respectively, excluding bias effects from velocity anomalies (Ruud, 1988; see also Harris, 1982).

One of the basic assumptions of the ACH method, necessary to justify the use of kinematic ray-tracing, is that the size (spatial extension) of the anomalous structures must be greater than the dominating wavelength in the data (e.g., for ACH inversion of NORSEAR data wavelengths are about 3 km while spatial correlation distance is ca 20 km). The dominating wavelength in the NORESS records used in this study is about 1 km, while the spatial correlation length of the data residuals is about 4 km. Thus the high frequency approximation inherent in travel time inversion is strictly not valid for this experiment. However, using principles from Fresnel diffraction theory we may define the 'width of a ray' (radius ρ) at a distance D from the receiver by requiring that the difference in distance to the diffraction point in the wavefront to be less than a quarter of the wavelength λ so that they interfere constructively (Nolet, 1987, p. 10). For a source at infinite distance we then have

$$\sqrt{\rho^2 + D^2} - D = \lambda/4 \quad (1)$$

Solving for ρ we get

$$\rho = \sqrt{(\lambda/4)^2 + D\lambda/2} \quad (2)$$

For instance, for $\lambda = D = 1$ km we get $\rho = 0.75$ km which gives a clue to the 'resolving power' of the data at a depth of 1 km. This reasoning was used when deciding the size of the blocks used in the tomographic experiment.

Another basic assumption of the method is that the anomalies should be confined to the interior of the model so that the wave is plane as it enters into the model at the bottom interface. This assumption is in most cases not strictly valid, but in practice the model is made a little larger than the volume we expect to be well resolved by the data. Any velocity anomalies outside but close to the model will then appear primarily in the bottom layer. Larger scale (larger than the model) anomalies far from the array could refract the wave such that it arrive from a direction somewhat different from the one expected from bulletin information, but still mainly as a plane wave. To account for this we define travel time anomalies relative to the best fitting plane wave and not relative to expected azimuth and slowness. Denoting arrival time of the i -th event at the j -th sensor as t_{ij} , the average arrival time as \bar{t}_i , the slowness vector as \mathbf{u}_i , and the position of the j -th sensor relative to the array centre as \mathbf{r}_j , the time residuals are defined as

$$\Delta t_{ij} = t_{ij} - (\bar{t}_i + \mathbf{r}_j \cdot \mathbf{u}_i) \quad (3)$$

where \bar{t}_i and \mathbf{u}_i are least square estimates for each event. Elevation corrections were allowed for (although not included in the equation above).

In contrast to the original ACH method all event parameters were retained as unknown through the inversion process. The estimated event slownesses are used for ray-tracing in the initial lateral homogeneous model in order to compute the

length of the ray-segments d_{ijk} (event i , sensor j , block k). The system of equations to invert is then

$$\Delta t_{ij} = \Delta t_i + \mathbf{r}_j \cdot \Delta \mathbf{u}_i + \sum_k d_{ijk} \Delta s_k \quad (4)$$

where Δt_i and $\Delta \mathbf{u}_i$ are correction terms to the event parameters and Δs is the slowness anomalies. This extended system was solved using the method of parameter separation (Spencer and Gubbins, 1980) which reduce the size of the system to the same as for the original ACH method. Stochastic inversion was used to damp unresolved model parameters.

The obtained slowness anomalies are presented in Fig. 3 together with standard deviations. The variations in standard deviation depends mainly on model resolution which is very good in the central blocks in each layer (about 0.9), but decreasing towards the peripheral blocks. As usual with ACH-type of inversion horizontal velocity layering can not be resolved because relative time residuals are used. The RMS value of the residuals were 5.5 msec which is reduced to 3.7 msec by the inversion. In terms of variances, the model explains 53% of the observed residuals. The lateral dimensions of the model were increased with depth in order to assure that all rays are within the model volume when entering the bottom layer from below (the incidence angle of most rays is less than 47° , corresponding to P_n velocity, ca 8.2 km/sec) and the block size were also increased according to the expected decrease in resolving power with depth.

Regarding the estimated slowness anomalies, we see that the most significant anomalies, i.e., anomalies greater than the estimation error, are confined to the uppermost layer (depth range: 0.0-1.0 km) and that there is a dominance of high velocities to the north-east in this layer. In the second layer (depth range: 1.0-2.5 km) anomalies are generally much smaller, and we note that the strongest anomalies are confined to the peripheral blocks where estimation errors also are large. For the third layer (depth range: 2.5-5.0 km) slowness anomalies are so weak that this layer is considered essentially homogeneous. Thus there seems to be no reason to add more layers to the model which besides would give a depth range far exceeding the array aperture of 3 km.

Discussion

From the geology of the NORESS siting area our working hypothesis in discussing the seismic results is that the observed reflectors/anomalies are tied to differences in physical properties between granite/rhyolite and gabbro at least for the uppermost one at ca 1.1 km (layer 1). On this account we interpret this reflector as the underside of an intruding gabbro body. From the 3D results the inferred body appears to be steeply dipping northeast-wards, while the profile gives a more moderate northward dip. Note that these results are not in conflict because the profile is not perpendicular to the strike. According to the geological map a reflection from the top of the gabbro intrusion should possibly be present in the profile section. However, the quality of the upper 2-300 meters of the section is poor due to interference from the dominant direct waves.

The western and southern parts of the NORESS siting area appears to be rather homogeneous in layer 2. The 3D results imply that granite/rhyolite rocks dominate here in view of the relative low velocities and this hypothesis is consistent with the local geology. On the other hand, relative high velocities persist in the north-east, and hence tied to a thickening of the inferred gabbro body. This interpretation implies that the 1.7 and 2.5 km reflectors are unlikely to be associated with a granite-rhyolite/gabbro sandwiching structure. In short, the origin of the two deeper reflectors remain obscure with the data at hand and we can only regret that there is no profiling perpendicular to the dominant strike direction. However, we note that observations of seismic reflectors in the crystalline crust are widespread although their geological counterpart often remain diffuse (e.g., see Larsson and Husebye, 1989).

In the bottom layer the 3D anomalies are weak and besides cannot be given any geological significance. To summarize the discussion so far; the 3D anomalies are interpreted in terms of a gabbro body in the north-east quadrant of the array siting area thickening towards the north-east. The profiling data seemingly just sample the flank of a mushroom-like intrusive body.

In the profiling results there is indication of a weak reflector at ca 6 sec TWT (Mykkeltveit, 1987 - not shown in Fig. 2) or equivalently at a depth of ca 18 km. This depth is ca 6 times larger than the NORESS aperture for which there is no resolution in the 3D analysis. However, in 3-component wavefield studies (e.g., see Christoffersson et al., 1988) using NORESS data occasionally SV-wavelets are observed at ca 2 sec after the first P-onset and the corresponding 'conversion' boundary would be about 18 km. Also, gravity studies over the Oslo Graben (Wessel and Husebye, 1987) implies the existence of an intrusive, magmatic body at this depth range.

Finally, to what extent should we really expect overlapping results using rather different mapping techniques? Reflection profiling essentially maps discontinuities in acoustic impedance along near horizontal planes using high frequency (100-250 Hz) reflected waves and hence good depth resolution (within 50 m). With 3D imaging, using direct waves from distant sources in the frequency range 2-10 Hz, we map relative long wavelength (of the order of 1 km) velocity variations. The inherent smoothing involved would naturally reduce velocity anomalies compared to those for well separated gabbro/granit bodies. In the NORESS siting area it is not easy to reconcile reflection and 3D imaging results - and in this respect being hampered by very sparse reflection coverage - most needed is a profile perpendicular to the NW strike direction.

Conclusions

In this study we have demonstrated that even though seismic profiling and 3D inversion results seemingly are very different the two methods actually provide complementary information to the geological interpretation. While the reflection data maps rock boundaries with high resolution, the 3D imaging data provide information on velocity variations helping to classify the structural volumes and to indicate their spatial extension. Further profiling remains desirable for a more detailed mapping

of the structures and for a better comparison of the two methods.

The seismic results together with local geology information strongly imply that the north-eastern part of the NORESS siting area is underlain by a shallow gabbro intrusion possibly mushroom shaped and thickening towards the north-east. We intuitively expect that this body would influence the wavefield as observed across the array and this appears indeed to be the case. For example, Christoffersson (pers. communication) reports a buckling of the P wavefront as reconstructed independently from estimated slowness vectors using 3-component stations within the array. Ultimately, we plan to undertake 3D synthetic seismogram analysis to check to what extent the gabbro body beneath NORESS can account for observed P-wave train complexities as observed across the array.

Acknowledgements

This research is supported by the Defence Advanced Research Projects Agency under AFORS Grant AFORS-89-0259 (B.O.R), and by VISTA V6222 (E.S.H.). We would also like to thank S. Mykkeltveit for making the profiling results available to us.

References

- Aki, K., A. Christoffersson and E. S. Husebye (1977). Determination of the Three-Dimensional Seismic Structure of the Lithosphere, *Journal of Geophysical Research*, 82: 277-296.
- Christoffersson, A, E. S. Husebye, and S. F. Ingate (1988). Wavefield Decomposition Using ML Probabilities in Modeling Single Site 3-Component Records, *Geophysical Journal*, 93: 197-213.
- Harris, D. B. (1982). Uncertainty in Direction Estimation: A Comparison of Small Arrays and Three-Component Station, *Lawrence Livermore National Lab., Tech. Rep. UCID-19589*, Livermore, Calif.
- Larsson, F. R., and E. S. Husebye (1989). Crustal Lamination – Skagerrak Tectonic Province, m/s submitted to *Tectonophysics*.
- Mykkeltveit, S. (1987). Reflection Profiling in the NORESS Siting Area. In: L. B. Loughran (ed.), *Semiannual Technical Summary, NOR SAR Scientific Report No. 1-87/88*, Kjeller, Norway.
- Nolet, G., ed. (1987). *Seismic Tomography, with Applications in Global Seismology and Exploration Geophysics*, D. Reidel Pub. Comp., Dordrecht, The Netherlands.
- Ruud, B. O. (1988). *Seismic Inversion Experiments on the Basis of Crustal Phases Observed from the NORESS Array*, Cand. Scient. thesis, Inst. of Geology, Univ. of Oslo, Norway.
- Skålvoll, H. (1988). VALER 2016 III, and ELVERUM 2016 IV, preliminary bedrock maps 1:50000, Geological Survey of Norway (NGU), Trondheim, Norway.

Spencer, C., and D. Gubbins (1980). Travel-Time Inversion for Simultaneous Earthquake Location and Velocity Structure Determination in Laterally Varying Media, *Geophys. J. R. astr. Soc.*, 63: 95-116.

Wessel, P., and E. S. Husebye (1987). The Oslo Graben Gravity High and Taphrogenesis, *Tectonophysics*, 142: 15-26.

Figure captions

Figure 1: Geological map over the NORESS array and its vicinity (array center at 60.74°N and 11.54°E). The array seismometers used in the inversion experiment are marked with black dots and the reflection profile line with a 'P'. Typical density and P-velocity values for granite and gabbro are (2.66 g/cm^3 , 5.9 km/s) and (2.99 g/cm^3 , 6.7 km/s) respectively. The physical properties of rhyolite are expected to be close to those of granite.

Figure 2: Section of the reflection profile showing the upper 1 sec TWT (down to ca 3 km). TWT is two-way-traveltime in seconds. The three dominant reflectors referred to in the text are marked R_1 , R_2 and R_3 . The traces have been filtered in the 100-250 Hz passband.

Figure 3: Slowness anomalies obtained from inversion. The lower numbers in each block are standard deviations. Both anomalies and uncertainties are given in msec/km relative to the reference layer velocities (5.8, 5.9 and 6.0 km/s). A slowness anomaly of +3 msec/km would thus correspond to a velocity change of ca -0.1 km/s. Labels H and L indicates high and low *velocity* regions. Only significant anomalies, i.e., greater than standard deviation are hatched. Note the differences in length scale for each layer (indicated in the figure). The lateral block sizes are 0.6 km for layer 1, 0.9 km for layer 2 and 1.5 km for layer 3.

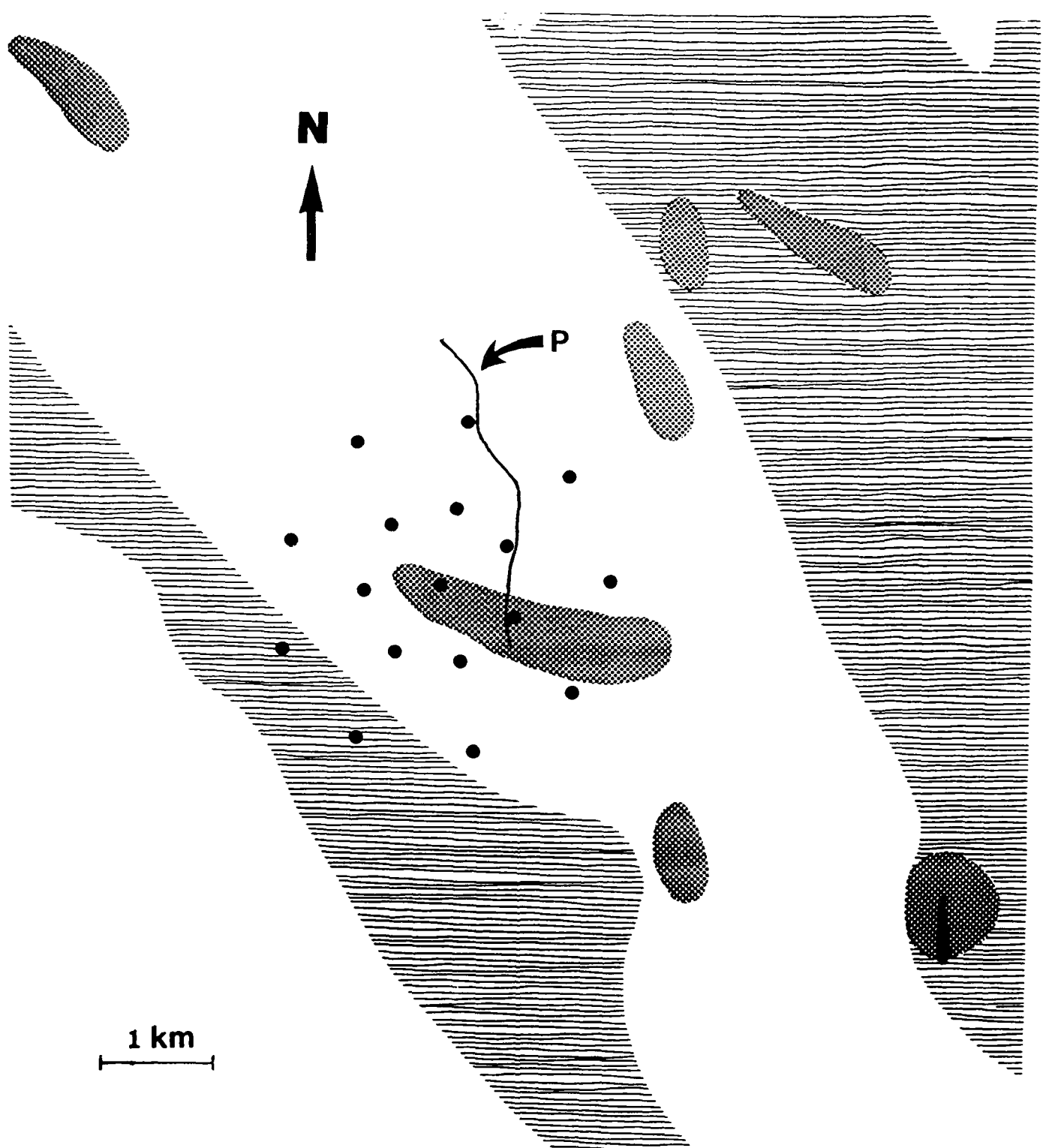


Figure 1:

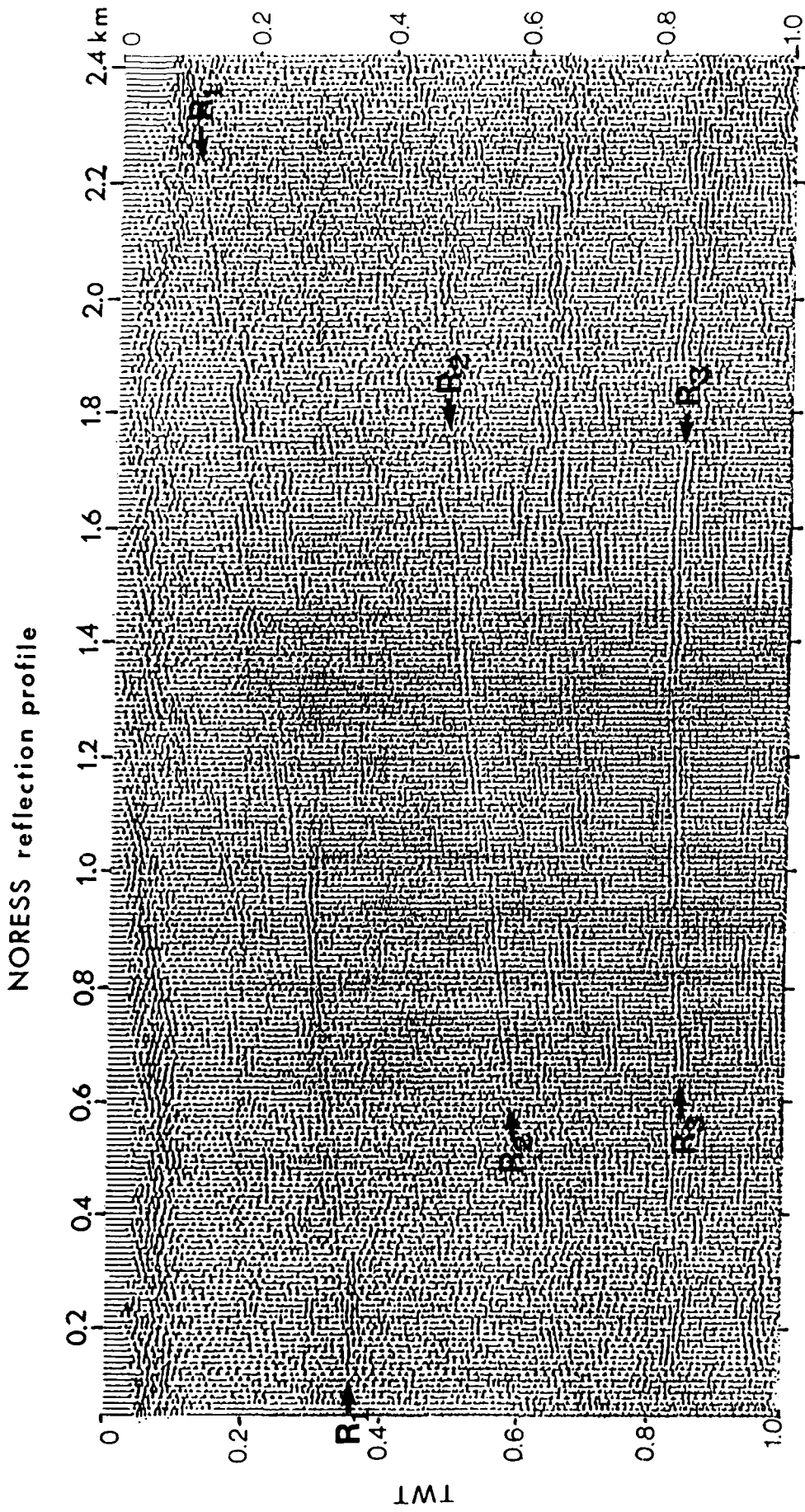


Figure 2:

Slowness anomalies and standard deviations in msec/km

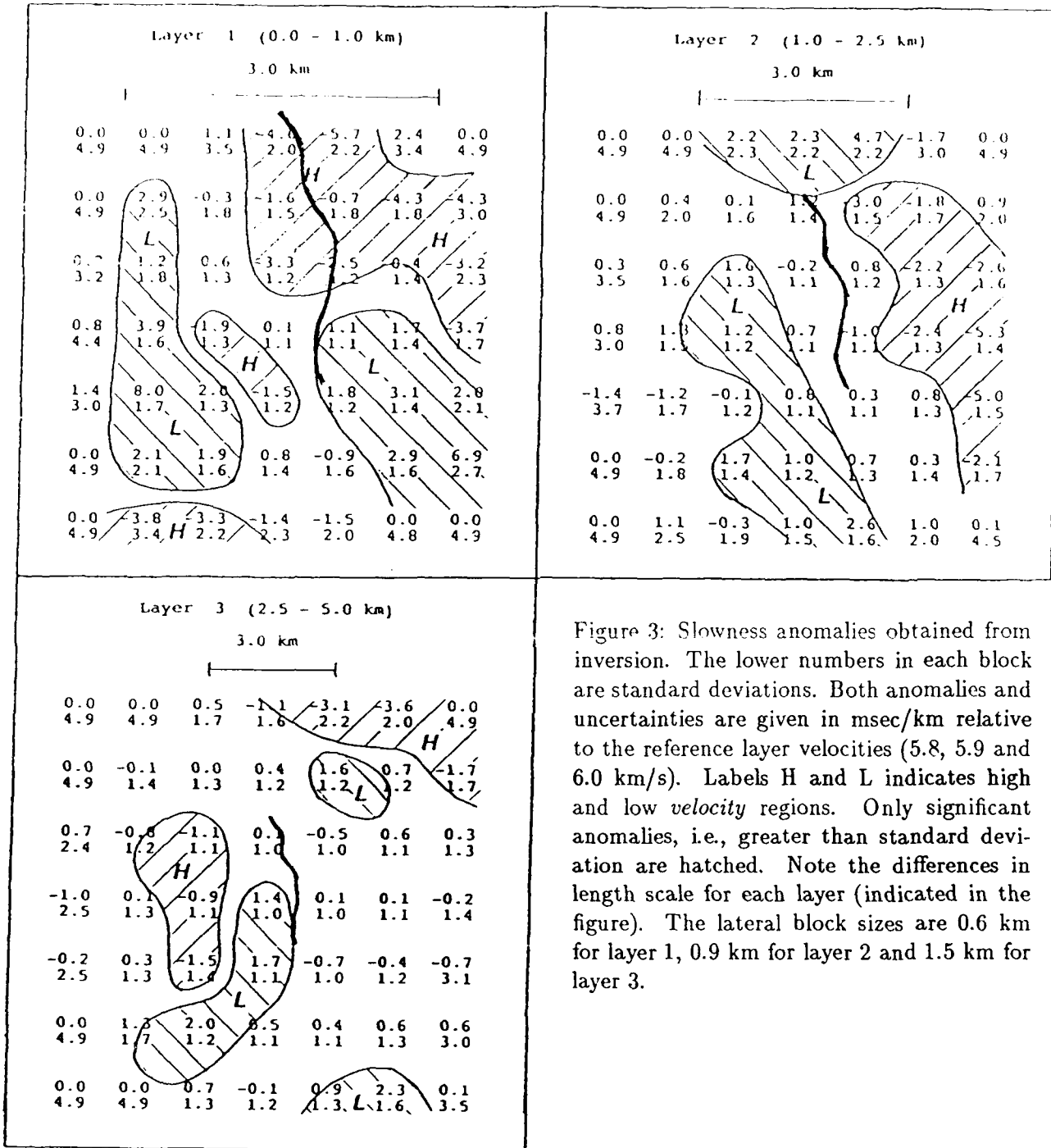


Figure 3: Slowness anomalies obtained from inversion. The lower numbers in each block are standard deviations. Both anomalies and uncertainties are given in msec/km relative to the reference layer velocities (5.8, 5.9 and 6.0 km/s). Labels H and L indicates high and low velocity regions. Only significant anomalies, i.e., greater than standard deviation are hatched. Note the differences in length scale for each layer (indicated in the figure). The lateral block sizes are 0.6 km for layer 1, 0.9 km for layer 2 and 1.5 km for layer 3.

**THE SOUTH SCANDINAVIAN CRUST - STRUCTURAL COMPLEXITIES
FROM SEISMIC REFLECTION AND REFRACTION PROFILING**

J.J. Kinck¹⁾, E.S. Husebye¹⁾ and C.-E. Lund²⁾

¹⁾ Dept. of Geology, University of Oslo, Norway.

²⁾ Dept. of Geophysics, Uppsala University, Sweden.

ABSTRACT

Pioneering work on mapping the Scandinavian crust commenced in the early 1960s and since then numerous profiling surveys have been undertaken, particularly as part of the on-going EUGENO-S project. However, the most significant contribution to mapping crustal structural details came from the M/V Mobil Search cruises in the Skagerrak Sea and off the West coast of Norway (reflection profiling 16 sec TWT). In short, all past and present crustal profiling results have been integrated to produce detailed maps of Moho depths and crustal thicknesses for the S. Scandinavia. The thinnest crust is found in the North Sea and Skagerrak (approximately 20 km), while east-central Sweden feature very thick crust (app. 50 km). Other interesting features are the apparent correlation between crustal thinning and sedimentation / subsidence, documented magmatic activity, earthquake occurrences and the tectonic age of the crust. Moho depth and the crustal thicknesses clearly mirror the tectonic evolution and the present structural features of the region investigated.

1. INTRODUCTION

Crustal studies became popular with seismologists some 3 decades ago. In the early sixties the prime motivations were to map Moho depths, deduce whether the number of crustal layers should be 2, 3 or 4, and investigate to what extent velocity reversals took place. Now as before the most popular and also the most precise tool for such studies are tied to seismic surveys, i.e. refraction and/or wide angle reflection profiling. However, during the last decade improved instrumentation in combination with sophisticated forward and inverse modelling has permitted more detailed mapping of crustal structures. Though 1-D line profiling is limited to identifying gently undulating velocity contrasts in the crust and below Moho, and naturally depths to major structural boundaries. Significant improvements in mapping came with the advent of seismic tomography (e.g., see Aki et al., 1977) and the adaption to crustal studies of the seismic reflection techniques used in oil prospecting, (e.g. the USA COCORP, and the UK BIRP programs). The use of these mapping techniques provide vastly improved structural images of crustal heterogeneities, but their interpretation in a geological context remains non-unique. For example, the abundance of crustal reflectors or laminae observed in deep crustal reflection surveys can be explained in terms of petrological, geochemical, hydrostatic or magmatic discontinuities or simply low-angle faults (Larsson and Husebye, this volume).

The crustal study developments in Scandinavia have a clear parallel to those taking place elsewhere; it started with refraction profiling in the early sixties, extended to wide-angle profiling and tomography, and recently culminated with approximately 10,000 km of deep seismic reflection data (16 sec TWT) collected during M/V Mobil Search cruises in Norwegian off-shore areas in 1987. Our part of this project was the Skagerrak Sea survey, totaling 1730 km of intersecting profiling lines. The shotpoint map is shown in Fig. 1 (Husebye et al., 1988). The crustal information extracted from these marine data are the

main topic of this presentation. Fortunately, it is fairly easy to integrate the Skagerrak survey into seismic profiling efforts of the past, thus the study was extended to comprise the whole of south Scandinavia. As we consider it important to attempt to interpret geophysical results in a geological context, we therefore start with a brief overview of the geological evolution of not only south Scandinavia but the whole of Fennoscandia.

2. TECTONIC EVOLUTION OF FENNOSCANDIA WITH EMPHASIS ON THE SOUTH SCANDINAVIAN AREA

A structural map of south Scandinavia is shown in Fig. 2. Major structural features and evolutionary details are as follow:

2.1 BALTIC SHIELD STRUCTURES

The Baltic Shield, comprising mainland Norway, Sweden, Finland, the Kola peninsula and USSR Karelia, was mainly formed or accreted during four orogens (enhanced in Table I) essentially confined to the time period 3100 to 1500 Ma. Later orogens have largely reworked the existing crust, adding little if any new material to the craton. The shield is roughly zoned, in the sense that the oldest crust is found in NE Finland and the Kola peninsula and the youngest in southern Norway. While the oldest crust stems from the Saamian orogen (3100 - 2900 Ma), most of the Baltic Shield was formed during the following three orogens; the Lopian (2900 - 2600 Ma), the Svecofennian (2000 - 1750 Ma) and the Gothian (1750 - 1500 Ma).

The Lopian and Svecofennian orogens had a northwest-southeasterly front while the Gothian was more north-south (Berthelsen and Marker, 1986). According to Poorter (1981) and Stearn and Piper (1984), the Baltic Shield was rotated clockwise with respect to Laurentia during the interval 1190 to 1050 Ma. This also account for the complexity of the

Gothian orogen (Gaál and Gorbatshev, 1987).

The Protogine zone (PZ in Fig. 2) in south-central Sweden was formed by episodic faulting accompanied by magmatic intrusions. Main phases of activity took place between 1650 - 900 Ma. Today it constitutes a sharp boundary between the highly metamorphic and foliated SW Scandinavia (reworked during the Grenvillian orogen) and the well preserved Svecofennian terrains to the east. The effect of the later Sveconorwegian orogen was a thorough reworking of the crust as far east as the Protogine zone.

During the Caledonian orogen (600 - 400 Ma) large areas of the precambrian crust of west Scandinavia became concealed beneath nappes, consisting of disconnected precambrian basement fragments with younger sediments on top. This orogen affected the precambrian basement progressively in a westward direction by reworking and foliation. The Oslo Graben (OG) is an intracontinental rift, cutting through the younger parts of the Baltic Shield and is dominated by large amounts of volcanic material, dating from 305 Ma in the south to 245 Ma in the north (Neumann et al., 1986).

We have only given a rough outline of the geological evolution of the Baltic Shield for the simple reason that such information is difficult to correlate with seismic/geophysical data. The fundamental problem is that past deformations are far better preserved geologically and geochemically than in geophysical anomalies reflecting the present tectonic environment.

2.2 DENMARK AND ADJACENT SEAS.

Denmark and adjacent seas belong to the mobile part of paleo-Europe, and as such appear to be younger than the stable shield areas to the north. How and when these areas became attached to each other, remains somewhat obscure. Berthelsen (1987) has suggested that a continental-continental collision took place. Denmark and adjacent seas have been subject to more recent and severe deformations than the shield areas to the north. This is demonstrated in a Skagerrak basin subsidence analysis by Pedersen et al. (this volume), who also reconstructed crustal thicknesses to precambrian times. From Fig. 2 we see that this area is dominated by three main features, namely the Fennoscandian Border Zone (FBZ), the

Norwegian-Danish Basin (NDB), and the Ringkøbing Fyn High (RFH). The FBZ is a NW to NNW trending fault zone separating the Shield and the European platform. Even though the FBZ has been repeatedly reactivated since precambrian times, the movements along the zone appear modest (Liboriussen et al., 1987; Kornfælt and Larsson, 1987). The sediment thicknesses in the NDB are large, exceeding 10 km in NW Jutland. Subsidence probably started in early Paleozoicum but the main pulse took place during the Triassic. The sediments here are dominated by thick Zechstein evaporites. Subsequent halokinetic movements resulted in domes and diapirs in the NW part of the basin. The RFH is an area of elevated precambrian basement and is subdivided into several blocks by N-S trending grabens such as the Horn Graben. RFH appears to have been elevated in the Carboniferous while taphrogenesis has been related to the late Carboniferous - early Permian Hercynian movements (Ramberg and Spjeldnæs, 1978; EUGENO-S Working Group, 1988). A brief overview of the evolution of this area is given in Table II. A very extensive literature exists on the evolution of Denmark and adjacent seas, and key references here are Fluh and Berthelsen, 1986; Michelsen, 1976; Ziegler, 1981 and 1982 and Pegrum 1984a and 1984b.

3. SEISMIC PROFILING DATA AND THEIR ANALYSIS

Initially, the intention was to restrict the crustal analysis to the M/V Mobil Search profiling lines in the Skagerrak Sea (Fig. 1) where reflection records are of exceptionally high quality. The opportunity for tying-in the Skagerrak crustal results with those obtained from nearby land profiling surveys made it natural to extend the scope of our crustal synthesis to the whole of S. Scandinavia. This offer an unique opportunity to examine crustal variations across vastly different tectonic provinces. The Skagerrak survey is dealt with in detail below while for the other profiling surveys (shown in Fig. 3) we have used the relevant results as summarized in reports and publications (see Table IV).

3.1 THE M/V MOBILE SEARCH SURVEY - DATA AND ANALYSIS

During the Mobile Search cruise of one month in Winter 1987 (Husebye and Ro, 1987; Husebye et al., 1988) 1730 km of seismic reflection profiling was accomplished. A dual sampling rate of 4 and 8 msec was used, and record length was 16 sec TWT giving an effective penetration depth of 50-60 km. On-board data processing at 8 msec and the resulting seismic sections constitute the basis for our crustal analysis in the area. Data quality is exceptionally high, and may be further enhanced by reprocessing using more refined techniques than permitted on-board. Such a project is now being completed with financial support from oil companies.

The first step in analysis/interpretation of the individual profiles was to identify major reflectors in the sedimentary column and crystalline crust. Guided by other surveys and works in the area, notably that of Haatvedt and Nerby (1984) and bore-hole log information from the Danish Geological Survey, reflectors were tied to the following horizons: Moho, Precambrian basement, top Permian, base and top Zechstein, inter-Jurassic erosional plane, base and top Chalk and base Tertiary and Quarternary. Depth conversion was achieved using standard techniques and velocities as listed in Table III. The results of the analysis are illustrated in Fig. 4 and 5 for OG-2 and 12 and 5,7 and 13 respectively. On the basis of individual profiling results, maps of Moho depths and thickness of crystalline crust have been constructed and are displayed in Figs. 6 and 7.

A few clarifying comments to these maps apply; the quality and the reflector sharpness varies from line to line and along individual lines. In the southernmost profiles halokinetic make it difficult to extract information from reflectors below Zechstein; this problem is most pronounced on OG-4. In north Skagerrak a combination of thin sediments and a hard bottom with a rough relief make discrimination between the paleozoic sediments and basement often non-unique. In other words, the exact position of the southward continuation of the Oslo Graben (OG), that is the Oslo Rift (OR), is somewhat diffuse. On some profiles Moho can be tied to a sharp and well defined reflector, characterized by 2 cycles of high amplitude. On others, there are bands or several reflectors in the appropriate

depth range. This is not tied only to line location but also to profile strike direction. The sharp reflectors, like those on OG-13, have been used as markers for identifying Moho in reflector bands at intersections with other lines, such as OG-12. A basic problem here is naturally that the Moho discontinuity is not uniformly sharp over the entire area. However, the correlation between OG-12 and OG-13 indicates that Moho should not be defined as the bottom of a general and broad reflective zone which seems to be the tendency in many recent works in deep seismic reflection profiling (e.g., see Matthews and Cheadle, 1986).

To summarize, data processing tied to 8 msec sampling is a bit coarse for the sedimentary column but considered adequate for identifying major discontinuities and detailing velocity distributions. The final outcome, that is Moho depth estimates, would as mentioned depend on choice of reflector(s) taken to be representative for this prime discontinuity. It is not always sharp (Barton, 1986) but by harmonizing reflector "pickings" at line intersections a reasonable consistent Moho isopac map has been obtained. Errors here are considered unlikely to exceed 0.5-1 sec TWT or equivalently that Moho depth estimates are correct within ± 3 km, while the relative error would be less. In the south Moho reflectors are more diffuse and we may even have a more bumpy Moho across the Fjerritslev Fault Zone (FFZ), and the depth errors could be slightly larger here. During reprocessing special attention would be given to this and similar problems. Finally, upper/lower crust transition is not a first order discontinuity in Skagerrak, as reflector(s) at appropriate depth range have not been identified. However, from extensive laminae analysis, the thickness of the upper brittle and lower ductile parts of the crust appears to be roughly the same, that is 50 ± 10 per cent (Larsson and Huseby, this volume).

3.2 SEISMIC REFRACTION AND WIDE ANGLE PROFILING SURVEYS

In the past numerous seismic profiling surveys have been conducted over various parts of south Scandinavia - many of those bordering on the Mobile Search profiling lines in Skagerrak. Details on these profiles are given in Fig. 3 and in Table IV. Note that some of the oldest profiling records (shot prior to 1971) have been reinterpreted by Kværna (1984),

these are profiles I, K and L. The Moho depth estimates from all these surveys plus those from Skagerrak has been integrated, the final result being the south Scandinavian Moho depth and crustal thickness maps in Figs. 6 and 7. Noteworthy, the Skagerrak results blend well with those of bordering profiles in Norway, Sweden and Denmark - differences being within ± 2 km. Naturally, in drawing the Moho depth map some cosmetic smoothing has been introduced in part justified by covering gaps between adjacent profile lines. Our mapping should be considered an evolutionary process i.e., it is updated as new profiling results become available.

4. RESULTS

The Moho depth and the crustal thickness may in comparison to the structural features indicate the relative correlation between these features and thus provide a clue to the evolution of the region under investigation.

The main features of the Moho depth map (shown in Fig. 6) is a pronounced Moho elevation in Skagerrak, Jutland and off-coast west Norway, which geological counterparts are sedimentary basins, including the NDB. This is expected as basin formation is a direct consequence of extension processes or crustal thinning (e.g., see Pedersen et al., this volume). In particular, there is a marked Moho elevation of approximately 5km associated with the OR/OG system, being somewhat broader than the corresponding surface structural features. The crust underneath the Caledonides of west Norway is relatively thick, while the Western Gneiss Region is thin. There is a similar feature of thicker crust, also related to the Caledonides on the British side of Viking Graben/Central Graben (VG/CG), but a correlation is speculative (S. Klemperer pers. comm.). Pronounced crustal thinning take place off S. Norway and SW. Sweden. In the latter case the trends of the FFZ/FBZ seem to be dominating. The RFH stands out sharply as a thick crustal block. The deepest Moho is found in southeast Sweden with depths around 50 km. The Moho trends in Skagerrak seem to be influenced mainly by the OG/OR and the NDB. The FFZ/FBZ seem to be of less

importance in this area, but its more easterly segments (in the Kattegat area) appear to have a counterpart in Moho undulation. The oldest part of the Baltic Shield, the area east of Protogine Zone(PZ) or the Sveconorwegian Front(SNF), is relatively uniform with depths exceeding 40 km and only minor gradients.

The thickness of the crystalline crust is displayed in Fig. 7. The thinning in Skagerrak and Denmark is pronounced with a minimum in NDB of about 18 km. Again the pattern is complex with trend directions coinciding/following FFB/FFZ, Swedish west coast, the OR/OG and finally one paralleling the SE coast of Norway. The RFH is even more pronounced than in the Moho depth map, and an off-shore westward extending "tongue" of the Caledonide province is clear. The extreme localized thinning near Bornholm (22 km) coincides with a southward shift in FFZ. Areas not affected by post-Cambrian subsidence and rifting coincides generally with the area where the crust is thicker than 36 km.

5. OTHER GEOPHYSICAL AND GEOLOGICAL OBSERVATIONS

It is prudent to consider/discuss our crustal results in the framework of other geophysical and geological observations, and a brief summary of these are given below.

5.1 VOLCANIC ACTIVITY IN SOUTH SCANDINAVIA: CARBONIFEROUS TO PRESENT

The western part of S. Scandinavia has experienced volcanic activity as shown in Fig. 8. Paleozoic magmatism is mainly related to the formation of the Oslo Rift (OR) and the Fjerritslev Fault Zone (FFZ). Manifestions on land are dykes in S. Scandia (Bergström, 1982; Klingspor, 1976) and of dykes and magma outcrops in the Oslo Graben (OG) (Neumann et al., 1986; Ramberg and Spjeldnæs, 1978; Ramberg and Larsen, 1978). In Denmark and Danish North Sea magma of this age have been located in some wells

(Holmsen, 1959; Rasmussen, 1974). Mesozoic volcanism is apparently confined to S. Scandia and the FFZ (Bergström, 1982; Klingspor, 1976), but possibly also in the Egersund Sub-Basin (58N:6E) (Furnes et al., 1982). Although there is no ultimate evidence of Tertiary volcanic activity in Skagerrak, there are indications. For example, analysis of ash layers of Paleocene-Eocene ages in Denmark, imply that likely source areas should be located within 100-200 km bearing N-NE from Limfjord (LF in Fig. 8). A few layers also indicate a NW-W bearing according to Nielsen and Heilmann-Clausen (1988), although the magmatic source(s) have not been found. Other investigations, notably using geophysical data (Åm, 1973; Hovland, 1987) and dredging (Noe-Nygaard, 1967) give candidate locations as marked on Fig. 8 with age ranges from Permian to Tertiary.

In summary, evidence of volcanic activity throughout Carboniferous to present have been found and is essentially confined to areas affected by rifting and subsidence, and hence to areas with thin crust (thicknesses less than about 30 km). West coast of Sweden and the northern part of OG (Fig. 8) is exceptional here with crustal thicknesses of approximately 36 km.

5.2 CRUSTAL VELOCITY - DEPTH DISTRIBUTIONS

Crustal velocity plots from refraction and wide-angle lines (Fig. 9) show first and/or second order discontinuities in central parts of the crystalline crust. On the Larvik - Lysekil profile and the northern part of E-4 there are two discontinuities, the upper one at approx. 14 and 12km respectively. Even though the P-velocity depth distribution in the crust is not well constrained in general this depth range coincide with the onset of laminae (Larsson and Husebye, this volume), tentatively taken to mark the transition from the upper brittle to the lower ductile crust. Similar results have been reported by Wever (1989). It seems then that the upper and lower crust is roughly equal in thickness here. Relativ pronounced velocity discontinuities are found along the Fennolora and the Fedje - Grimstad profiles. Areas with intermediate velocities (7.3-7.9 km/s), that are higher than normal crustal velocities and less

than typical sub-Moho velocities, are located in areas with truly thick crust along the Fennolora profile. Similar features have been observed for SW. Norway (S. Deemer, pers.comm.).

5.3 EARTHQUAKE (EQ) LOCATIONS - CRUSTAL THICKNESSES

The Nordic EQ database (Seismological Observatory, Helsinki) has been used. We have briefly examined the epicenter distribution versus our estimated crustal thicknesses. The time period covered by this database is from 1375 to present, a natural subdivision here is: i) Historical data: 1375 - 1889. ii) Macro seismic data: 1890 - 1950. iii) Instrumental data: 1951 - present. For example, historical data are generally of poor quality with most occurring EQ left unreported and at least larger EQ having unreliable epicenter locations. Macroseismic data are of better quality reflecting information on felt EQ through circulation of questionnaires (e.g., see Husebye et al., 1978). Instrumental data are relative superior to the other data sets, particularly regarding detectability of small events, and also those located off-shore. Both historical and macroseismic epicenter locations are landward biased. Among the four hypocenter parameters; focal depth is the least reliable, and often a default value of 15 km is used even for instrumental data.

This being said, we have plotted epicenter locations as a function of crustal thickness both on a map (Fig. 10) and also in a histogram fashion (Fig. 11). Indeed, there is a striking correlation between EQ locations and crustal thicknesses which are even more pronounced for large magnitude events. A high EQ concentration in W. Norway and off the west coast is obvious from Fig. 10. There are also some events in south-central Sweden but these are mainly of small magnitude ($M_l < 3.0$). Most events are located in areas relatively recently subjected to extension where the crust is thin and/or the crustal thickness gradient is high, this is even more striking for the largest earthquakes. The same phenomenon is observed for continental crust on a global scale as demonstrated by Johnston (1989).

5.4 CRUSTAL THICKNESS - TECTONIC AGE

The crustal thickness appears to be increasing as a function of tectonic age. The crustal thickness has been sampled evenly and using the age tied to the latest period of major tectonic activity for a given area. For the Archean period the data have been taken from Luosto and Korhonen (1986), giving rather few points compared to the other periods/areas. Fig. 13 and Table V contain the results for the area investigated and reveal a marked thickening of the older parts of the shield, except for a minor thinning in the (oldest) Archean province. This has been observed in Australia as well (Drummond and Collins, 1986). Meissner (1986) has expressed crustal thickness as a function of age using the relation: $Z=25\log t-32$, where Z =thickness and t =age in Ma, using global data. A linear function like $Z=8t+31$ where Z =thickness and t =age in Ga gives a reasonable fit to our data, as shown in Fig. 13 together with that of Meissner. It appears that after about 1500 Ma the continental growth terminated, that is accretion of microcontinents and/or continental fragments essentially ceased (e.g., see Berthelsen and Marker, 1986). There also appears to be a limit to crustal thickness growth over time as discussed by Warren (1989). The essence of current hypothesis is that during crustal cooling in shield areas an instability is created in the lower crust in terms of a modest density increase due to phase transformation. The effect is a presumed mass exchange between the lower crust and the upper mantle, thus limiting crustal growth to a thickness of 50 - 55 km.

5.5 GRAVITY

The long wavelength Bouguer gravity map of the area is displayed in Fig. 14 (Balling, 1984). It exhibit a generally smooth picture with some positive feature in northern Skagerrak and one of the Swedish west coast with a NW trend, see also Wolf, 1984. The dominating feature is a marked negative anomaly (-80 mgal) over western Norway Caledonides, and thus coincides with sub-Moho Pn and Sn low velocity anomalies (Bannister et al., this volume). This and the fact that the gravity/crustal thickness are poorly correlated in this area implies a sub-Moho mass deficit. The origin of this mass deficit is tentatively

ted to the Caledonide collision per se and/or the opening of the Norwegian Sea 58 Ma ago.

6. SUMMARY AND CONCLUDING REMARKS

The oldest part of the Baltic Shield, east of the PZ, is thick and relatively undisturbed. The Moho depth and the crustal thickness varies from 40 to 50 km, and their gradients are rather small, with the exception of the southernmost part of Sweden.

In the southern part of Kattegat the FFZ/FBZ plays an important role, and these trends are dominating both the Moho depth and the crustal thickness map. The Moho depth varies from 32 to 36km across the zone and its gradients are steep. This is even more pronounced on the crustal thickness map. The FFZ/FBZ loses importance westwards as the Moho depth and crustal thickness variations get smaller, and the FFZ/FBZ covers a broader area.

In south Skagerrak the NDB seems to be the dominating feature with a generally elevated Moho, thin crust, small gradients and no dramatic changes in the westward direction before the CG/VG. However, the subsidence history north and south of the FFZ is different as demonstrated by Pedersen et al. (this volume).

Further north in Skagerrak the Moho depth and crustal thickness are dominated by the OR/OG. The Moho elevation is about 5 km. The OR appears to be divided in two parts, a northern dominated by volcanic activity and large amounts of volcanic material extruded during a rather short period of 40-60 Ma (Neumann et al.,1986). The large volumes of extrusives and the elevated Moho would indicate a mantle source as the prime driving force for the OR. This also agrees with the models for mantle plumes put forward by Neugebauer (1983). Also Lynch and Morgan (1987) argues that the prime factor controlling rifting of continental crust is variation in the geotherm.

The lateral movements along the FBZ/FFZ is estimated by several authors to be in the order of 10-20 km (Liboriussen et al.,1987; Anonymous, 1988). These movements may have controlled the southern part of the OR where large scale block faulting have been observed (Husebye et al., 1988); see also Fig. 4 and 5.

The tongue of thicker crust at the west coast of Norway coincides with the Caledonides. It terminates towards the CG/VG in the North Sea. A similar feature is found on the British side of the CG/VG as mentioned above.

Volcanic activity throughout Carboniferous to present is confined to areas affected by rifting and thin crust.

Velocity discontinuities coincides with the onset of laminae, taken to mark the transition between the upper brittle and the lower ductile crust.

EQ occurrences show that most events are located where the crust is thin and/or the gradient is steep. This is even more pronounced for the high magnitude ($m_l > 3.0$) events.

Crustal thickness increases with age until about 2000 Ma and then level off or is slightly diminishing, and apparently no new crust has been accreted after about 1500 Ma. However, crustal thicknesses seemingly reflect tectonic age as the Sveconorwegian (1200 - 850 Ma) crust is relatively thin being deformed in post Cambrian times.

The long wavelength Bouguer gravity have a marked negative anomaly, this coincides with the Caledonides. Together with Pn and Sn low velocity anomalies this indicate a sub-Moho mass deficit.

This study has been aimed at presenting an overview over currently available geological and geophysical (seismic) information bearing on the crustal structures in S. Scandinavia and adjacent areas. In particular, crustal thickness and Moho depths over this region have been contoured at the 2 km level. There is an obvious correlation between the various geological and geophysical features but on the other hand such relationships are most difficult to quantify. We have not attempted to do this for the simple reason that the underlying geodynamic processes deforming the crust/lithosphere are not well understood. These are indeed intriguing problems where progresses have been slow despite much research efforts over the last decade. Hence we limited the scope of our study to presenting present crustal information which we consider to be a good starting platform for geodynamic modelling exercise now being contemplated.

ACKNOWLEDGEMENTS

We express our gratitude to Mobil Exploration, Norway Inc., who made the M/V Mobil Search available for the Skagerrak survey, and to the captain and crew for their dedication during this survey. For cruise management, surveying strategy and processing, the support of Mobil representatives M. Solli (Stavanger), B. Warner and R. Frowe (both Dallas) are gratefully acknowledged. For stimulating discussion during this work we wish to thank S.C. Bannister, F.R. Larsson, T. Pedersen, S.E. Pettersson and H.E. Ro. This research was supported by grants from the Norwegian Research Council for Science and the Humanities (RNF/NAVF; D 48.50.10), VISTA (V:6217), and the Defence Advanced Research Projects Agency under AFORS Grant-89-0259.

TABLE I**TECTONIC EVOLUTION OF THE BALTIC SHIELD**
- MAJORE DEFORMATION PHASES

OROGEN/AREA	TIME (MA)	MAIN FEATURES
Saamian	3100-2900	Basement of late archean greenstone belt.
Lopian	2900-2650	Generated large volumes of new crust.
Svecofennian	2000-1750	Large volumes of igneous rocks (1880 ±20 Ma).
Trans Scand. Igneous Belt	1785-1650	Ensialic spreading.
Sveconorwegian Gothian	1750-1500	Hot lithospheric regime, building the SW. Scandinavian region.
Hollandian	1500-1400	"Interlude" with mafic intrusions.
Sveconorwegian Greenvillian	1250- 900	Rotation of the Shield, complex orogen with large scale reworking of old crust.
Caledonian	600- 400	Collision, trust-Nappe tectonics.
Oslo Graben Oslo Rift	305- 245	Rifting, large volumes of volcanic material, large normal faults.

TABLE II

EVOLUTION OF DENMARK AND ADJACENT SEAS

PERIOD	MAIN FEATURES
Precambrian	Few details due to lack of sediments.
Early Paleozoic	Thick sediment strata in grabens to the NE.
Silurian	Basin subsidence to the SW of FBZ.
Devonian - Carboniferous - Hercynian	Most of Denmark uplifted - erosion. Strong faulting and uplift of marginal basins. The Caledonian orogen of moderate influence - Lower paleozoic strata show no evidence of compressive deformation.
Late Carboniferous - Early Permian	FBZ activated, dextral movement, wrench tectonics; complex faulting and widespread magmatic activity. Rise of RFH and erosion. Taphrogenesis - rifting initiated in Rønne, Oslo and Horn Grabens.
Early Permian	Volcanic activity abated. NDB subsidence. RFH a positive structure.
Triassic	Repeated reactivation of FBZ - transtensional regime. Denmark - crustal extension, rapid differential subsidence, decreasing in late Triassic. Block faulting and subsidence along FBZ. Mantle derived basaltic plugs onshore Scandia.
Cretaceous	FBZ reactivated several times. Volcanic activity. Accumulation of thick sediments in Ålborg and Rønne grabens.
Late Cretaceous - Tertiary	FBZ inversion with a shift from Early transtensional to transpressional regime. Partial uplift often related to the Alpine orogen.

TABLE III**VELOCITIES USED FOR DEPTH CONVERSION.**

Velocity (km/s)	Layer/Period	Lithology/comment
1.46	Water	Brackish, Cold
1.8	Quaternary	Clay, Silt, Sand, Gravel
3.8	Upper Cretaceous	Chalk
3.0	L.Cretaceous-U.Jurassic	Shale/Sand
3.9	L.Jurassic, Triassic	Shale/Sand
5.3	Upper Permian	Evaporites
5.05	Paleozoic	Sediments
6.1-7.0	Precambrian	Crystalline crust
8.1	Sub Moho	

The velocities are based on: Wells: Skagerrak-1 (57 50.6N 9 55E), Skagerrak-2 (57 26N 8 33.1E) and North Sea-3 (57 0.8N 6 10.1E); refraction experiment from the area (Egilson and Husebye, 1989); Faleide, (1984) and processing results from the M/V Mobil Search data (J.E. Lie pers.comm.).

TABLE IV**SEISMIC PROFILING - CRUSTAL MAPPING STUDIES**

Map-ref	Name/Area	Reference	Type
A	Central Graben	Barton and Wood, 1984	Refrac
B	Mobile Search/ West coast of Norway	S. Deemer pers. comm.	W.Refl/ Refrac
C	Møre margin	Olafsson, 1988	ESP
D	Cannobe/S. Norway	Cassell et al., 1983	Refrac
E1-E5	Eugeno-S/ Denmark, Kattegat, SW.Sweden	Anonymous, 1988/ Lund et al., 1987	Refrac
F1-F3	Fennolora S. part	Clowes et al., 1987	Refrac
G	Swedish Lapland	Båth, 1984	Refrac
H	Trondheim-Sundsvall	Vogel and Lund, 1971	Refrac
I	Oslo Trondheim	Kanestrøm, 1971	Refrac
J	Otta - Årsund	Mykkelstveit, 1980	Refrac
K	Flora - Åsnes	Sellevoll and Warrik, 1971	Refrac
L	Fedje - Grimstad	Sellevoll and Warrik, 1971	Refrac
M-N	Oslo Rift	Tryti and Sellevoll, 1977	Refrac
O	Larvik - Lysekil	Egilson and Husebye, 1989	Refrac
P1-P4	NSDP84-01:04 North Sea	Fichler-Fettig and Hospers, 1988	Reflec
NOA	NORSAR, Norway	Berteussen, 1977	Spec.r.
COP	Copenhagen, Denmark	Bungum et al., 1980	Spec.r.
HFS	Hagfors, Sweden		
KON	Kongsberg, Norway		
UME	Umeå, Sweden		
UPP	Uppsala, Sweden		
	Siljan, Sweden	Lund et al., 1988	Reflec
	S.Sweden-Kattegat	Kornfælt and Larsson, 1987	Reflec
	Viking Graben	Hospers and Ediriweera, 1988	Reflec

(Refrac = refraction profiling; W.Refl = wide angle reflection profiling; Spec.r. = long period seismic spectral ratio technique; ESP = expanding spread profile.)

TABLE V

CRUSTAL THICKNESSES VS AGE.

AREA	TIME (MA)	AVERAGE THICKNESS (km)
ARCHEAN	2700-2500	49.3
SVECOKARELIAN	2100-1900	51.5
SVECOFENNIAN	2000-1800	46.0
TRANS SCAN. IGNEOUS BELT	1750-1550	44.3
SVECONORWEGIAN	1200- 850	37.6
SN EAST of OG		39.7
SN WEST of OG		34.5
CALEDONIAN	550- 400	37.3
CALEDONIAN		38.6
WESTERN GNEISS R.		34.1
OSLO GRABEN	305- 245	31.5

References

- Anonymous** 1988: Crustal structure and tectonic evolution of the transition between the Baltic Shield and the North German Caledonides (the EUGENO-S Project). *Tectonophysics*, 150, 253-348.
- Aki, K., Christoffersen, A. and Husebye, E.S.** 1977: Determination of the three-dimensional seismic structures of the lithosphere. *J. of Geophysical Research*, 82, 277-296.
- Balling, N.** 1984: Gravity and isostasy in the Baltic Shield. In: D.A. Galson and S. Mueller (eds.). *Proc. First Workshop on the European Geotraverse (EGT), Northern segment*. European Science Foundation, 53-68.
- Bannister, S.C., Ruud, B.O. and Husebye, E.S.** 1989: Tomographic estimates of sub-Moho seismic velocities in Fennoscandia and structural implications. *Tectonophysics*, this volume.
- Barton, P. and Wood, R.** 1984: Tectonic Evolution of the North Sea Basin: Crustal Stretching and Subsidence. *Geophysical J. R. astr. Soc.* 79, 987-1022.
- Barton, P.** 1986: Earth sciences; Deep reflections on the Moho. *Nature*, 323, 392-393.
- Bergström, J., Holland, B., Larsson, K., Norling, E. and Sivhed, U.** 1982: Guide to excursion in Scania. *Sver. geol. unders.* 54, 1-95.
- Berteussen, K.-A.** 1977: Moho Depth Determinations based on Spectral-Ratio Analysis of NORSAR Long Period P-waves. *Physics of the Earth and Planetary Interiors*, 15, 13-27.
- Berthelsen, A.** 1987: A Tectonic Model for the Crustal Evolution of the Baltic Shield. In: J.-P. Schaer and J.R. Rodgers (eds.), *The Anatomy of Mountain Ranges*. Princeton University Press. Princeton, New Jersey, 31-57.
- Berthelsen, A. and Marker, M.** 1986: 1.9-1.8 Ga Old Strike-slip Megashears in the Baltic Shield and their tectonic implications. *Tectonophysics*, 128, 163-181.
- Bukovics, C. and Ziegler, P.A.** 1985: Tectonic development of the Mid-Norway Continental Margin. *Marine and Petroleum Geology*, vol 2, 2-22.
- Bungum, H., Pirhonen, S.E. and Husebye, E.S.** 1980: Crustal thickness in Fennoscandia. *Geophys. J. R. astr. Soc.*, 63, 759-774.
- Båth, M.** 1984: A seismic Refraction Profile in Swedish Lapland. Report no. 2-84. Seismological Department. University of Uppsala, 1-32.
- Cassell, B.R., Mykkeltveit, S., Kanestrøm, R. and Husebye, E.S.** 1983: A North Sea - southern Norway seismic crustal profile, 733-753.
- Clowes, R.M., Gens-Lenartowicz, E., Demartin, M. and Saxov, S.** 1987: Lithospheric structure in southern Sweden - Results from Fennolora. *Tectonophysics*, 142, 1-14.
- Drummond, B.J. and Collins, C.D.N.** 1986: Seismic evidence for underplating of the lower continental crust of Australia. *Eart Planet. Sci. Lett.*, 79, 361-372.
- Egilson, T. and Husebye E.S.** 1989: An Oslo Graben Experiment - shooting at sea and recording on land. *Tectonophysics*, (m/s submitted).
- Faleide, J.I.** 1984: Geoacoustic modeling of the sea floor - with examples from the Barents sea,

North sea, Skagerrak, Kattegat and Oslofjord. FFI/NOTAT-84/2007, Forsvarets forskningsinstitutt. 82pp.

Fichler-Fettig, C. and Hospers, J. 1988: Deep crustal structure of the Northern North Sea Viking Graben: results from deep reflection seismic and gravity data. Report no. 10. Deep Geology of the Norwegian Continental Shelf. The petroleum centre, NTH, Trondheim, Norway, 1-42.

Fluh, E.R. and Berthelsen, A. 1986: Tectonic evolution and crustal structure in Denmark, and Southwest Sweden. In: R. Freeman, S. Mueller and P. Giese (eds.). European science Foundation 3th. EGT workshop Aug. 1986, 41-51.

Furnes, H., Elvsborg, A. and Malm, O.A. 1982: Lower and middle Jurassic alkaline magmatism in the Egersund Sub Basin, North Sea. *Marine Geology*, 46, 53-69.

Gaál, G. and Gorbatshev, R. 1987: An Outline of the Precambrian Evolution of the Baltic Shield. *Precambrian Research*, 35, 15-52.

Gorbatshev, R. 1985: Basement of Scandinavian Caledonides. In: D.G. Gee and B.A. Sturt (eds.). *The Caledonian Orogen - Scandinavia and Related Areas*. Wiley, New York, 197-212.

Holmsen, P. 1959: Ringe-1. DGF 14, 61-62.

Hospers, J. and Ediriweera, K.K. 1988: Mapping the top of the crystalline continental crust in the Viking Graben area, North Sea. *Nor. Geol. Unders.*, (in press).

Hovland, M. 1987: Tertiary intrusives in western Skagerrak? *Marine Geology*, 78, 175-182.

Husebye, E.S., Ringdal, F., Sandvin, O.A. and Christoffersson, A. 1978: Statistical test theory in the analysis of macroseismic questionnaires. *Tectonophysics*, 49, 161-170.

Husebye, E.S. and Ro, H.E. 1987: Marine Geophysical Survey with R/V Mobil Search - Cruise Report Skagerrak Sea 16 Jan-10 Feb 1987. Tech. Rep., Dept. of Geology, University of Oslo, Oslo, Norway, 1-9.

Husebye, E.S., Ro, H.E., Kinck, J.J. and Larsson, F.R. 1988: Tectonic studies in the Skagerrak province: the "Mobil Search" cruise. *Nor. Geol. Unders. Special Publ.*, 3, 14-20.

Kanestrøm, R. 1971: Seismic Investigations of the Crust and Upper Mantle in Norway. In: A. Vogel (ed.) *Deep Seismic sounding in northern Europe*. Swedish Natural Science Research Council, Stockholm, 17-27.

Klingspor, I. 1976: Rad. age-determining of bas. dol. and rel. syen. in Skåne, South Sweden. *Geol. Fören. i Stockholm Forh.* 98, 195-216.

Kornfält, K.-A. and Larsson, K. 1987: Geological maps and cross-sections of Southern Sweden. Swedish Nuclear Fuel and Waste Management Co. Technical Report 1987-24. Stockholm, 44pp.

Kværna, T. 1984: Reinterpretation of Seismic refraction profiles in the framework of Fennoscandian tectonic evolution. *Cand. Scient. thesis*. University of Oslo.

Larsson, F.R. and Husebye, E.S. 1989: Crustal lamination in the Skagerrak area. *Tectonophysics*, this volume.

Liboriussen, J., Ashton, P. and Tygesen, T. 1987: The Tectonic Evolution of the Fennoscandian Border Zone in Denmark. *Tectonophysics*, 137, 21-29.

Lund, C.-E., Roberts, R.G., Dahl-Jensen, T. and Lindgren, J. 1988: Deep Crustal Structures in the Vicinity of the Siljan Ring.

- Lund, C.-E., Roberts, R.G. and Juhlin, C. 1987:** The reflectivity of the lower crust in southwestern Sweden. *Annales Geophysicae*, 5B, 375-380.
- Luosto, U. and Korhonen, H. 1986:** Crustal structures of the Baltic Shield Based on off-Fennolora Refraction Data. *Tectonophysics*, 128, 183-208.
- Lynch, H.D. and Morgan, P. 1987:** The tensile strength of the lithosphere and the localization of extension. In: M.P. Coward, J.F. Dewey and P.L. Hancock (eds.). *Continental Extensional Tectonics*. Geological Society Special Publication No. 28, 53-65.
- Matthews, D.H. and Cheadle, M.J. 1986:** Deep Reflections from the Caledonides and Variscides west of Britain and comparison with the Himalayas. In: M. Barazangi and L.D. Brown (eds.). *Reflection Seismology: A Global Perspective*. AGU Geodynamics Series, 13, 1-19.
- Meissner, R. 1986:** *The Continental Crust - A Geophysical Approach*. Academic Press, Orlando, 426pp.
- Michelsen, O. 1976:** Kortfattet oversikt over de geologiske forhold i den danske del av Nordsøen. *Danm. geol. unders. Årbog 1975*, 117-132.
- Mykkelstveit, S. 1980:** A Seismic Profile in Southern Norway. *Pure and Applied Geophysics*, vol. 118, Birkhäuser Verlag, Basel, 1310-1325.
- Neugebauer, H.J. 1983:** Mechanical Aspects of Continental Rifting. *Tectonophysics*, 94, 91-108.
- Neumann, E.-R., Pallesen, S. and Andresen, P. 1986:** Mass estimates of cumulates and residues after anatexis in the Oslo Graben. *Journal of Geophysical Research*, vol 91, 11629-11640.
- Noe-Nygaard, A. 1967:** Dredged basalt from Skagerrak. *Medd. Dansk Geol. Foren.* 17, 285-287.
- Nielsen, O.B. and Heilmann-Clausen, C. 1988:** Palaeogene volcanism: the sedimentary records in Denmark. In: A.C. Morton and L.M. Parson (eds.). *Early Tertiary Volcanism and the Opening of the N.E. Atlantic*, Geological Society Special publication No 39, 395-405.
- Olafsson, I. 1988:** Deep crustal structure of the Møre margin from analysis of two ship multichannel seismic data. *Dr. Scient Thesis. University of Bergen, Norway*, 154 pp.
- Pedersen, T., Pettersson, S.E. and Husbye, E.S. 1989:** Skagerrak evolution derived from tectonic subsidence. *Tectonophysics*, this volume.
- Pegrum, R.M. 1984a:** Structural development of the southwestern margin of the Russian-Fennoscandian Platform. *Petroleum Geology of the North European Margin*, Norwegian Petroleum Society, Graham and Trotman, 359-369.
- Pegrum, R.M. 1984b:** The extension of the Tornquist Zone in the Norwegian North Sea. *Norsk Geologisk Tidsskrift*, vol 64, 39-68.
- Poorter, R.P.E. 1981:** Precambrian Palaeomagnetism of Europe and the position of the Balto-Russian Plate relatively to Laurentia. In: A. Kroener (ed.). *Precambrian Plate tectonics*, in the collection *Developments in Precambrian Geology*, Elsevier, Amsterdam, Nederland, 599-622.
- Ramberg, I.B. and Larsen, B.T. 1978:** Tectonomagmatic Evolution. In: J.A. Dons and B.T. Larsen (eds.). *The Oslo Paleorift, A review and Guide to Excursion*. NGU, 337, 55-73.
- Ramberg, I.B. and Spjeldnæs, N. 1978:** The Tectonic History of the Oslo Region. In: I.B. Ramberg and E.R. Neumann (eds.). *Tectonics and Geophysics of Continental Rifts*. Reidel, Dordrecht, Holland, 167-194.
- Rasmussen, L.B. 1974:** Some geological results from the first five Danish exploration wells in the North Sea. A-1, A-2, B-1, C-1 and D-1. *Danm. Geol. Unders. III Række*, 42, 1-46.

Rawson, P.F. and Riley, L.A. 1982: Latest Jurassic - Early Cretaceous Events and the "Late Cimmerian Unconformity" in North Sea Area. Am. Ass. Petrol. Geol. Bull., 66, 2628-2648.

Sellevoll, M.A. and Warrick, R.E. 1971: A Refraction Study of the Crustal Structure in Southern Norway. Seismol. Soc. Amer. Bull. vol 61, No2, 457-471.

Stearn, J.E.F. and Piper, J.D.A. 1984: Palcomagnetism of the Sveconorwegian mobile belt of the Fennoscandian Shield. Precambrian Research, 23, 201-246.

Tryti, J. and Sellevoll, M.A. 1977: Seismic Crustal Study of the Oslo Rift. Pure and Applied Geophysics, vol 115/4, 1061-1085.

Vogel, A. and Lund, C.-E. 1971: Profile section 2-3. In: A. Vogel (ed.). Deep seismic sounding in northern Europe. Swedish Natural Science Research Council, Stockholm, 62-75.

Ziegler, P.A. 1981: Evolution of sedimentary basins in Northwest Europe. In: L.V. Illing and G.D. Hobson (eds.). Petrol. Geol. Cont. Shelf of N.W. Europe, Inst. Petrol. London, 3-39.

Ziegler, P.A. 1982: Geological Atlas of Western and Central Europe. Elsevier, Amsterdam, 130pp and 40 plates.

Åm, K. 1973: Geophysical Indications of Permian and Tertiary Igneous Activity in the Skagerrak. Norges Geol. Unders. 287, 1-25.

Figure Captions

Fig. 1 Location map for the Skagerrak profiles shot by M/V Mobile Search in the winter 1987 (Husebye et al.,1988).

Fig. 2 Structural map of south Scandinavia showing main features. **CF:** Caledonian Front; **CG:** Central Graben; **ESB:** Egersund Sub-Basin; **FBZ:** Fennoscandian Border Zone; **FSE:** Færøy-Shetland Escarpment; **FFZ:** Fjerritslev Fault Zone; **HG:** Horn Graben; **KBFC:** Kristiansund-Bodø Fault Complex; **MB:** Møre Basin; **MTFZ:** Møre-Trøndelag Fault Zone; **MZ:** Mylonite Zone; **OG:** Oslo Graben; **PZ:** Protogine Zone; **RFH:** Ringkøbing-Fyn High; **SF:** Svecofennides; **SNF:** Sveconorwegian Front; **TEF:** Trans European Fault; **VG:** Viking Graben; **WG:** Western Gneiss Region. (Modified after EUGENO-S Working Group, 1988; Bukovics and Ziegler, 1985; Gorbatshev, 1985; Rawson and Riley, 1982). (These abbreviations are frequently used in the text).

Fig. 3 Seismic profiles and seismograph stations in S. Scandinavia used as sources for crustal thickness estimates (profiling details and references in Table IV).

Fig. 4 Linedrawings of OG-2 and OG-12. Depth in km. Intersecting lines are marked.

Fig. 5 Linedrawings of OG-13, OG-5 and OG-7. Depth in km. Intersecting lines are

marked.

Fig. 6 Moho depth below mean sea level - 2 km contour interval.

Fig. 7 Thickness of crystalline crust in km - 2 km contour interval.

Fig. 8 Volcanic activity and thickness of crystalline crust in km -contour interval 4 km.

Arrows indicate directions to early Tertiary magmatic sources within 150 km from ash deposits at Limfjorden (LF), lines are Permian dykes, circles are Permian volcanism, diamonds are Mesozoic volcanism and stars are possible Tertiary volcanism.

Fig. 9 Velocity plots a: Larvik - Lysekil and northern part of EUGENO-S-4; b: Fedje - Grimstad; and c: Fennolora, southern part.

Fig. 10 Epicenters in S. Scandinavia 1951 - 1988, Open squares: Ml:2.4-3.5; filled squares: Ml:3.6-5.5 and crustal thickness in km, contour interval 2 km.

Fig. 11 EQ frequencies vs crustal thickness. Open: Ml:2.4-3.5 ; Hatched: Ml:3.6-5.5.

Fig. 12 EQ frequencies vs crustal thickness, adjusted for unit area of crustal thickness (approx. 25x25km²). Open: Ml:2.4-3.5 ; Hatched: Ml:3.6-5.5.

Fig. 13 Crustal thickness vs tectonic age. Stars = average for period; Triangles = average for subgroup. See Table V for details.

Fig. 14 Bouguer gravity map, contour interval 20 mgal (Balling, 1984).

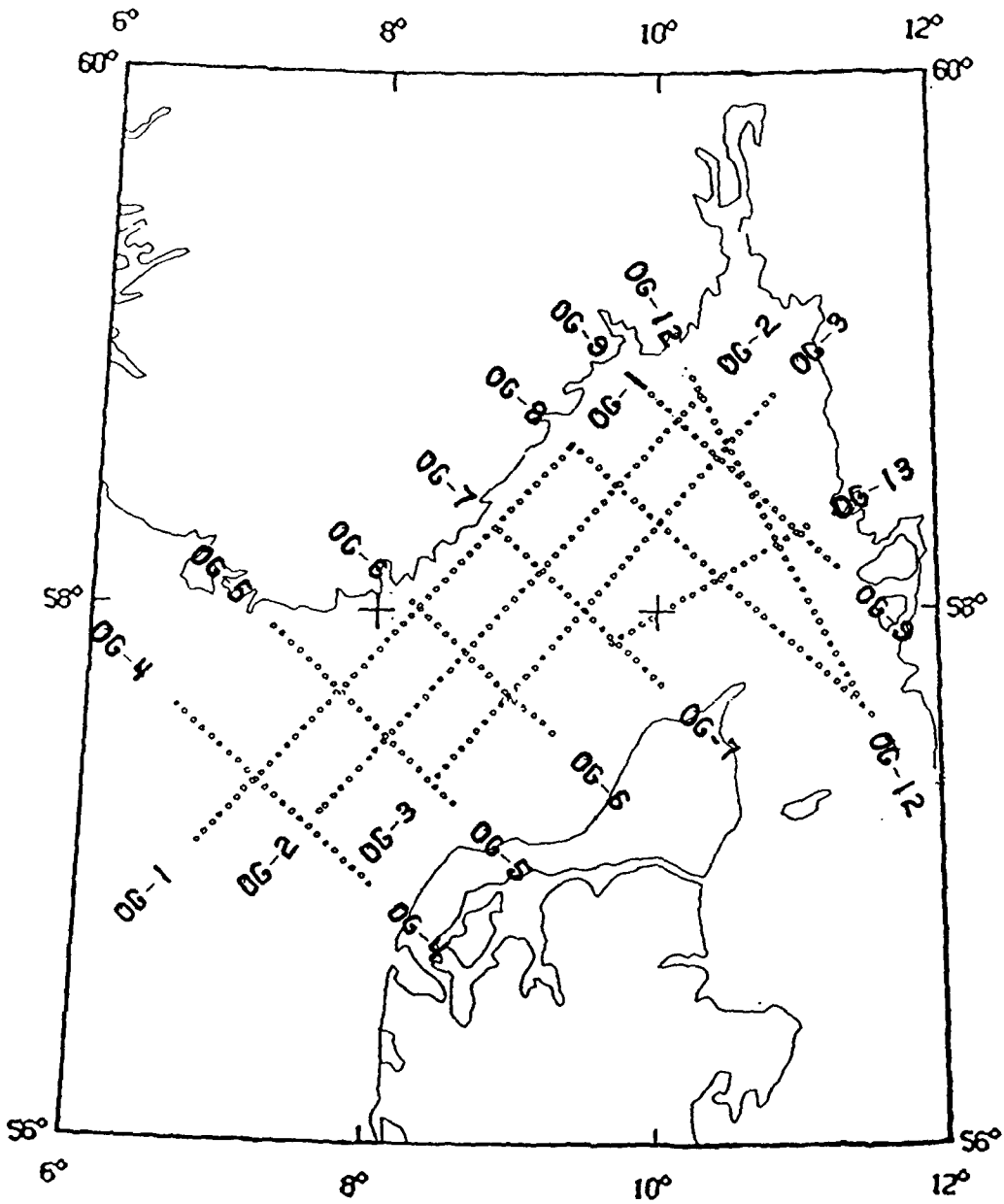


Fig. 1

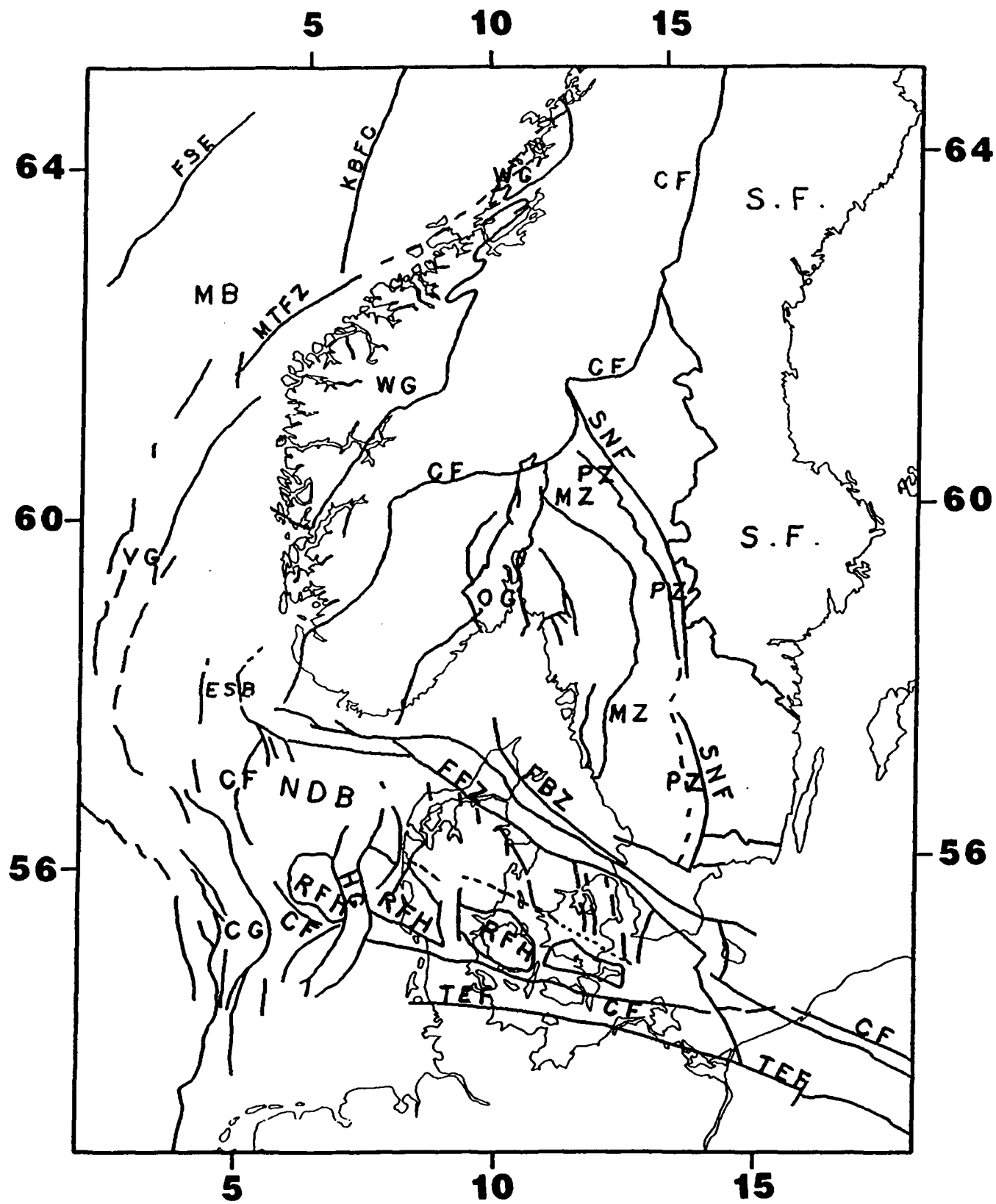


Fig. 2

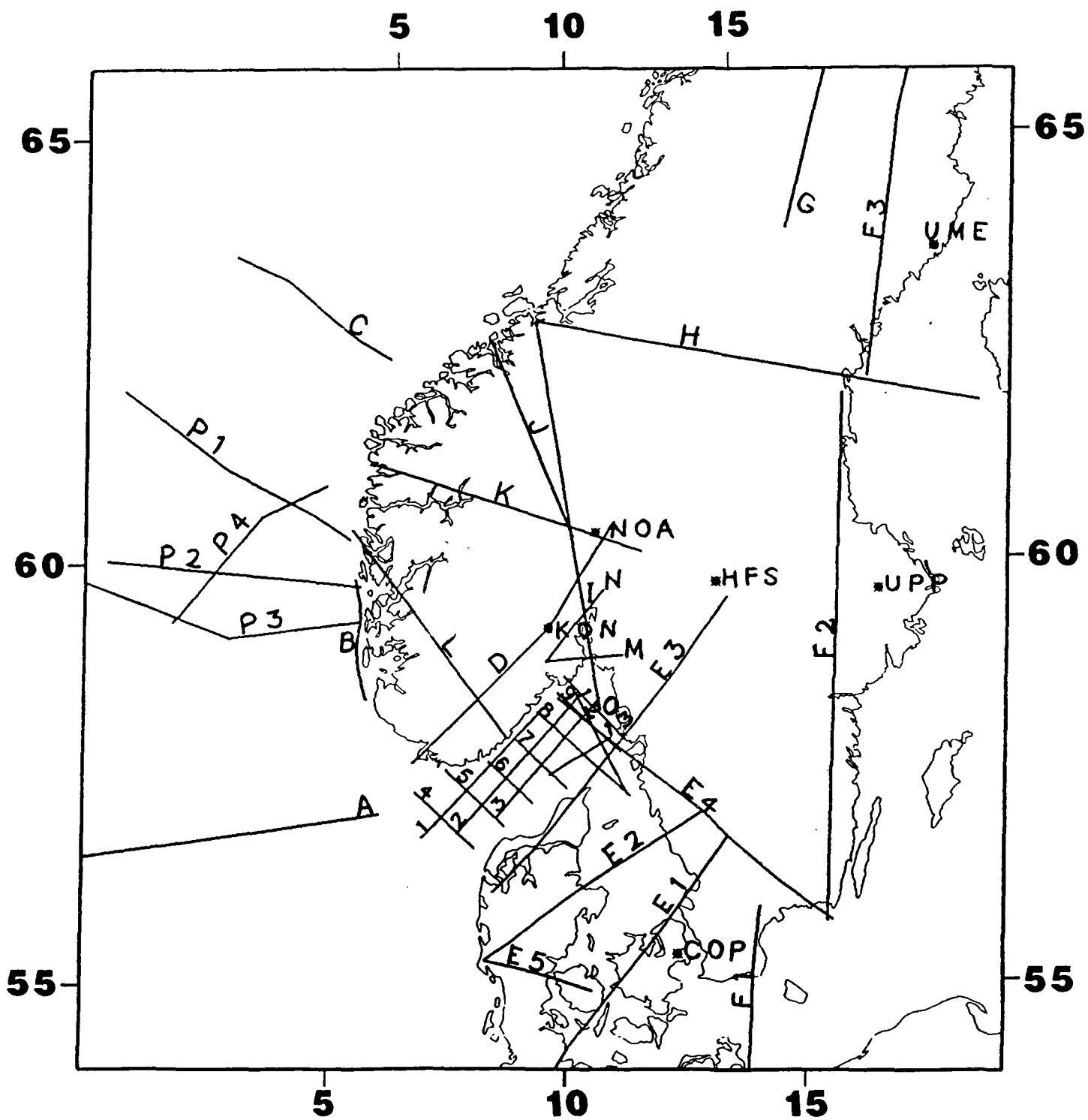


Fig. 3

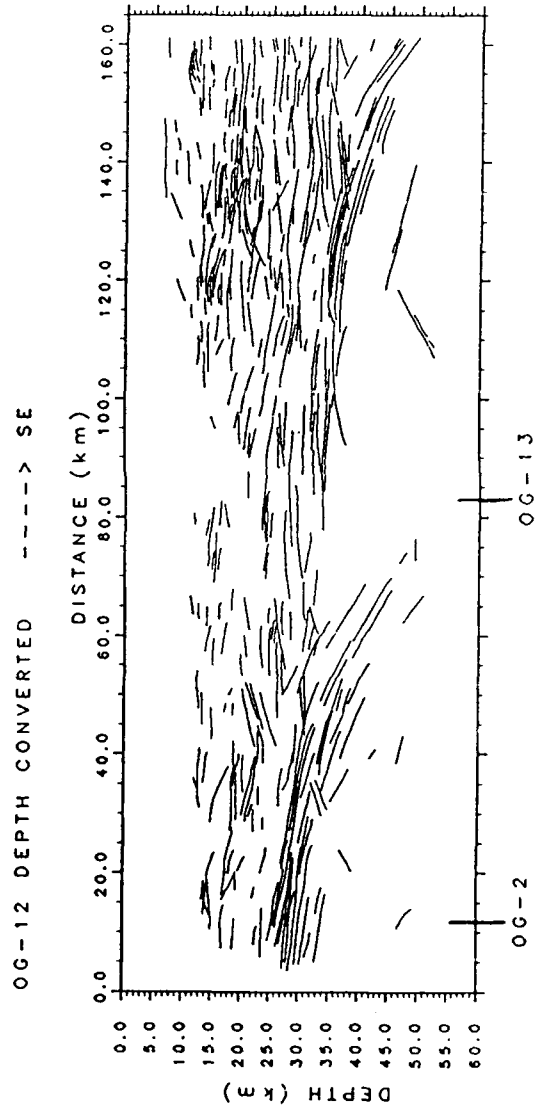
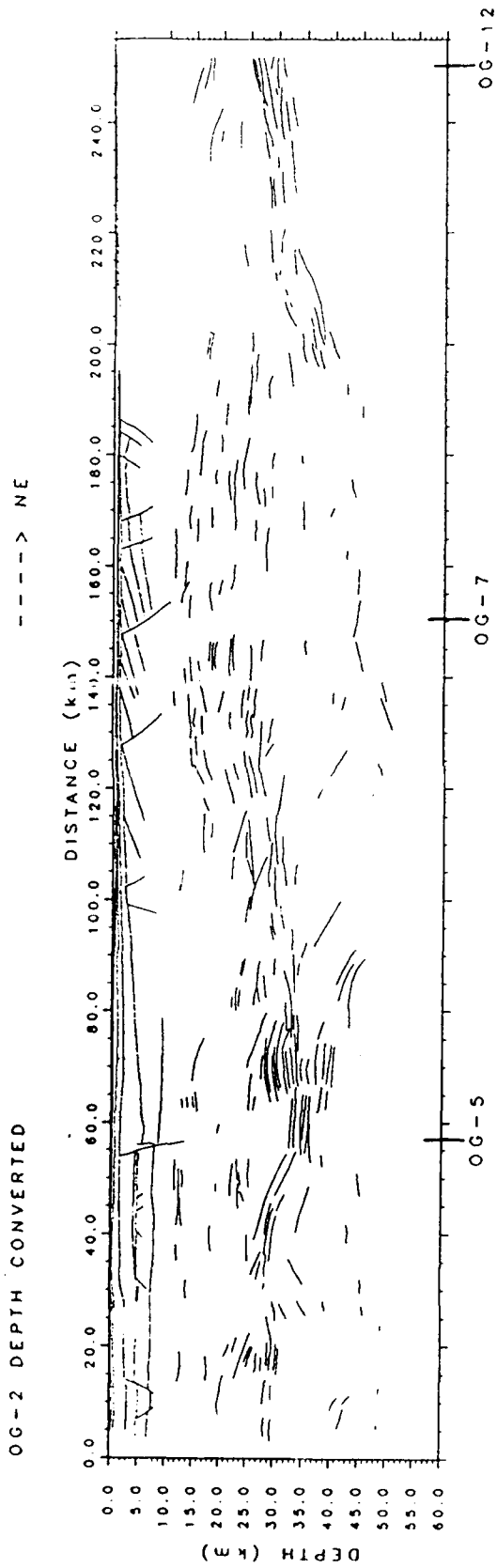


Fig. 4

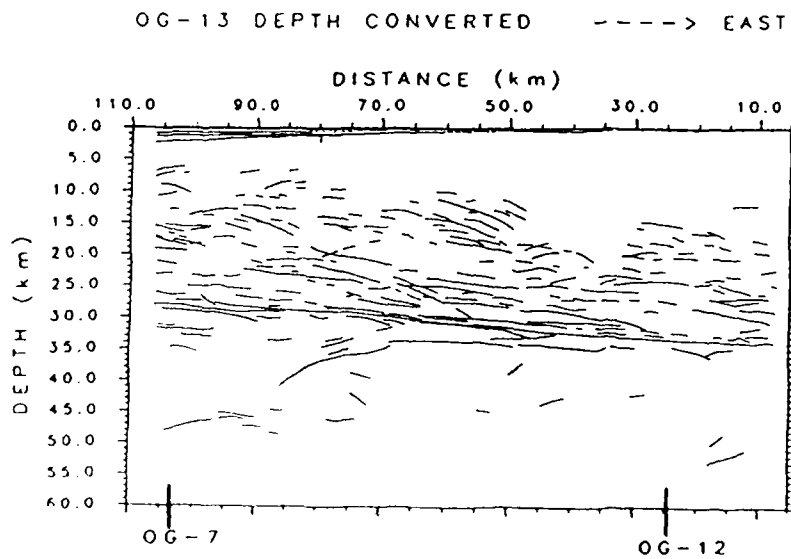
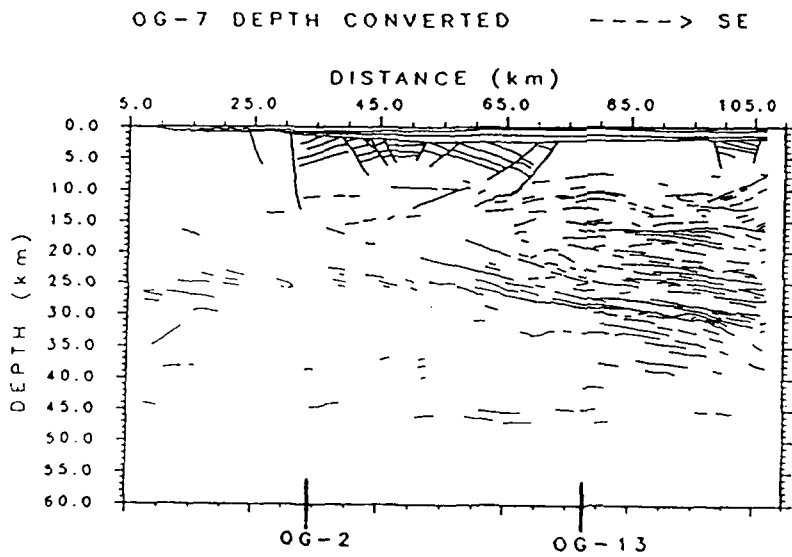
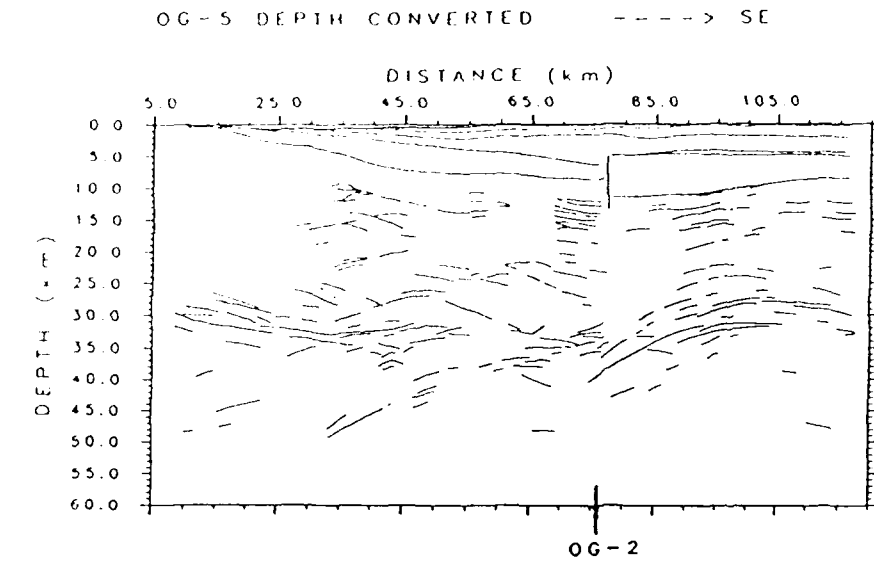


Fig. 5

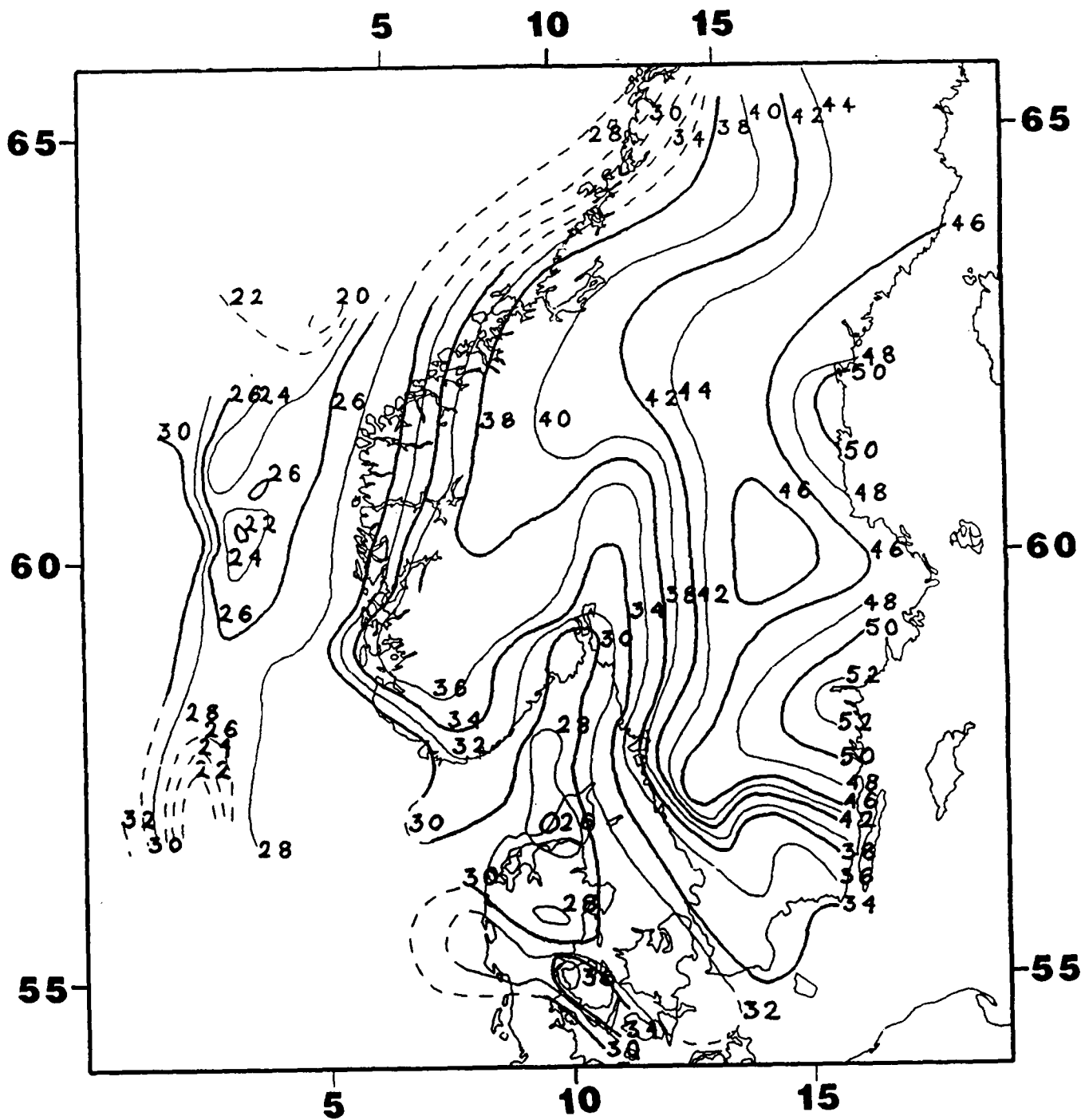


Fig. 6

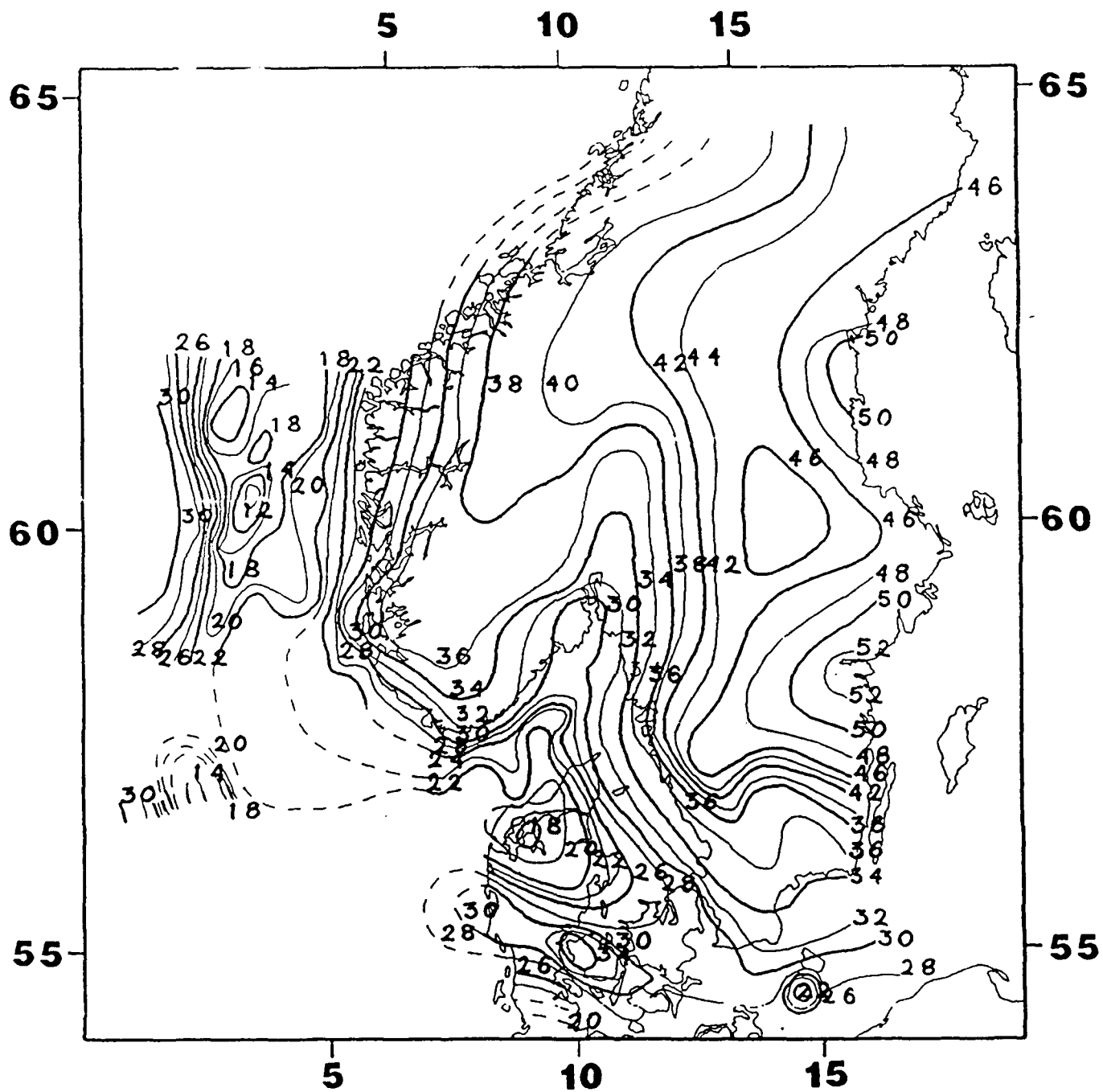


Fig. 7

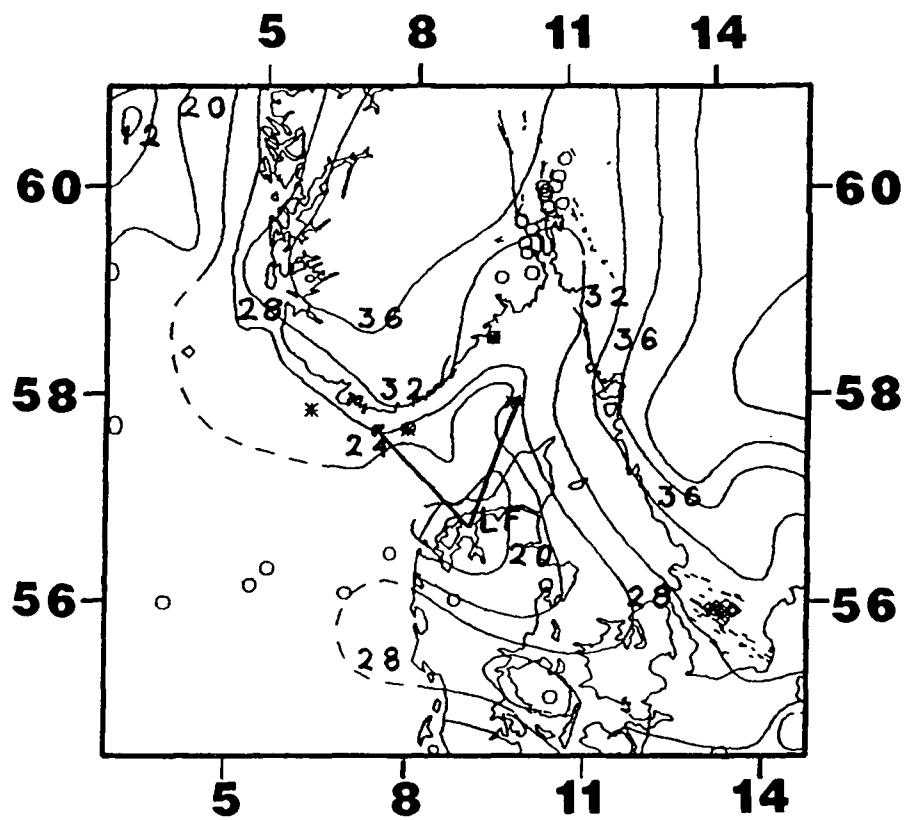
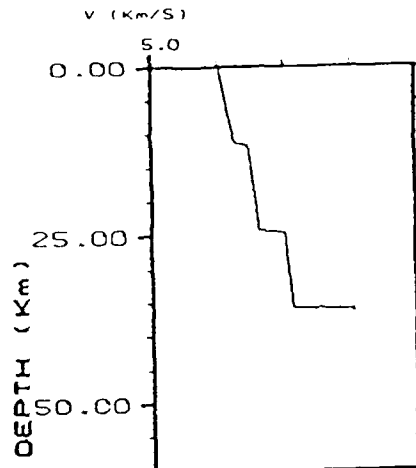
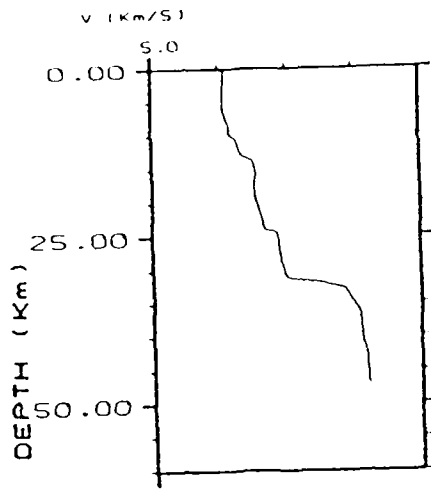


Fig. 8

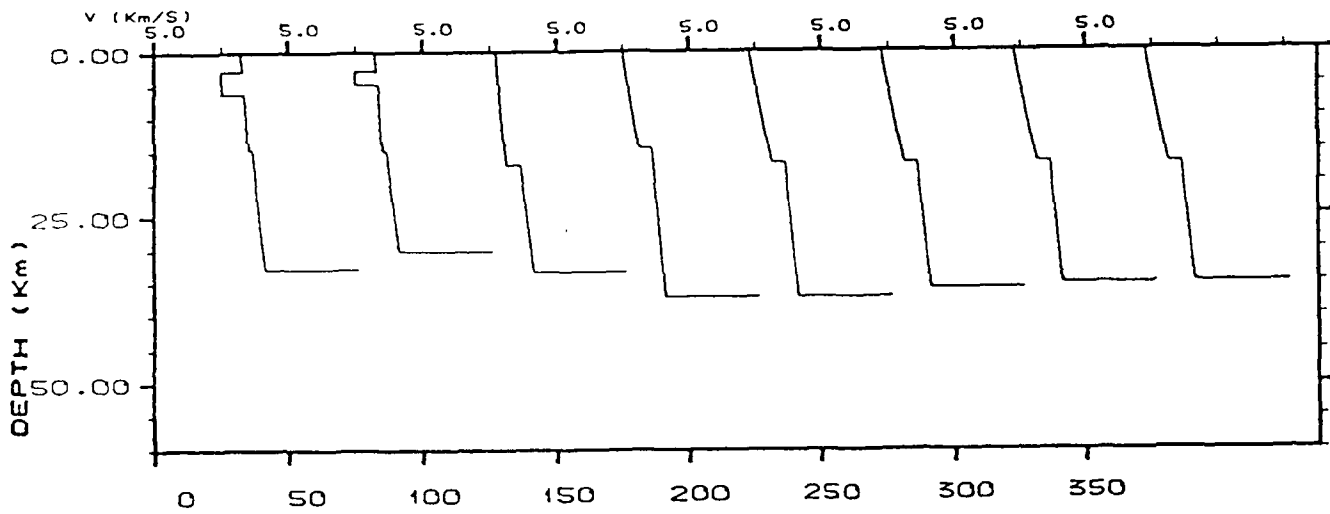
A

LARVIK-LYSEKIL

EUGENO-S-4 NORTH

**B**

FEOJE - GRIMSTAD vel.

**C**

FENNOLORA 1-2 VEL.

OFFSET (Km)

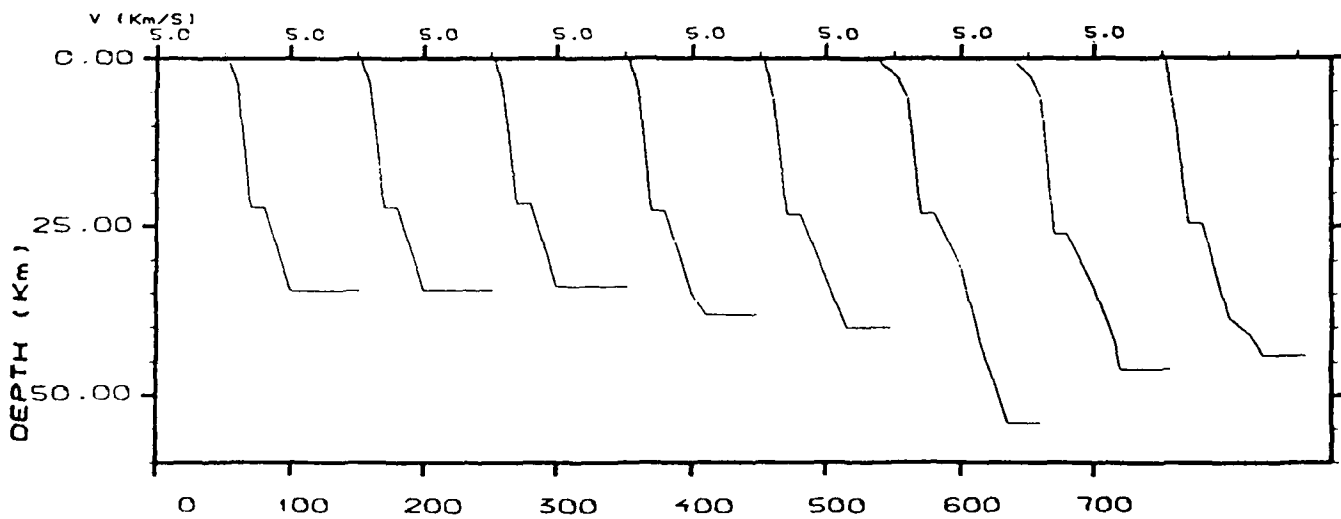


Fig. 9

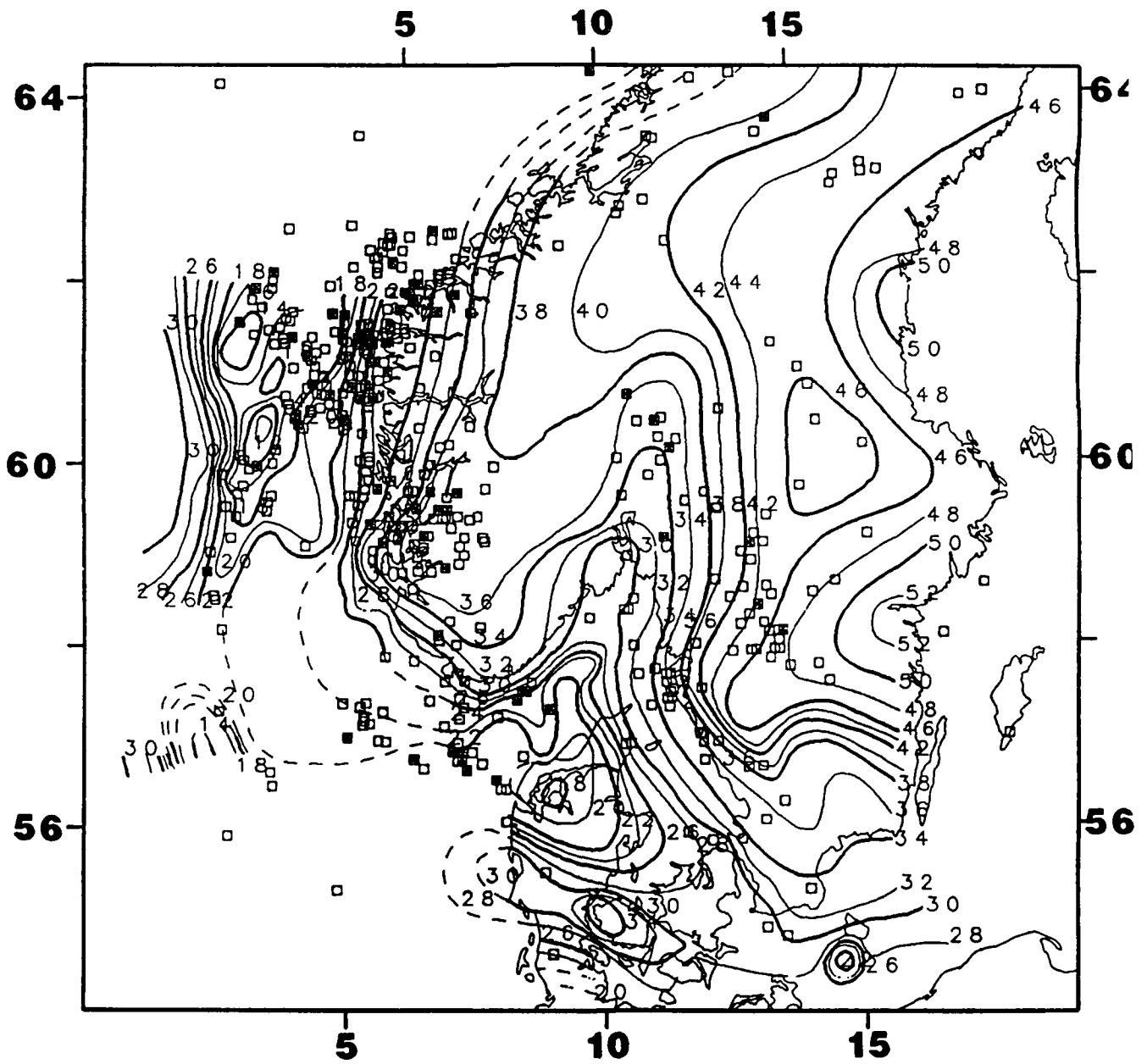


Fig. 10

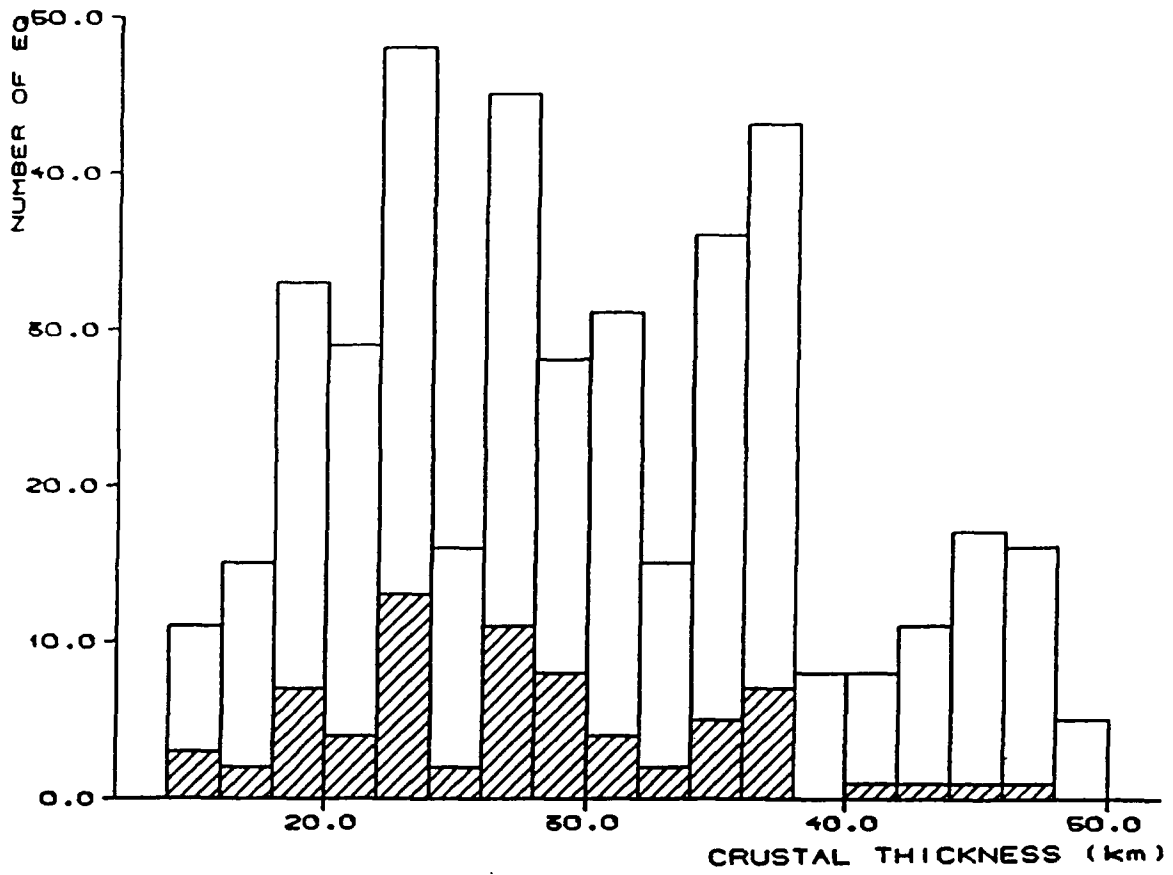


Fig. 11

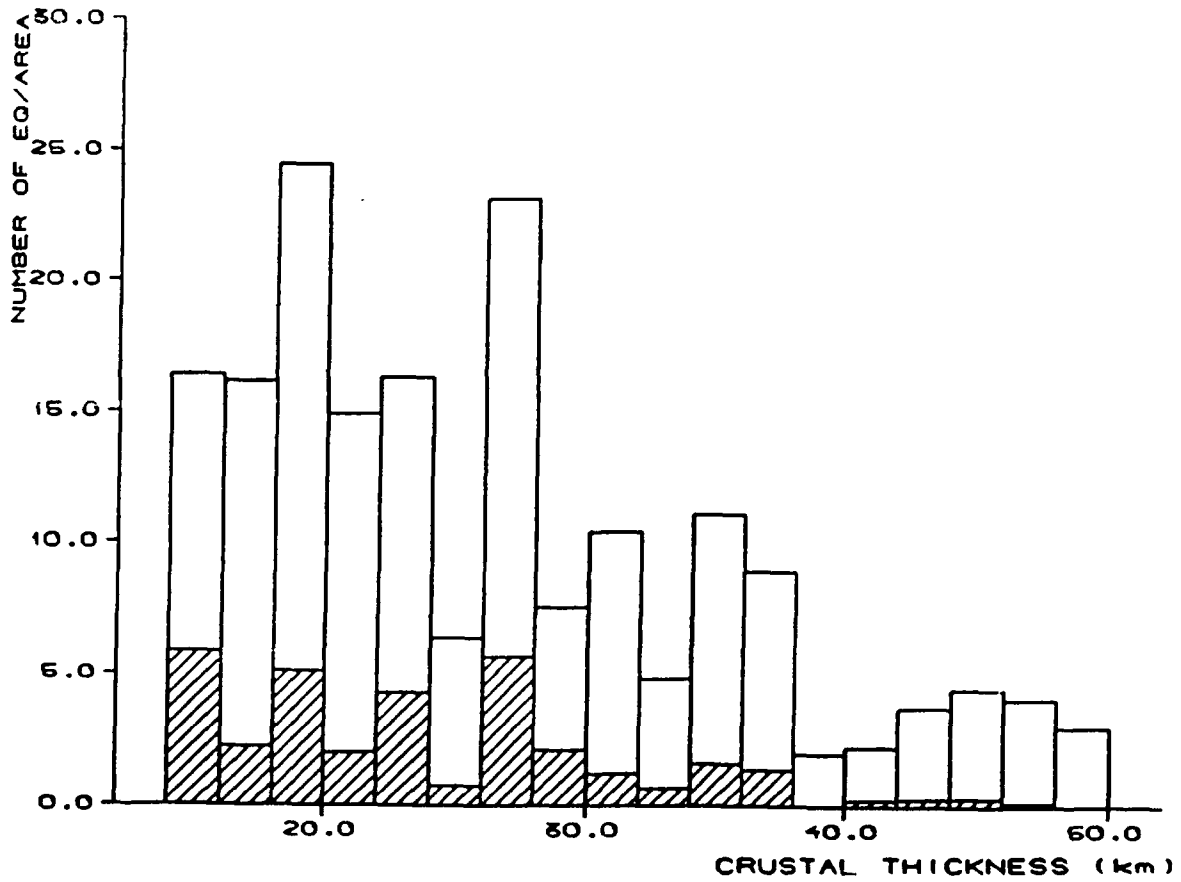


Fig. 12

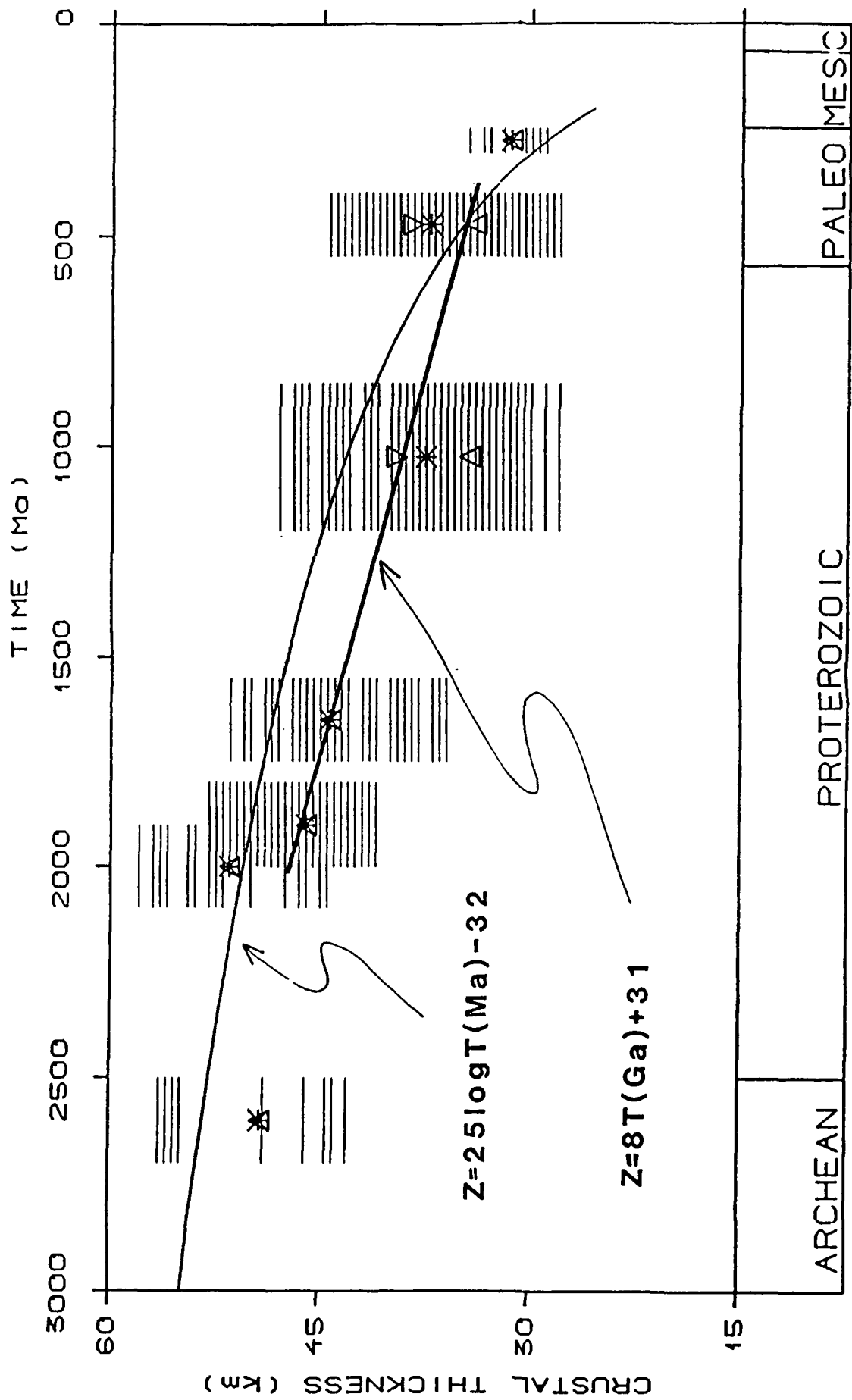


Fig. 13

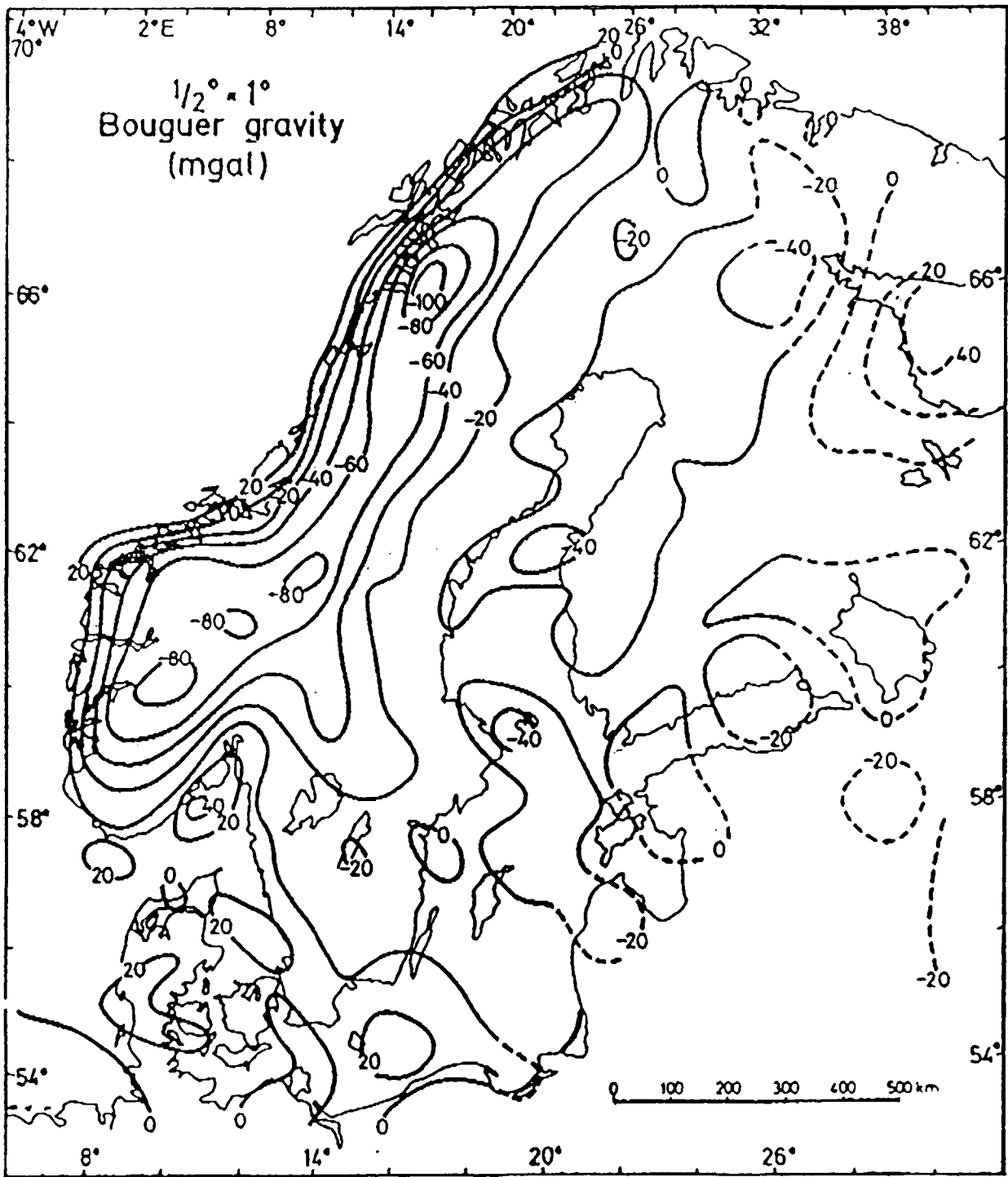


Fig. 14

Tomographic estimates of sub-Moho seismic velocities in Fennoscandia and structural implications

Bannister,S.C., Ruud,B.O., and Husebye,E.S.

Department of Geology, PO Box 1047, Oslo University, Blindern, N-0316 Oslo, Norway.

Abstract

Pn and Sn velocity estimates are derived for sub-Moho structure beneath Fennoscandia using a tomographic conjugate gradient scheme. Observational data stem from local earthquake recordings of crustal phases Pg, Sg (Lg) and subcrustal phases Pn and Sn by the Fennoscandian seismograph network. Unknowns are Pn and Sn velocities along with event hypocentral parameters. Crustal thicknesses are presumed known and are not estimated while velocities are allowed to vary. The most prominent P and S velocity anomalies are found in the northwest (in-land Lofoten) and southwest (Møre) of Norway and, for shear waves, also in central Finland. There is a good correlation between the velocity anomalies in Norway and observed negative Bouguer anomalies, indicating the presence of low-density sub-Moho material in these areas. Geologically the Pn and Sn velocity anomalies appear to be associated with geodynamic processes tied to the opening of the Norwegian-Greenland Sea.

1. Introduction.

Seismology currently offers the most powerful means for mapping the physical properties of the earth, leading towards the understanding of present and past geodynamical processes. Crustal velocity structures have traditionally been mapped only along selected profile lines using refraction and wide-angle reflection data (e.g., in projects such as FENNOLORA, Galson & Mueller, 1986). Although such experiments give detailed information on vertical velocity variations the resolution of lateral heterogeneities is restricted to the profile line. Present knowledge of 3-D velocity structures therefore comes from seismological research where earthquake signals are continuously recorded by seismic stations. The first effort in this field was that of Aki et al. (1977) using arrival times of teleseismic P-waves (distances > 3000 km) at NORSAR, Norway. The method has since been used for mapping larger scale velocity anomalies in Fennoscandia (Husebye and Hovland, 1982) and in southern Scandinavia (Husebye et al., 1986). Dispersion analysis of Rayleigh waves (e.g. Knopoff,1972 and Der and Landisman, 1972) also provides information on lateral velocity variation, resolving the variation of shear wave velocity with depth and hence the lithosphere thickness. Calcagnile (1982) applied this method to the Fennoscandian region and found large thicknesses (>170 km) in Finland and northern Sweden while normal thicknesses (ca.110 km) were found for Denmark and south-western Norway (Dost, 1986).

In this paper we use arrival times of Pn and Sn crustal phases, as reported by Fennoscandian stations, to obtain tomographic estimates of the sub-Moho P and S velocities in the region. Similar studies have been made by Aki and Lee (1976) and Hearn and Clayton (1986a,b) using data from the dense Southern Californian seismic network. Our method differs from that used by Hearn and Clayton, which is a delay time method, in that we allow for variations in crustal thickness and include the earthquake source parameters as unknowns during inversion, thus effectively relocating the events.

We also use a different numerical algorithm, results are presented here for a least square conjugate gradient (CGLS) algorithm (e.g. see Spakman and Nolet, 1988).

2. Model description and inversion technique

The model used in the study consists of a two layered lithosphere which is divided by the Moho discontinuity, the upper layer containing the whole crystalline crust, the critically refracted Pn and Sn rays travelling through the lower layer representing the sub-Moho region. A similar two layer model has earlier proved sufficient for locating local events in Fennoscandia (Ruud et al., 1988). A zero velocity gradient was assumed in the sub-Moho region; in most earth models very low or even negative gradients are given for the earths upper 100 km. In the model of Herrin (1968) for example, which is a smoothed model with no discontinuities or low velocity zones, the P ray-path lies within the upper 100 km for distances of up to ca 1500 km.

Both layers were divided into 36 x 42 rectangular blocks of constant velocity, each block 1°(long) x 0.5°(lat). The large lateral extent of the model requires that the earth sphericity is taken into account. The block subdivision of our model was along lines of constant latitude and longitude; rays which are assumed to follow great circles will appear slightly curved relative to the model grid system. All lateral distance calculations were performed in spherical coordinates.

Variations in crustal thickness were allowed for by varying the thickness of the upper layer blocks (but everywhere with horizontal interface to the block below in the lower layer). Detailed knowledge of the variation of the Moho depth beneath the region has been obtained from deep reflection seismic work; it is known that the Moho depth varies by more than 30 km, from ca. 20 km off the west coast of Norway to some 50 km in central Finland. The a-priori model of crustal thickness used in this study (Fig 1) was based on the works of Kinck et al.(1989, this volume), Luosto (1989, this volume), Planke et al.(1989, this volume), Faleide et al.(1989) and Prodehl and Kaminski (1984).

Ray-tracing was carried out initially using a model with no lateral velocity variation. The rays were traced as straight lines between the hypocenter and station down to the Moho interface, using the angle of incidence calculated from the reference layer velocities (while ignoring the effect of potential slanting Moho). Between the two interface intersection points ray-paths were assumed to be horizontal and completely within the lower layer. Differences in the level of the two intersection points were accounted for by applying a length scaling factor to the segment of the ray in the lower layer. P-wave velocities of 6.32 and 8.18 km/s were used as initial reference velocities for the crust and sub-Moho respectively; initial S velocities were 3.65 and 4.65 km/s. These reference velocities were derived from a least squares regression analysis of our data set described below.

2.1 Inversion

Velocity anomalies and source parameters are highly correlated in travel time tomography involving sources which are not precisely located. Both types of variable should be treated as unknowns during the estimation process (Aki and Lee, 1976; Spencer and Gubbins, 1980). We thus considered the travel time residuals to consist of three parts; (1) that caused by genuine velocity anomalies, (2) mislocation of the events, and (3) errors. The latter group consists of not only reading and timing errors but also errors resulting from deficiencies of the simplified model such as the artificial block structure and the lack of vertical velocity gradient.

The system of equations can then be written, following Spakman and Nolet (1988),

$$Ax = [L, G]x = d + e, \quad x = \begin{bmatrix} s \\ g \end{bmatrix} \quad (1)$$

where s is the vector of slowness anomalies, g the vector of hypocentre parameter corrections (origin time, latitude, longitude and depth), d the vector of time residuals, e the error vector, G the matrix of partial derivatives with respect to hypocentral parameters, and L the matrix of ray segment lengths. Station corrections are accounted for within the upper layer block on which each station is situated. Assuming that the errors are random and approximately follow a gaussian distribution with zero mean we want to obtain a least square estimate of the x vector. Appropriate damping and weighting (according to a-priori information) was applied to the system (1) as detailed by Spakman and Nolet (1988). Such weighting is essential for a meaningful result as the vector x of unknowns in (1) consists of different physical parameters.

In our study the system (1) consists of thousands of unknowns and equations so that solution by generalized matrix inversion is prohibited by computer time and memory considerations. We therefore seek a solution using row-action or projection techniques. These are iterative algorithms with modest memory requirement resulting in stable solutions after relatively few iterations. One such algorithm we have applied is the least square conjugate gradient (CGLS) (Hestenes and Stiefel, 1952). This algorithm produces results very similar to the popular LSQR method (Paige and Saunders, 1982). We also carried out experiments using a SIRT algorithm (e.g. Nolet, 1985). This later algorithm tends to have errors in poorly sampled blocks and was not used for the results presented below.

As tomographic systems are usually under-determined (at least in some parameters) it is critical that the solution is stabilised. Stabilisation in CGLS results from the use of explicit damping together with implicit damping within the actual algorithms, the smaller eigenvalues gradually entering into the solution with increased iterations (Spakman and Nolet, 1988). A mild smoothness constraint was also imposed during the reconstruction process (e.g. Herman et al., 1975) using a nearest neighbour moving average filter every fifth iteration. Such smoothing assists convergence towards a solution involving smoothly varying anomalies.

3. Data and their inversion

Arrival times as reported from seismological stations in Fennoscandia (Fig 2) are routinely collected by the Seismological Institute at the University of Helsinki, Finland, where event association and epicenter location are also carried out. Data from 1981 to the present is available in a computer readable form although the reporting frequency and station coverage were somewhat incomplete prior to 1984. This data base is small compared to the one used by Hearn and Clayton (1986a,b) but resolution is fairly good in the central part of the region where cross-sampling is best, as demonstrated below; there is a reasonable distribution of events across the region, with a high density in the west Norway and Finland areas as well as in the Norwegian Sea.

We used P_n and S_n arrival times reported from seismic stations (Fig 2) in the Fennoscandia region between January 1984 and May 1988. The network at hand is too

coarse for incorporating Pg and Sg(Lg) phase observations as these phases are seldom reported reliably beyond epicenter distances of 2-300 km due to Pn and Sn interference. The arrivals were extracted by subjectively 'windowing' on a travel-time distance plot (e.g. Fig 3) using an absolute residual time threshold of 3s; the rejected arrivals scattered outside of these windows are likely to be associated with events that are poorly located or involve data input errors. More than 1800 Pn and 1500 Sn arrivals were extracted between distances from 350 to 1500 kms. Fig 4 shows the spatial coverage of the Pn and Sn raypaths respectively. It is seen that there is a high density of raypaths in the center of Fennoscandia, along the west coast of Norway and between north-west Norway (offshore) and the Finland seismograph network.

All events reported for the time period were relocated by us both before the inversion, using the updated crustal model which incorporates the variation in depth of the Moho across the region (Fig 1), and after the inversion, incorporating the lateral variations of velocity detailed below. The epicenters of the events before the first relocation (i.e. as reported in the Finland data base) are shown in Fig 5. together with the final locations following the completion of the inversion procedure. Maximum epicenter shifts from the initial 'Finland' event locations to the final inversion locations were of the order of 1° for events at the periphery of the model, but of the order of 10 km for events in its central parts. Most of this epicentral shift occurred in the first pre-inversion relocation, the shift in the epicenters following this first relocation (i.e. to the final epicenters determined by the end of the inversion procedure) was much less - of the order of 5 km in the central areas, approximately half of the above. Most of the epicentral shift can be attributed to our improvement of the data set together with a small difference in the reference Moho velocity. Event depths generally shallowed slightly, remaining within the upper crust with few exceptions, all events above the Moho. Only arrivals from events within the region were included in the inversion and events with less than 5 phases were disregarded. Station elevation corrections were applied to both Pn and Sn arrivals.

Inversion of the data was accomplished through application of the CGLS algorithm, estimating ca.1600 hypocenter corrections and ca.1300 velocity parameters. The RMS of the travel-time residuals was reduced from 1.5 seconds to 0.6s (P-velocities) and 1.5s to 0.74s (S-velocities) after 39 iterations. A mild nearest-neighbour moving average was applied to the resulting velocity images to emphasize the longer wavelength features (Herman et al., 1975). This filter had a small, if negligible, effect on the convergence. A more important parameter was the relative scaling between hypocentral and slowness corrections, discussed further below.

3.1 Resolution and error analysis

In the following section the major anomalies found in the tomographic inversion are presented and discussed. First, however, we must examine the resolution associated with the data set. Use of the ray-traction techniques prohibits us from calculating formal resolution and standard errors for the estimated parameters. As a substitute we inverted several synthetic data sets constructed using the rays from the actual data set and the travel times calculated from artificial slowness anomalies.

The synthetic models are shown in Fig 6, along with the P-velocity images derived after application of the CGLS algorithm. The first synthetic model (Fig 6a) involved patterns of low (7.9 km/s) and high (8.5 km/s) bodies in a sub-Moho with a background velocity of 8.2 km/s. No anomalies were initially placed within the modelled crustal layer, which was assigned an initial velocity of 6.32 km/s. Velocities of all blocks in both the sub-Moho and crustal layers were included as unknowns in the tomographic

reconstruction (Fig 6b), together with hypocentral correction parameters, which were initially set to zero. The second model (Fig 6c and 6d) involved east-west oriented velocity anomalies (7.9 km/s and 8.5 km/s) within the sub-Moho.

Inversion of the data was accomplished through application of the CGLS algorithm. The RMS of the travel-time residuals for the first data set was reduced from 0.63 s. to 0.12 s. after 39 iterations. The artificial anomalies in the center of the model (Fig 6a) are well resolved, both spatially and in amplitude (Fig 6b). These regions correspond to central Fennoscandia, that is Bothnian Bay, southwest Finland, the east and center of Sweden, and central Norway. We can see some smearing of the anomalies in the NW-SE direction in the northern part of the model, an effect that is best seen in the first synthetic model (Fig 6b) but that is also reflected in Fig 6d where broadening of the northern row anomalies can be seen. This effect likely results from the biased (NW-SE) direction of the raypaths in this part of Fennoscandia, involving waves from events off-coast NW Norway recorded at seismograph stations in central Finland. In addition to this effect we can see broadening of the row anomalies to the west of Norway (Fig 6d); the resolution of the images are highly dependent on the cross-sampling of the ray-paths (Fig 4). The amplitudes of the reconstructed anomalies are, on average, ca 60 % of the synthetic anomalies. In this respect we note the dependence on the relative scaling of the hypocenter parameters with respect to the velocity perturbations. The unknown event corrections are usually not well constrained, and can easily absorb part of the delay time which may otherwise be explained by velocity heterogeneities. In a joint inversion as carried out here this has a damping effect on the estimation of the sub-Moho velocity heterogeneities - the anomalies tend to be reconstructed with less amplitude, and thus represent minimum estimates. This effect is most dominant in regions which have poor ray coverage, biasing the event parameters but down-weighting the velocity perturbation. To a lesser extent this same trade-off also occurs between the estimated velocities of blocks within the crustal layer and the sub-Moho, again resulting in down-weighted estimates for the sub-Moho velocity perturbations. The reconstruction would act similarly with real data involving data errors; in this regard there is a subtle balance between reconstructing the full magnitude of the cell slowness anomalies and the degree of influence of the data errors on the velocity estimates. This subjective scaling is determined on the basis of the amplitude behaviour of the components of the solution - the hypocentral corrections and velocity estimates.

We note that this synthetic modelling will not separate the artifacts in the solution that may result from mis-representation of the earth structure or our parameterisation. The possible effect of such errors on the velocity estimates are discussed further below.

4. Results

Results of the tomographic inversion of the data set are shown in figures 7 and 8 for the P and S-arrival data sets respectively. The general trend seen in the P velocity reconstruction is towards high velocities in the oldest and thickest part of the Baltic shield and low velocities in Norway and the offshore areas. It should be noted that areas which are not sampled (e.g. Barents Sea) will retain the reference values for the P and S velocities. The most prominent features in the P-velocity image are the low velocity anomalies beneath western (60-62°) and central (62-63°) Norway, the Lofoten area in the NW (67-69°N) of Norway and the weaker anomaly beneath south-central Finland (see Fig 7 for details). Offshore, the negative anomaly trending WNW from S.Sweden, across Jutland and towards SW Norway coincides with the Fennoscandian border zone. Weak high velocity anomalies are found beneath eastern Sweden, Bothnian Bay and central NE Finland. From the synthetics in Fig.6 the above anomalous areas are well sampled, that is

the ray path coverage is good with respect to path orientation and density and thus the resolution should be good. However the results from the synthetic modelling indicate that the anomalies in the Lofoten area are likely to be smeared slightly in the NW-SE direction while those anomalies far off-shore western and southern Norway are of marginal significance.

Similar features are also seen in the S-velocity image, together with an additional anomaly at 65°N (SE Sweden). Both the W.Norway anomalies are quite strong and again are spatially well resolved. The S velocity anomaly beneath south-west Finland is strong, involving a 2-3% contrast with the surrounding lithosphere, slightly greater than the P-wave anomaly observed in that area.

Crustal P and S velocities estimated in the inversion deviated from the background reference velocity only in the blocks directly beneath seismograph stations and events. Estimated velocities varied from 6.17 km/s to 6.45 km/s across the region, quite a respectable deviation from the initial 6.32 km/s but well in line with the range of (average) crustal velocities that might be expected. These estimates however are not further interpreted here as the estimates act to some degree as buffers for data errors, as noted above in the synthetic modelling.

There may well be artifacts resulting from mis-representation of the earth structure or our parameterisation that were not illuminated by the synthetic modelling. For example if the crustal model used in this study is grossly inaccurate then event locations and the calculation of the reference ray paths will both be affected to some extent although the resulting bias in the images is difficult to detect and separate. Such errors in the crustal model are not considered likely however as the crustal model in Fig 1 is quite heavily sampled apart from the periphery of the area, and is based on many intersecting profile lines. It is recognised however that there is some varying interpretations for the crustal model in south-west Finland and for the crustal transition along the western coastline of Norway. To test the effect of possible errors we carried out several inversions involving crustal models of varying thickness (+/- 2 to 5 km), and found only slight changes in the main features of the images discussed above. For example when the model crustal thickness in the area bounded by longitudes 10 and 13 and latitude 63 and 66 is increased by 5 km, which is an extreme change in the defined model, the change in the P velocity estimate for the sub-Moho in that region is only ca.0.04 km/s. The possible variation in the sub-Moho velocity depends on the sampling of the particular crustal block in question, for example crustal blocks directly above the western coastline of Norway (the region delimited in the above example) are only very lightly sampled. The method is expected to be most sensitive to errors in the crustal thickness beneath stations although these errors may also be absorbed, to a degree, by the crustal velocity estimate for the particular block. Errors in the thickness beneath epicenters on the other hand will mainly affect the estimated hypocentral depth.

Other errors may result from, for example, the parameterisation of our model involving a zero gradient within the upper mantle, and the subsequent modelling of the data as seismic energy propagating as head waves, rather than diving waves within the upper mantle. The evidence for any positive velocity gradient in the mantle beneath Fennoscandia is limited and there is generally a lack of accurate information on the variation in P and S amplitude vs distance. Moreover the P and S arrival time plots (Fig 3) are quite linear for distances up to around 1200 km, suggesting no large gradient in the mantle lid. If, however, a large positive velocity gradient did exist beneath the region then the errors induced in our results will vary depending on the distance of propagation under consideration, being higher for larger distances, and presumably leading to high

estimates for the velocities. It is difficult to quantify the overall effect on the velocity images from such an error although we do not believe that it would be great - 75% of the arrivals involve epicentral distances of less than 1000 km. Longer epicentral distances are usually associated with the events offshore NW Norway and corresponding raypaths show no obvious correlation with high velocity anomalies.

5. Geological and Geophysical Framework of Fennoscandia

The anomalous Pn and Sn velocity distributions appear, as noted above, to be correlated with dominant geophysical features in the region. Before discussing this in more detail we first outline the geological and geophysical setting of Fennoscandia.

The Baltic Shield, comprising Norway, Sweden, Finland, the Kola peninsula and USSR Karelia, was mainly formed or accreted during four orogenies between 3100 to 1500 Ma. The shield is roughly zoned, in the sense that the oldest crust is found in NE Finland and the Kola peninsula and the youngest in south and eastern Norway (Fig 9). Most of the Baltic shield was formed during the Lopian (2900- 2600 Ma), the Svecofennian (2000-1750 Ma) and the Gothian (1750- 1500 Ma) orogenies although the oldest crust stems from the Saamian orogeny (3100- 2900 Ma). The Protogine zone (PZ in Fig 9) in south-central Sweden was formed by episodic faulting accompanied by magmatic intrusions. Today it constitutes a geologically sharp boundary between highly metamorphic SW Scandinavia and the well preserved Svecofennian terrains to the east. The later Sveconorwegian orogeny resulted in thorough reworking of the crust as far east as the Protogine zone (Gaal and Gorbatshev, 1987). The Caledonian orogeny (600-400 Ma) involved closing of the Iapetus ocean (Late Ordovician) and subsequent Himalaya-type collision between Laurentia-Greenland and Fennosarmatia-Baltica. Large areas of the precambrian crust of W.Scandinavia become concealed beneath basement-involving nappes (e.g. Gee and Sturt, 1985 and Hossack and Cooper, 1986), with progressive extensive metamorphism in a NW direction. The extent of crustal deformation is not known in detail.

More recent deformational processes have involved extensional deformation of the continental margin offshore Norway and substantial thinning of the crust and lithosphere. The most recent deformation process of interest to our study is the opening of the Norwegian-Greenland Sea which commenced ca. 57.5 Ma ago (Talwani and Eldholm, 1977), and the transition from continental to oceanic crust tied to the Faeroe-Shetland and Vøring Plateau escarpments offshore (Fig.9). As the extension of continental lithosphere is accompanied by influx of hot magmatic material, anomalous heat flow is intuitively expected in certain parts off-shore W.Norway and possibly other parts of the continental margin. This in turn would correspondingly affect the Pn and, in particular, Sn velocity distributions. Key references on the geological evolution and structural mapping of these areas are Ziegler (1988), Planke et al.(1989) and Faleide et al.(1989); see also Fig 2 and Fig 9.

5.1 Geophysical investigations - crust/lithosphere structural mapping

The principal geophysical means for crust/lithosphere mapping are seismic refraction, wide-angle and reflection profiling. The main results within the region are incorporated in the crustal thickness model for Fennoscandia (Fig 1) and have, amongst others, been summarized by Kinck et al.(1989) and Luosto (1989). Tomographic mapping of the upper mantle has been performed by Husebye et al.(1986) using teleseismic P-wave residuals, although only long wave length structural anomalies could be mapped using this data. For an overview of other geophysical investigations see Husebye (1982) and others in this

volume. The gravity surveys are of most interest as the long wavelength anomalies may reflect sub-Moho heterogeneities. The Bouguer gravity map for Fennoscandia is displayed in Fig 10. One outstanding feature is the pronounced gravity low along the mountain range of Norway which broadens over the south central and Lofoten areas. Theilen and Meissner (1979) and Meissner (1979) noted the lack of mountain roots beneath the mountain range. They suggested that at least part of the implied mass deficit must be attributed to mantle sources while smaller wavelength features in the gravity field reflect the more superficial Caledonian nappe lithology (Wolff, 1983 and Haworth et al., 1988). Finally, areas exhibiting high heat flow are often characterized by relatively low seismic velocities, as demonstrated by Hovland et al (1981) for the Central Europe lithosphere. Unfortunately few precise heat flow measurements are available for Fennoscandia, and they are particularly lacking in the younger and, for this study, critical 'coastal' areas of Norway where heat imprints from the opening of the Norwegian- Greenland Sea might exist.

6. Discussion

The dominant shield structures in central parts of Fennoscandia exhibit only modest P and shear velocity anomalies (Fig 7 and 8). This is not unexpected as shield areas in general are seismologically homogeneous. The notable exceptions, as noted above, are the S and P velocity anomalies beneath south central Finland and the NE coast of Sweden which coincide neatly with the Svecofennides (Fig 9). The shear velocity anomaly is dominant, possibly indicating lateral variations in Poissons ratio.

The other dominant velocity anomalies are those found in Norway which coincide with pronounced negative gravity anomalies of long wavelength (Fig 9). As noted above the implied mass deficit cannot be fully explained by crustal structure, the presence of low-density upper mantle is required to explain the deficit. The velocity anomaly determined for the Lofoten area, ca. 3%, corresponds approximately to a density anomaly of 0.1- 0.2 Mg/m³ (using the relation of Birch, 1961). A body 10 x 200 x 200 km³ and with a relative density contrast of 0.1Mg/m³ would give rise to a Bouguer anomaly of 30-40 mgal or roughly half of the observed anomaly. It is puzzling however that critical sections of the prolonged negative Bouguer anomaly beneath the Caledonides do not have an obvious counterpart in the estimated Pn and Sn anomalies, although higher correlation is observed for the shear wave anomalies. To summarise the Norwegian mountain range correlates poorly with crustal thickness and does not appear to have a pronounced root-structure as observed elsewhere in similar areas. The negative P and S velocity anomalies observed in this study imply mass deficits at sub-Moho levels beneath two areas of Norway. In this context, Meissner (1979) and Theilen and Meissner (1979) have suggested that the primary mountain roots may have been 'scraped off' by a creep process related to the opening of the Norwegian-Greenland Sea. The implied mechanism is the intrusion of low viscosity, low density asthenosphere material beneath the Caledonides. Such a process is likely to be most dominant in areas close to the continental/ oceanic transition, i.e., close to where the velocity anomalies are observed. It is also notable that these areas (Møre and Lofoten) are also the landward extension of the major fracture zones in the Norwegian sea, the Jan Mayen Fracture Zone and Senja Fracture Zone (Fig.9). Realistically however, although the data at hand indicates the existence of sub-Moho structural heterogeneities, the data are not sufficient to resolve the type and extent of geodynamic processes deforming the lithosphere in areas of W.Norway. A far more extensive observational data base, including crustal seismic structural details and heatflow data, is required for a serious attempt at modelling the collision and opening processes.

The geometry of station and event distribution, as noted above, means that velocity estimates within peripheral blocks are less well resolved. We still consider however that the anomalies coinciding with the Fennoscandian border zone, and continuing further westward, reflect sub-Moho structural heterogeneities in this area. The anomalies could in fact continue southward without being resolved by the data (see Fig 6d). The argument here is that the crust in the area is very thin (e.g. see Kinck et al, 1989) and that the associated relative recent deformation processes have originated in the deeper part of the lithosphere.

7. Conclusions

Pn and Sn velocity estimates are derived for the sub-Moho beneath Fennoscandia. Both P-wave and shear wave velocity anomalies are found in the northwest and southwest of Norway and in central Finland. There is a close correlation between the anomalies observed in Norway and observed negative Bouguer gravity anomalies, indicating the presence of spatially restricted regions in the uppermost mantle involving low (P and S) velocity and corresponding low density. Geologically the anomalies are likely to be associated with geodynamic processes tied to the opening of the Norwegian-Greenland Sea.

Acknowledgements

This research was supported by the Royal Norwegian Council for Scientific and Industrial Research (S.C.B.), the Defence Advanced Research Projects Agency under AFORS Grant-89-0259 (B.O.R), VISTA (V6222) and NAVFCD (E.S.H).

References

- Aki,K. and Lee,W.H.K.,1976. Determination of three-dimensional velocity anomalies under a seismic array using first P arrival times from local earthquakes (part 1). *J.geophys.Res.*,81, 4381-4399.
- Aki,K., Christoffersson,A. and Husebye,E.S., 1977. Determination of the three-dimensional seismic structure of the lithosphere. *J.Geophys.Res.*,82: 277-296.
- Balling,N., 1984. Gravity and isostasy in the Baltic Shield. In: Galson,D.A. and Mueller,S. (eds), *First EGT Workshop : The Northern Segment*, 53-68. European Science Foundation, Strasbourg, 169 pp.
- Berthelsen,A., 1987. A tectonic model for the crustal evolution of the Baltic shield. In : J.-P Schaer and J.R.Rodgers (eds.), *The Anatomy of Mountain Ranges*. Princeton University Press. Princeton, New Jersey, 31-57.
- Birch,F., 1961. The velocity of compressional waves in rocks to 10 kilobars, part 2. *J.geophys.Res.*, 66, 2199-2224.
- Calcagnile,G. 1982. The lithosphere-asthenosphere system in Fennoscandia. In: E.S.Husebye (ed), *The Structure of the Lithosphere-Asthenosphere in Europe and the North Atlantic*. *Tectonophysics*, 90: 19-35.
- Der,Z.A. and Landisman,M.1972. Theory of errors, resolution and separation of unknown variables in inverse problems, with application to the mantle and the crust in southern Africa and Scandinavia. *Geophys.J.Roy.astron.Soc.*,27,137-178.
- Dost,B., 1986. Preliminary result from higher-mode surface wave measurements in western Europe using NARS array. In: D.A.Galson and St.Mueller (eds.): *The European Geotraverse, Part 2*. *Tectonophysics*, 126, 1-30.
- Faleide,J.I., Gudlaugsson,S.T., Eldholm,O., Myhre,A.M. and Jackson,H.R., 1989. Deep sea transects across the western Barents Sea continental margin. *Tectonophysics*, this issue.
- Gaal, G. and Gorbatshev,R. 1987. An outline of the Precambrian evolution of the Baltic shield. *Precambrian Research*, 35, 15-52.
- Galson,D.A. & Mueller,St., 1986. An introduction to the European Geotraverse project : First results and present plans. *Tectonophysics*, 126, 1-30.
- Gee,D.B. and Sturt,B.A. (eds). 1985. *The Caledonian Orogen - Scandinavia and related areas*. Wiley, New York, 197-212.
- Haworth,R.T., Hipkin,R., Jacobi,R.D., Kane,M., Lefort,J.P., Max,M.D., Miller,H.G., & F.Wolff. 1988. Geophysical framework and the Appalachian-Caledonian connection. In: Harris,A.L. & Fettes,D.J. (eds), *The Caledonian-Appalachian Orogen*, Geological Society Special Publication No. 38, pp 3-20.
- Hearn,T.M. and Clayton,R.W., 1986a. Lateral velocity variations in southern California. 1. Results for the upper crust from Pg waves. *Bull.Seism.Soc.Am.*,76, 495-509.

- Hearn, T.M. and Clayton, R.W., 1986b. Lateral velocity variations in southern California. 2. Results for the lower crust from Pn waves. *Bull. Seism. Soc. Am.*, 76, 511-520.
- Herman, G.T., Lakshminarayan, A.V. and Rowland, S.W., 1975. The reconstruction of objects from shadowgraphs with high contrast. *Pattern Rec.*, 7: 157-165.
- Herrin, E., 1968. Seismological tables for P phases, *Bull. Seism. Soc. Am.*, 58, 1193-1241.
- Hestenes, M.R. and Stiefel, E., 1952. Methods of conjugate gradients for solving linear systems. *J. Res. N.B.S.*, 49, 409-436.
- Hossack, J.R. and Cooper, M.A., 1986. Collision tectonics in the Scandinavian Caledonides. In: Coward, M.P., Dewey, J.F. & Hancock, P.L. (eds), *Continental Extensional Tectonics*, Geological Survey Special Publication No. 28, pp 611-619.
- Hovland, J., Gubbins, D., and Husebye, E.S., 1981. Upper mantle heterogeneities beneath Central Europe, *Geophys. J. R. Astron. Soc.*, 66, 261-284.
- Husebye, E.S., 1982. (Editor), *The structure of the lithosphere-asthenosphere in Europe and the North Atlantic*. *Tectonophysics*, 90(1-2):1-262.
- Husebye, E.S. and Hovland, J., 1982. On upper mantle seismic heterogeneities beneath Fennoscandia. *Tectonophysics*, 90: 1-17.
- Husebye, E.S., Hovland, J., Christofferson, A., Astrom, K., Slunga, R. and C-E. Lund, 1986. Tomographic mapping of the lithosphere and asthenosphere beneath southern scandinavia and adjacent areas. *Tectonophysics*, 128, 229-250.
- Kinck, J.J., Husebye, E.S. and C.-E. Lund., 1989. The S. Scandinavia Crust - Structural complexities from seismic reflection and refraction profiles. *Tectonophysics*, this issue.
- Knopoff, L., 1972. Observation and inversion of surface wave dispersion. *Tectonophysics* 13: 497-513.
- Luosto, U., 1989. Crustal structures of eastern Fennoscandia. *Tectonophysics*, this issue.
- Meissner, R., 1979. Fennoscandia - a short outline of its geodynamical development. *Geo Journal*, 3.3, 227-233.
- Nolet, G., 1985. Solving or resolving inadequate and noisy tomographic systems, *J. Comp. Phys.*, 61, 463-482.
- Paige, C.C. and Saunders, M.A., 1982. LSQR: an algorithm for sparse linear equations and sparse least squares, *ACM Trans. Math. Soft.*, 8, 43-71 and 195-209.
- Planke, S., Skogseid, J. and Eldhom, O., 1989. Crustal structure off Norway, 62° to 70° North. *Tectonophysics*, this issue.
- Prodehl, C. and Kaminski, W., 1984. Crustal structure under the FENNOLORA profile. In : Galson, D.A. and Mueller, S. (eds), *First EGT Workshop : The Northern Segment*, 53-68. European Science Foundation, Strasbourg, 169 pp.
- Ruud, B.O., Husebye, E.S., Ingate, S.F., and Christofferson, A., 1988. Event location at any

distance using seismic data from a single, three-component station, *Bull.Seism.Soc.Am.* 78, 308-315.

Spakman,W. and G.Nolet, 1988. Imaging algorithms, accuracy and resolution in delay time tomography, in, *Mathematical Geophysics; a survey of recent developments in seismology and geodynamics*, edited by N.J.Vlaar et al., Reidel, Dordrecht, 155-188.

Spencer,C.P. and Gubbins,D. 1980. Travel-time inversion for simultaneous earthquake location and velocity structure determination in laterally varying media, *Geophys.J.R.astr.Soc.*,63, 95-116.

Talwani,M. and Eldholm,O. 1977. Evolution of the Norwegian-Greenland Sea. *Geol.Soc.Am.Bull.* 88, 969-999.

Theilen,F. and Meissner,R. 1979. A comparison of crustal and upper mantle features in Fennoscandia and the Rhenish Shield, two areas of recent uplift. *Tectonophysics*, 61, 227-242.

Wolff,F. 1983. Crustal structure of the Scandinavian Peninsula as deduced by wavelength filtering of gravity data. In: Schenk,P.E. (ed.) *Regional Trends in the geology of the Appalachian-Caledonian-Hercynian-Mauritanide Orogen*, Reodel, Dordrecht.

Ziegler,P.A. 1988. Evolution of the Arctic-North Atlantic and the Western Tethys. *AAPG Memoir* 44, USA.

Figure captions:

Fig.1: The model of Moho depth. The shading is from 9 km (dark) to 55 km thickness (light shade).

Fig.2: The distribution of events (circles) and seismic stations (triangles) within Fennoscandia. Circled symbols refer to the national symbols of Norway (N), Sweden (S), Finland (SF) and Denmark (DK). P.Z. = protogine zone, B.B. = Bothnian Bay, S.F.Z. = Senja Fracture Zone, JMFZ = Jan Mayen Fracture Zone.

Fig.3: Reduced travel time ($V_{red} = 9$ km/s) versus distance of all arrivals reported in the Fennoscandian seismic data base, Jan 1984 - May 1988. The polygon windows delineate the Pn (lower window) and Sn (upper) arrivals that were accepted in the initial data selection.

Fig.4: The spatial coverage of Pn raypaths used in the inversion. The Sn raypaths is not visually different.

Fig.5: Epicenters of the events. The circles refer to the epicentral locations following the inversion procedure, the attached lines indicating the shift from the initial Finland data center locations.

Fig.6: Reconstructions from synthetic data. (a) Synthetic model involving a pattern anomaly with blocks of velocity 7.9 km/s (dark shade) and 8.5 km/s (light shade) set within a background velocity of 8.2 km/s. (b) The reconstruction of this synthetic model, shading ranges from 8 km/s (dark) to 8.36 km/s (light). (c) Synthetic model involving horizontally oriented anomalies, initial velocities as in (a). (d) Reconstruction of (c), velocity range: 8 km/s (dark) - 8.3 km/s (light).

Fig.7: P-wave velocities estimated from the real data. Shading ranges from 8.04 km/s (dark) to 8.3 km/s (light). A reference velocity of 8.18 km/s was used in the initial model.

Fig.8: S-wave velocity estimates. Shading from 4.61 km/s (dark) to 4.69 km/s (light). A reference velocity of 4.65 was used in the initial model.

Fig.9: Geology of Fennoscandia (following Berthelsen, 1987). SF - Svecofennian province, PZ - Protogine Zone, SN - Sveconorwegian orogen, A - Archean nucleus, JMFZ - Jan Mayen Fracture Zone, SFZ - Senja Fracture Zone, ESC - Faeroe-Shetland and Vøring Plateau escarpments (southern and northern ESC respectively), FBZ - Fennoscandian Border Zone. Bathymetry is marked in hundreds of meters (dotted lines).

Fig.10: Map of long wavelength Bouguer gravity anomalies (Balling, 1984). Contours are at 20 mgal intervals.

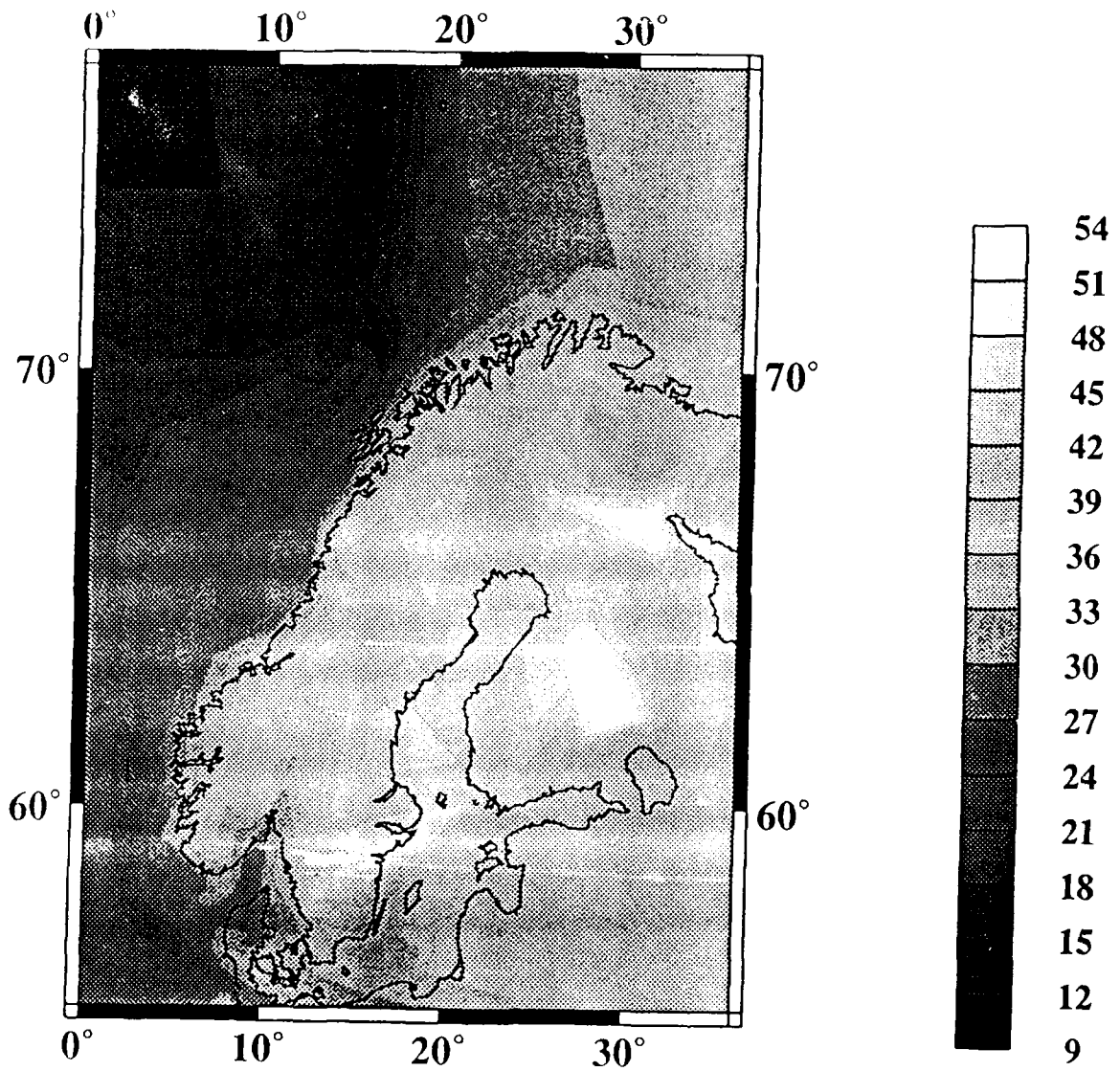


Fig. 1

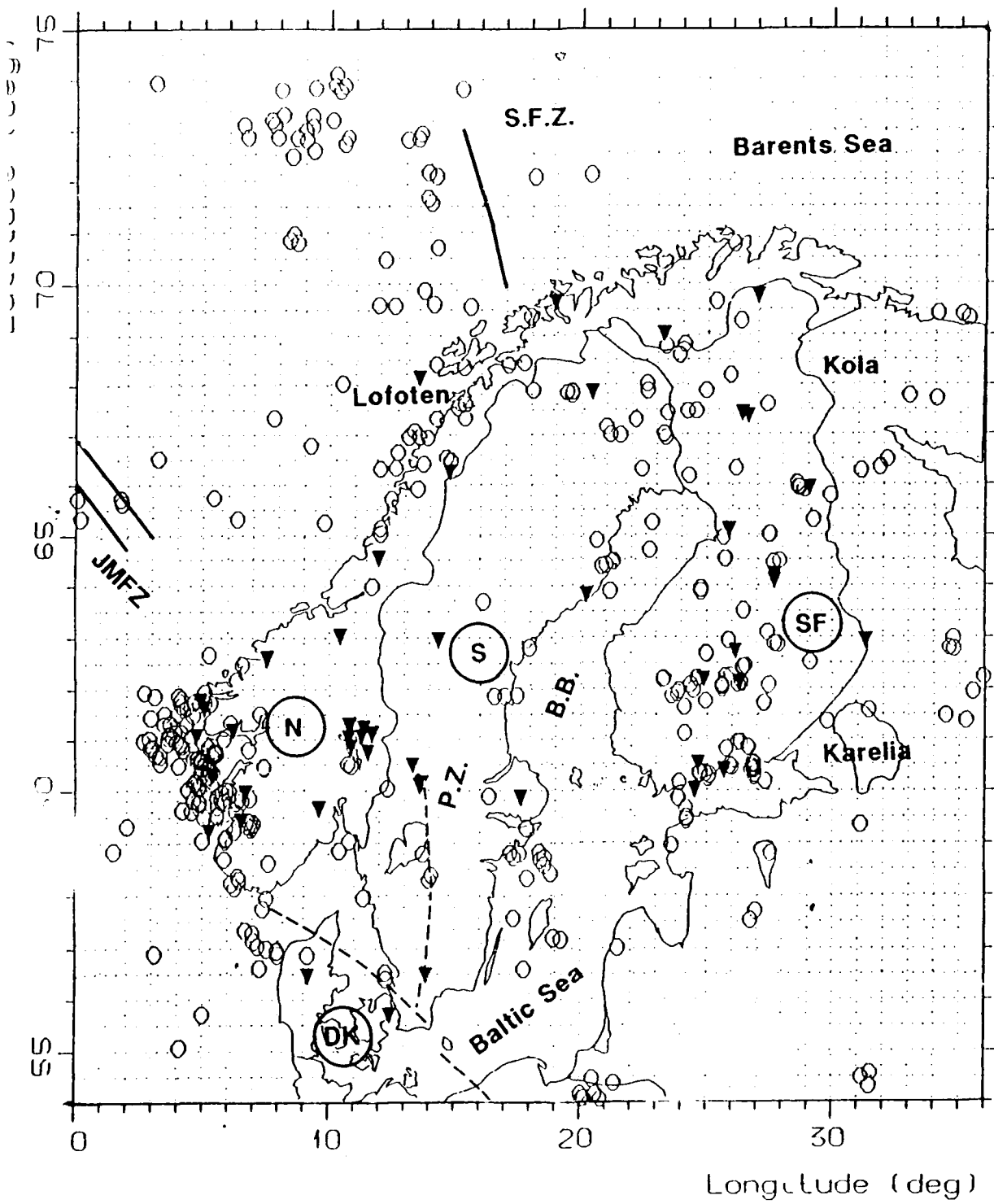


Fig.2

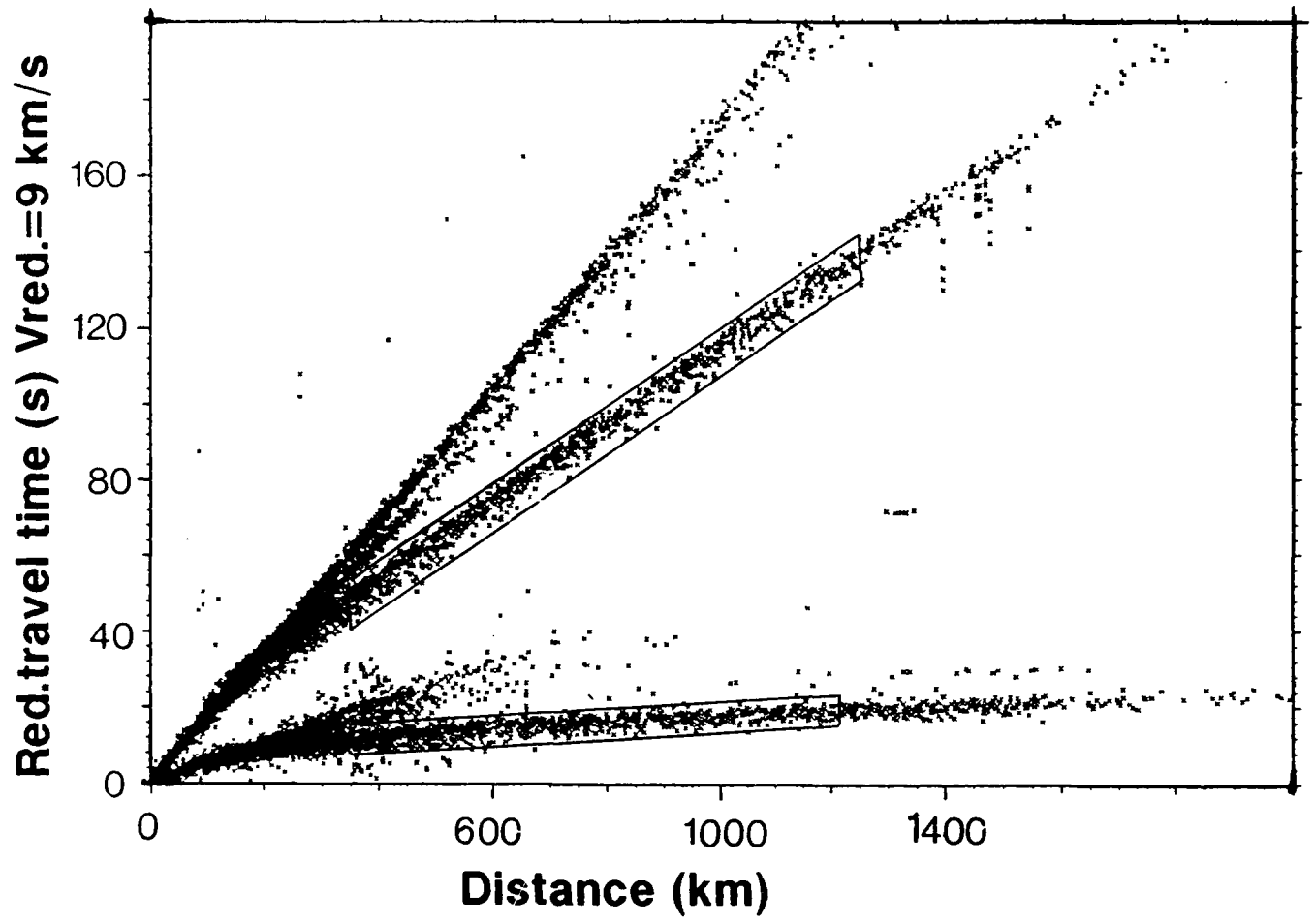


Fig.3

PN RAYS

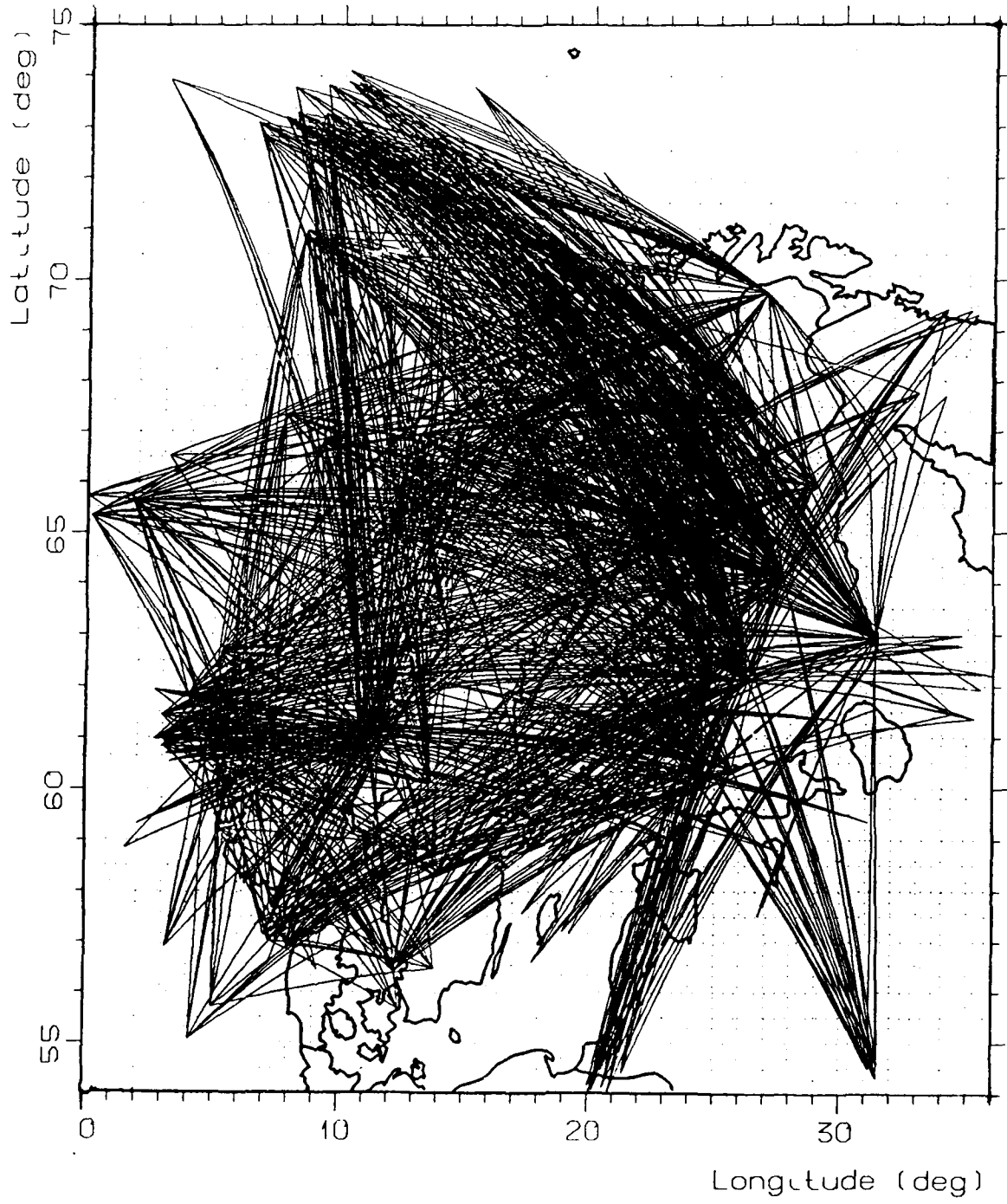


Fig.4

EPICENTERS

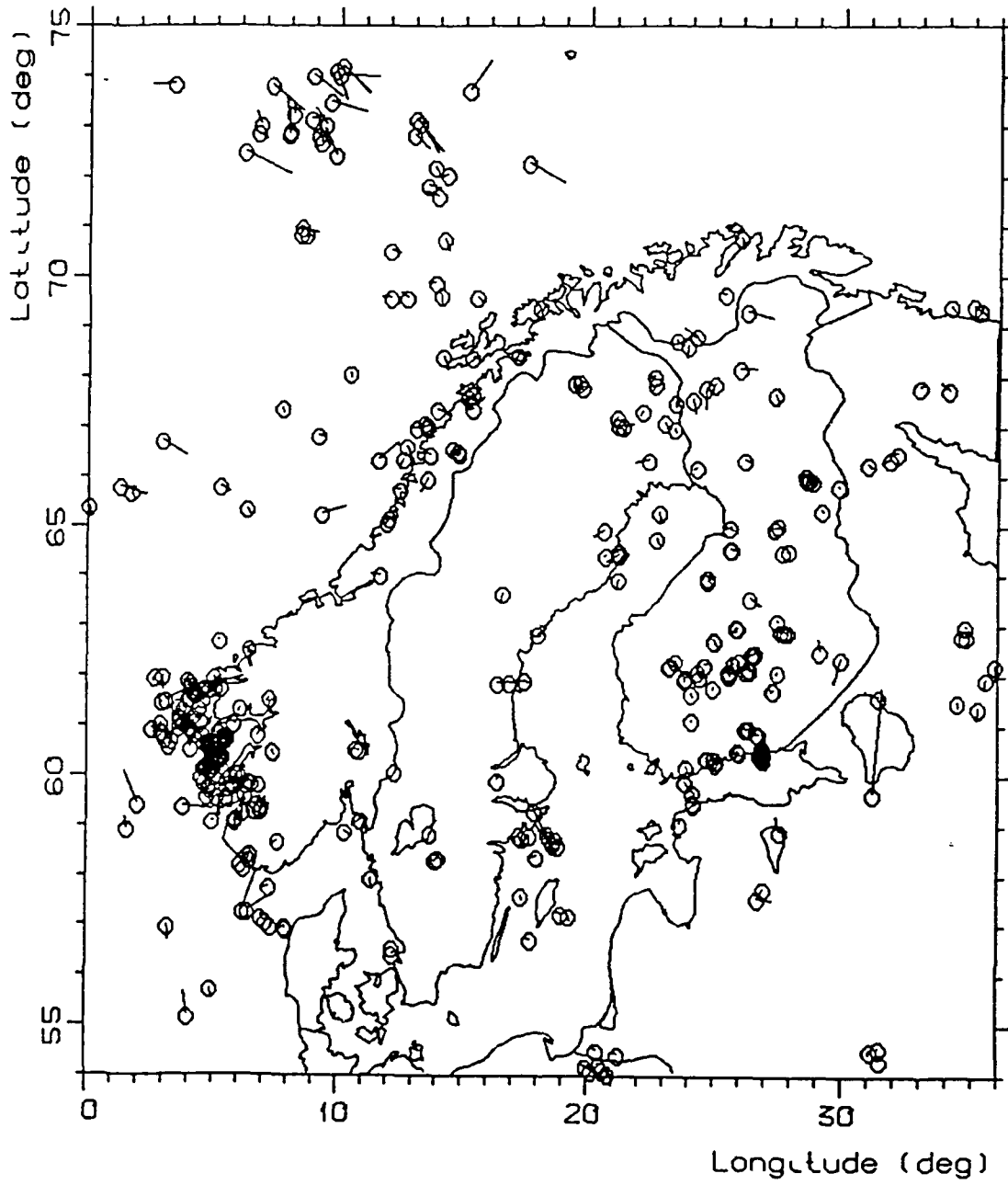


Fig.5

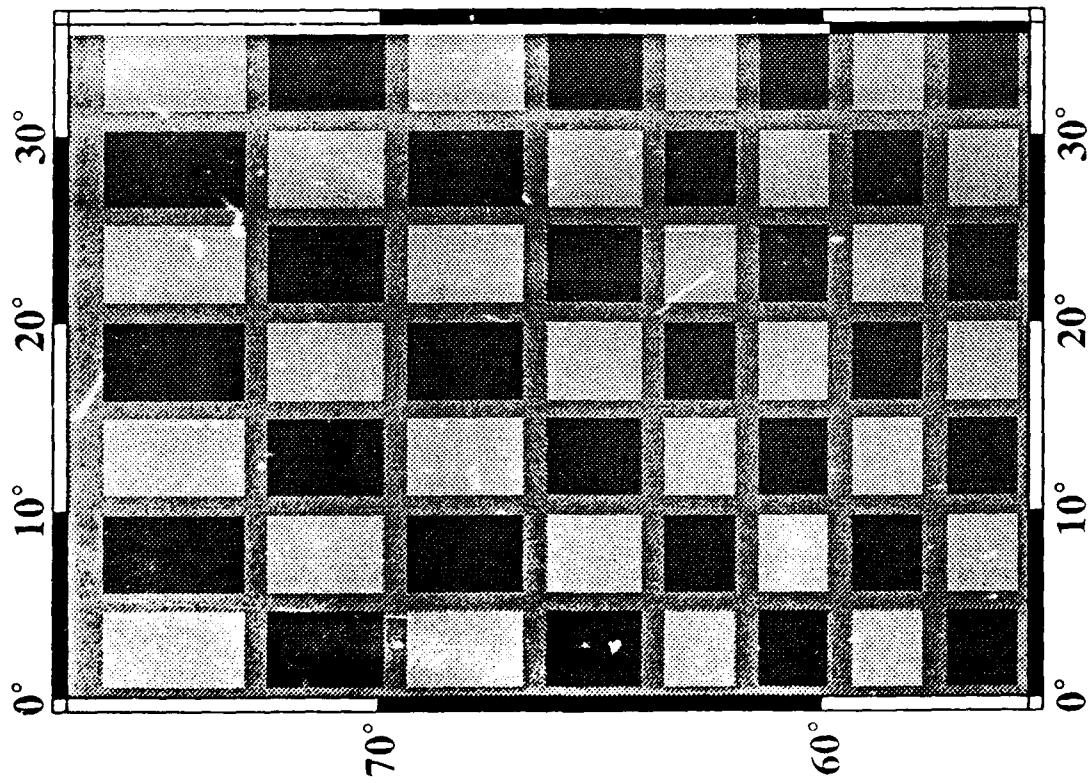


Fig.6a

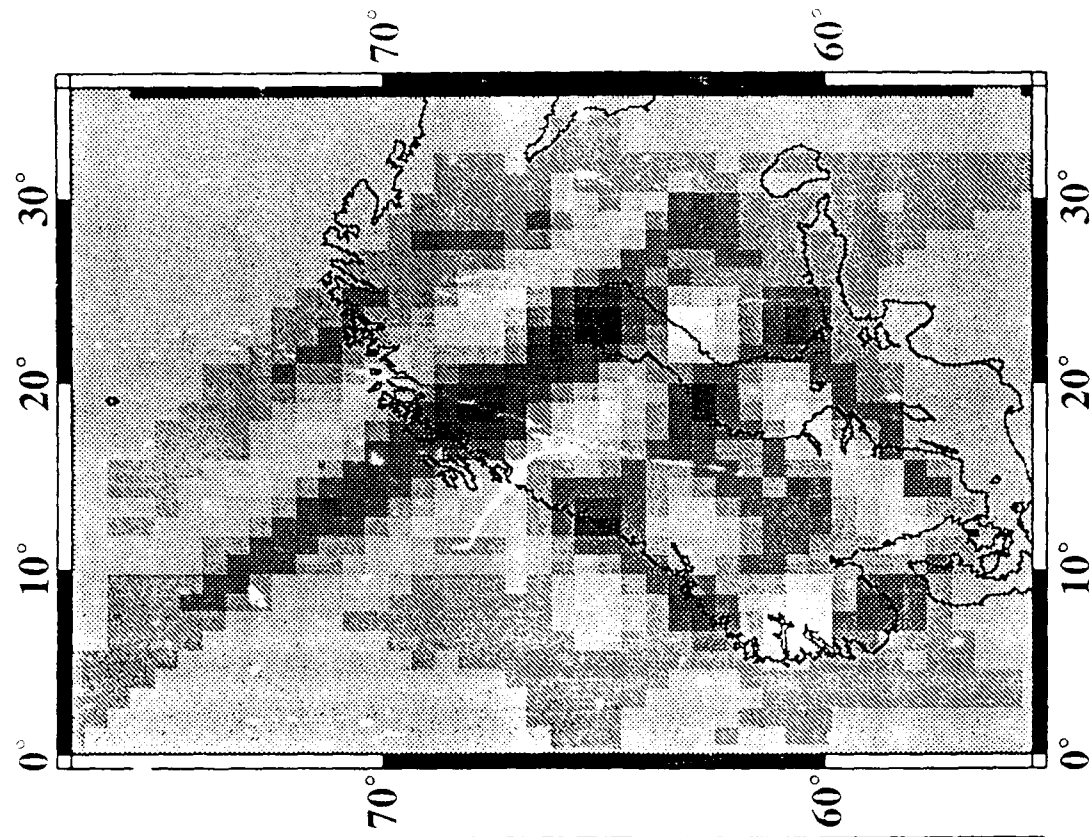
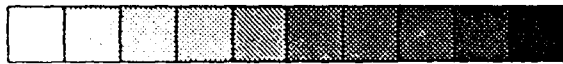


Fig.6b

8.3
8.27
8.24
8.21
8.18
8.15
8.12
8.09
8.06
8.03
8



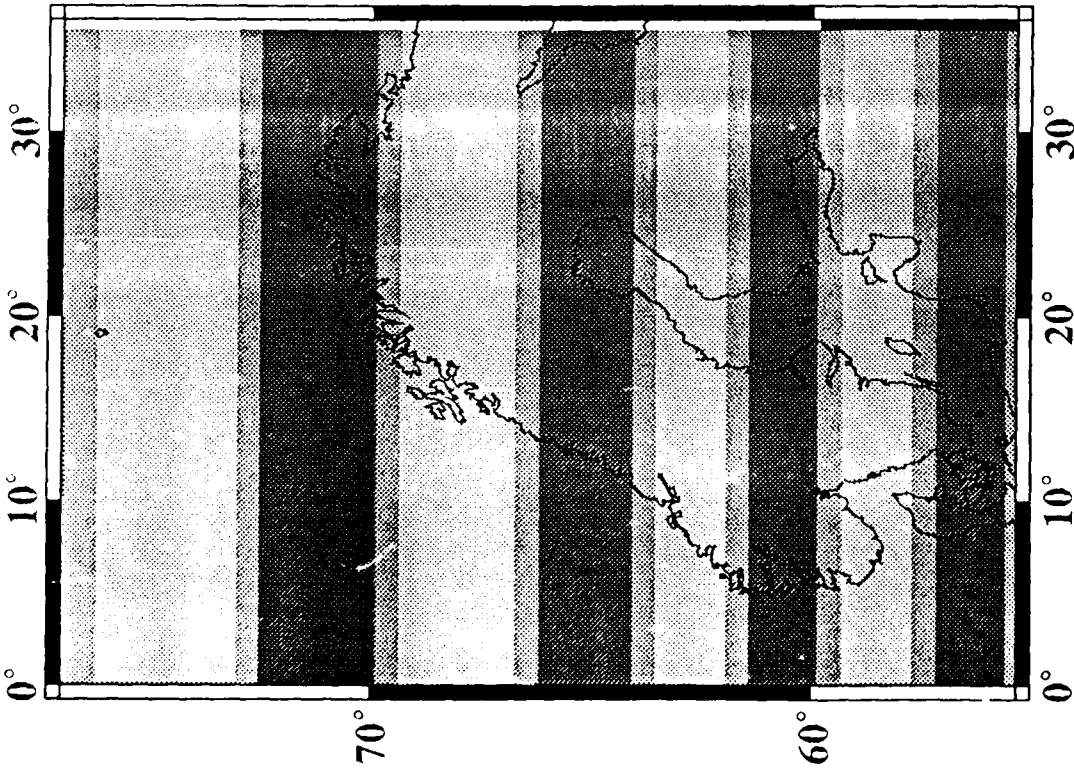


Fig.6c

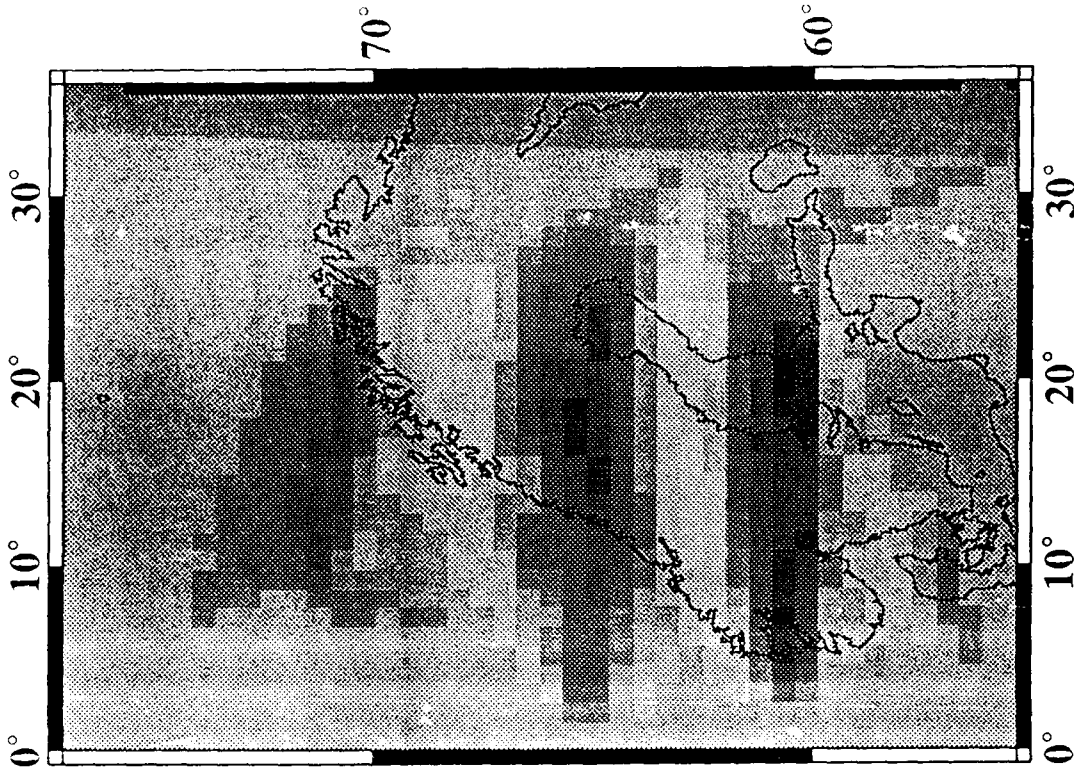
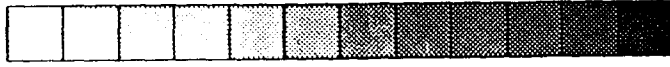


Fig.6d

8.39
8.38
8.33
8.29
8.24
8.2
8.17
8.15
8.12
8.09
8.06
8.03
8



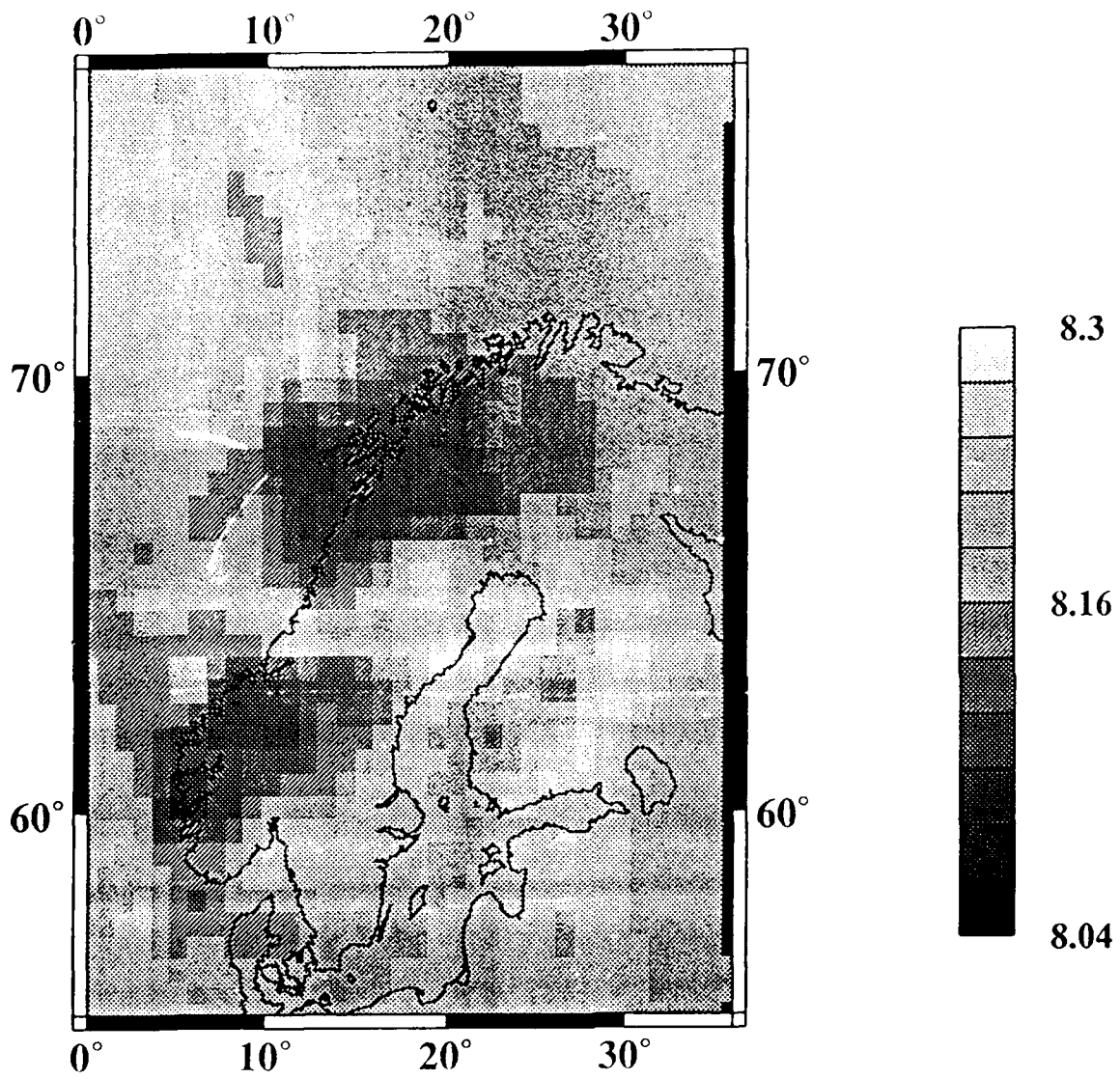


Fig.7

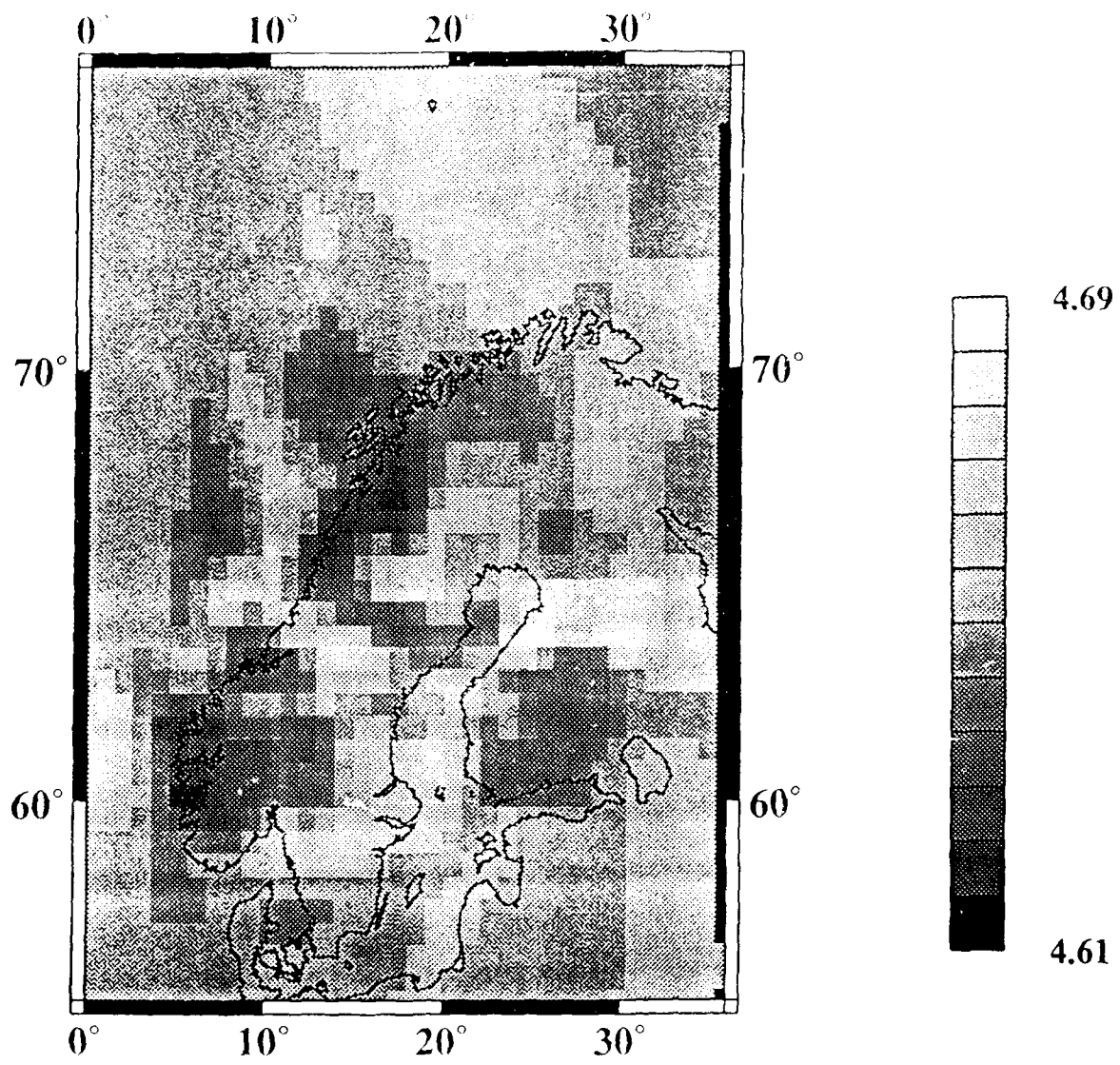


Fig.8

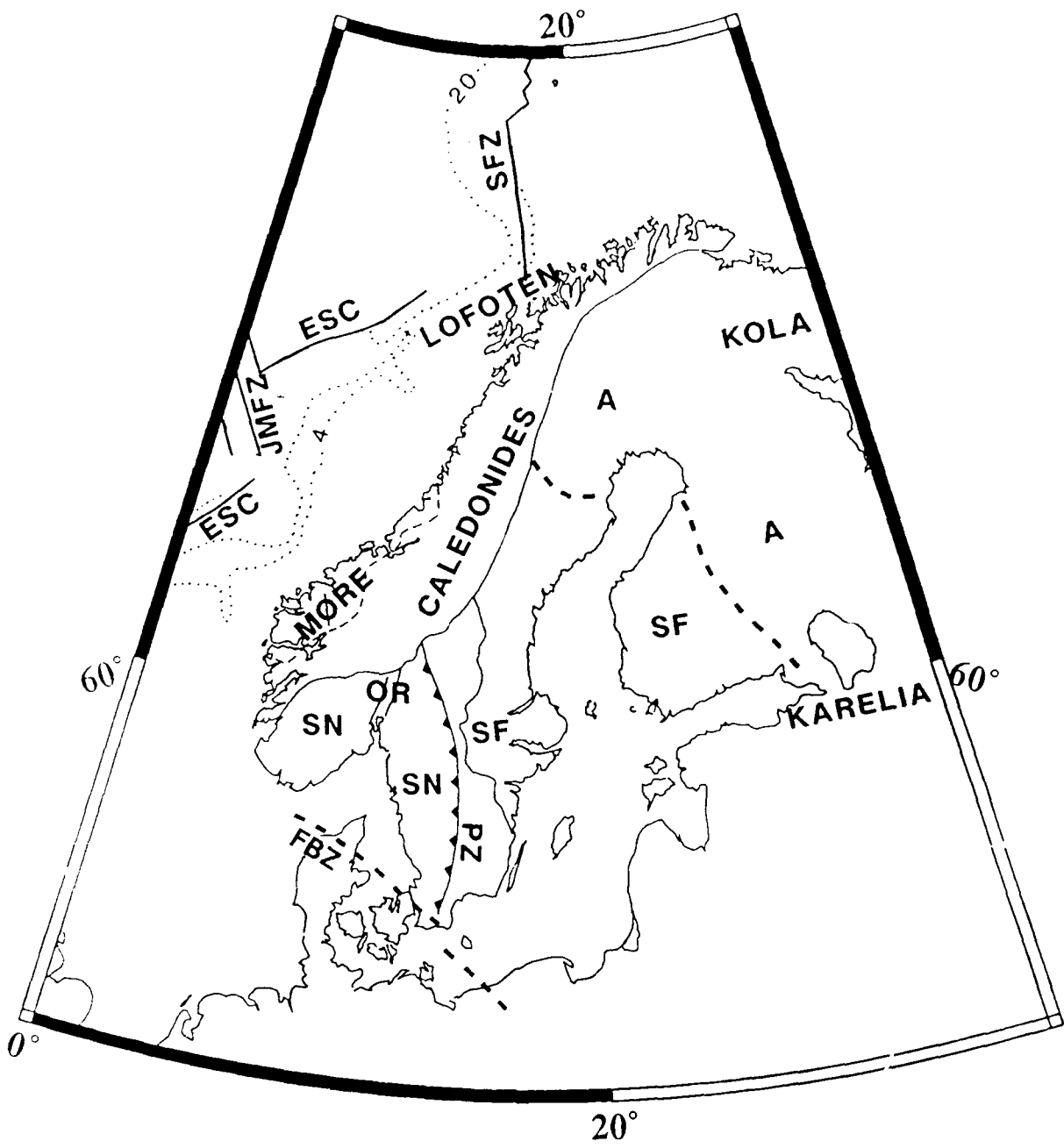


Fig.9

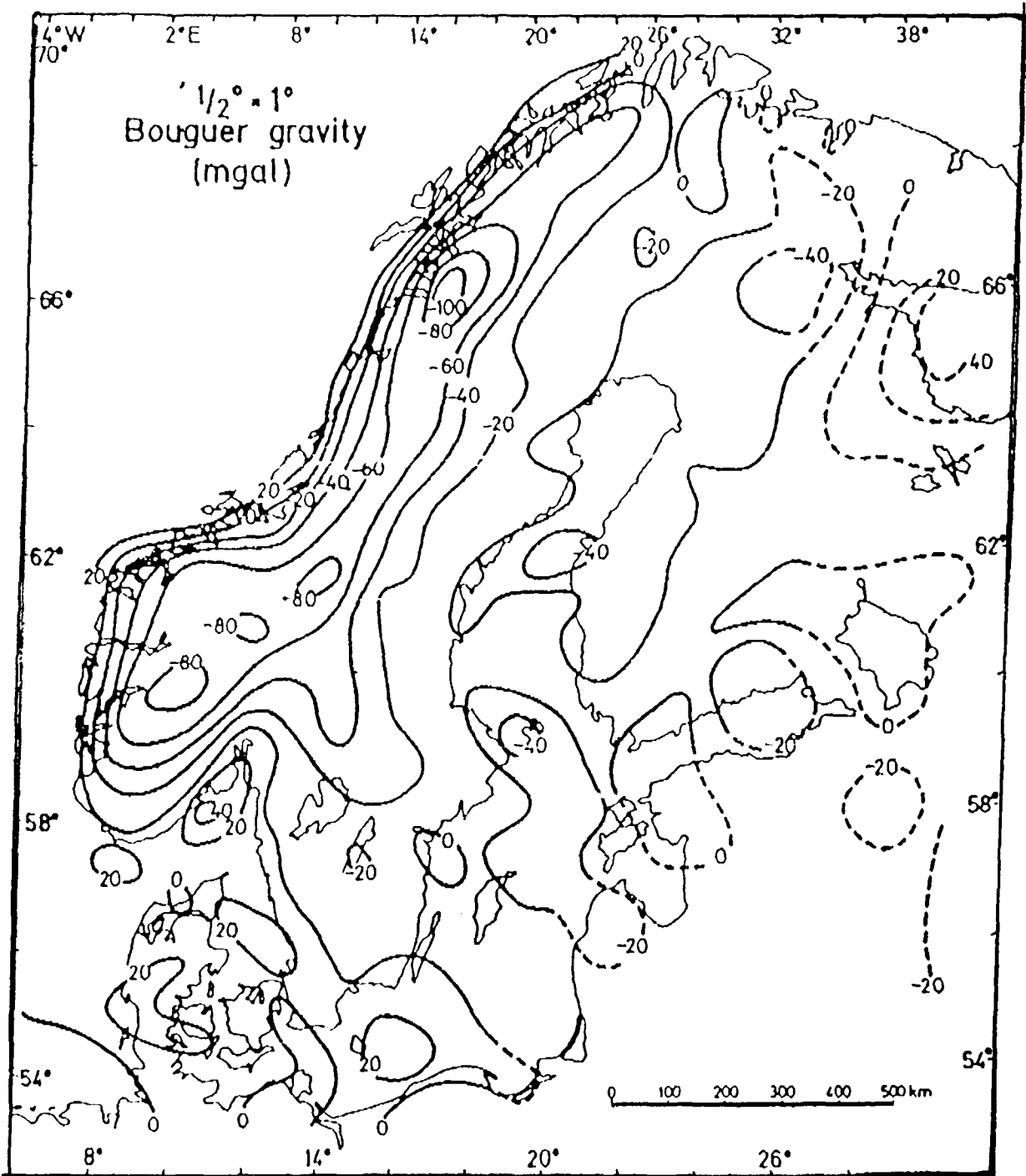


Fig. 10

**Teleseismic P-coda analyzed by three-component and array techniques -
deterministic location of topographic P-to-Rg scattering near the NORESS array.**

Bannister, S.C.¹⁾, Husebye, E.S.^{1,2)} and Ruud, B.O.¹⁾

¹⁾Dept. of Geology, Oslo University,
P.O. Box 1047, Blindern, N-0316 Oslo 3, Norway.

²⁾On leave of absence from NTN/NORSAR,
P.O. Box 51, N-2007 Kjeller, Norway

Abstract

P-wave coda of 75 s duration from 8 teleseismic events of widely different azimuths and depths as recorded by the NORESS array, Norway, have been examined using both array and 3C analysis techniques. The array data have been analyzed using the semblance technique which allow us to determine with good accuracy both time of arrival, apparent velocity and azimuth of the scattered waves. Coda coherency was found to vary considerably, probably reflecting extended source duration for some events. By subtracting the teleseismic beam from the records, locally scattered wavelets can be resolved even within highly coherent teleseismic P-coda. Although source-end scattering could not be separated from the source pulse per se, we favor the hypothesis of long source duration supported by observed slow beam amplitude decay rates. The majority of receiver-end scattering contributions appears to be P-to-Rg conversion in both forward and backward modes from two nearby areas with pronounced topographic reliefs, namely Bronkeberget (Dist~10 km, Azi~80°) and Skreikampen (Dist~30 km, Azi~225°). The scattering is multiple in the sense that both the primary and secondary phases from the source region contribute to the Rg-scattering. P-to-S scattering

constitute a significant part of receiver-end scattering but is more diffuse than Rg. Also here the Rg preferred azimuth directions are found, but the forward direction is important as well. P-to-P scattering is weak and mostly confined to the immediate vicinity of the array. The analysis of individual 3C stations shows high sensibility to interference with locally scattered waves which are probably responsible for a marked decrease in apparent velocity observed for some events 3-4 s after P-onset. To fully utilize the potential of 3C instruments for phase identification in an integrated array/3C processing scheme, at least one additional 3C station within the NORESS array would be necessary.

1. Introduction

The classical earth model involving spherically symmetric layers is valid only as a first approximation besides being useful in the computation of synthetic seismograms.

Although dominant and deterministic seismogram features like P, S and surface waves can be accounted for using such models, their codas cannot be. Coda waves arriving after deterministic phases are broadly attributed to seismic wave scattering phenomena associated with lateral heterogeneities, located within the crust and mantle while precursors to PKIKP and related phases reflect heterogeneities near the core-mantle boundary. Velocity and density heterogeneities, in addition to generating coda waves, can cause changes in waveform, phase (or travel time) and amplitude fluctuations as well as attenuation of the direct (deterministic) phase arrivals. Overall the seismic wave scattering reflects the dominant seismic wavelength of the seismic signal relative to the scale length of the heterogeneities, which may vary from the grain size of rocks to the lowest mode of global spherical harmonics; an instructive overview is given by Wu and Aki (1988)

Seismic wave scattering in a heterogeneous earth has motivated numerous theoretical studies. Most of these studies are aimed at obtaining approximate solutions to the wave equation for a medium characterized by a few parameters such as scale length and perturbation index (rms variation of velocity and density). Other studies concentrate on calculating the seismic response of wedge structures, Moho and topographic undulations and geological structures of irregular geometries. In this kind of studies it is not always

clear which propagation effects (e.g. mode conversion, diffraction and medium-related anisotropy) are included. Some of these problems can be reduced by using finite element methods (e.g., see Frankel, 1989 and Herraiz and Espinosa, 1987).

Observational studies of wave scattering effects are problematic due the weak signal correlation, even when using small arrays. This seems to be one reason why observational scattering parameters are often tied to coda envelopes and decay rates while wave types and associated propagation paths constituting the coda waves are often not specified. An exception is naturally the amplitude and phase fluctuations of initial P-wave arrivals, as demonstrated by Aki (1973) and Berteussen et al (1975) using the random media theory of Chernov (1960). These studies led to the tomographic mapping approach or the ACH-method of Aki et al (1977).

In this study we focus on attributes of P-coda waves as recorded by the small aperture NORESS array in southern Norway (Fig. 1 and Ingate et al, 1985). The aims of our study are two-fold, namely to attempt to decompose the coda waves into specific phase arrivals and associated slowness vectors and secondly to provide an insight into the scattering processes most important in generating the coda waves of teleseismic P-signals.

2. P coda generation - source or receiver contributions ?

An important parameter in scattering theory is the dimensionless quantity ka where k is the wavenumber and a the correlation distance in random media theory or scale length of the structural heterogeneities. For teleseismic P-coda with frequencies in the range 1-3 Hz and structural heterogeneities of the order of 0.1 to 10 km, the factor ka may vary from 0.1 to ca 30. The latter sizes of heterogeneities have been confirmed from P-phase and amplitude studies in the area of the NORESS site (e.g. see Aki et al., 1977, Haddon and Husebye, 1979 and Flatté and Wu, 1988) while the smaller scale length of ca. 1 km or less has been observed in many scattering studies around the world from coda analysis of high frequency local events. Small angle or forward scattering would be important for $ka \gg 1$ in which case sections of the coda should realistically be in the source direction. When $ka \sim 1$ however, wide angle scattering contributions are

expected to be relatively strong, with large angle scattering relative to a given azimuth direction. Conversions between different wave types are by far most efficient when structural anomalies are both in velocity and density. The crust and the surface topography are on this basis likely to play an important role in scattering generation. Second-order or doubly scattered wavelets are generally considered to be of little importance since the earth appears to be weakly heterogeneous, i.e. density and velocity rms fluctuations seldom exceed 5%. The relative excitation of the coda may vary with wavelength or equivalent signal frequencies given that the scatter length distribution is peaked, say, around 10 km.

Scattering may conceptionally be thought of as occurring in three principal areas, namely in the source region of the earthquake, along the wave path in the mantle (say below 400 km) and finally, near the receiver. We discuss each of these separately below.

Source area scattering : The size and focal depth of an earthquake is obviously of some importance, at least in regards to the time duration of scattering within the source region. Scattering contributions may arise from either multiple P-reflections within the crustal and lithospheric layers and/or S- or R-wave conversions to P. Intuitively the coda contribution of near-source scattering is expected to be relatively coherent when observed at teleseismic distances because of the small variation in take-off angle. To study source-end scattering it would be necessary to use data from several stations, e.g. see Lynnes and Lay (1989).

Transmission path scattering : For relatively short distances of 20-30° layered structures within the lithosphere and asthenosphere may act as a waveguide, thus contributing significantly to the P coda as demonstrated by Kennett (1987) and Korn (1988). Somewhat similar effects have been noted by King et al (1977) in the analysis of PP precursors where distinct differences between observed slownesses were attributed to $P_{400}PP$ at the source-end and $PP_{400}P$ at the receiver end of the propagation path.

Receiver end scattering : In general there is some differentiation here between two effects; that resulting from large scale heterogeneities, including continental and oceanic transition structural regimes, such as off the west coast of Norway, and secondly, small

scale scatterers in the crust and lithosphere, including rough topography. P-to-Rg conversion should be effective in the latter case if the topography undulations at least are of the order of half the Rayleigh wavelength of approximately 1-2 km (Frankel, 1989). The west Norway mountain area ca 100-300 km away from the NORESS seismic array is thus a candidate for this kind of scattering.

3. Data and analysis technique

As several coda wave mechanism may contribute we attempt to isolate individual scattering sources through careful event selection. Table 1 indicates good azimuth coverage, thus illuminating potential scatterers from a multitude of directions. We have used both 3C recordings from the four 3C stations within the NORESS array (Fig. 1) and vertical component data from the whole array. The essential signal parameters extracted for deducing wave type and propagation paths are polarity (particle motion) and slowness vectors in specific time windows.

Analysis techniques

In coda analysis optimum use of the various filtering options in the context of array wave field recording is important. To suppress part of the ambient noise band-pass filtering in the range 0.5-3.0 Hz are used. Source-end scattering contributions and the signal pulse itself are taken to be equivalent to the beam trace resulting from aiming the array towards the epicenter. The residual trace, that is, the difference between single sensor records and the beam trace, would enhance receiver-end scattering contributions. Beam-forming on the basis of residual traces would then give a relative powerful tool for pin-pointing scattered wavelets. Simple rotation of the NS- and EW-components into radial and transverse components relative to the epicenter and/or scattering sources would naturally serve to isolate specific wave types in the records.

Data analysis included f-k and semblance analysis (Husebye and Ruud, 1989), both of which have good separation of body and surface waves even for a small aperture array like NORESS. We also experimented with semblance velocity-analysis of the radial and transverse components of the four 3C stations (Fig. 1), but the results were not

instructive due to the odd configuration of this mini-array. At least one additional 3C station is needed in the C-ring.

3C analysis techniques available include that of Vidale(1986), Park et al (1987), Plesinger et al (1986), Jurkevics (1988), Christoffersson et al (1988) and Roberts and Christoffersson (1990). We have used the latter in our coda analysis. This technique works in the complex demodulate domain, a complex time domain, efficiently decomposing 3C signals to obtain instantaneous estimates of the real and quadrature parts (amplitude and phase) of the energy within selected frequency bands. Various attributes of the seismic coda can be easily obtained from the array and 3C records. Below we outline several attributes used in this study.

Wavelet azimuth: The azimuth is estimated from the observed cross-spectral densities between the horizontal and vertical components. Although this estimate is instantaneous, some averaging within a window of around 1 cycle is usually done to improve stability. In the analysis of array data the slowness vector (apparent velocity and azimuth) is tied to the maximum beam power (f-k) or the maximum coherence (semblance).

Incidence angle and apparent velocity: The incidence angle is determined from the cross-spectral density between the vertical and radial components. This angle can be converted to a velocity estimate given assumptions about the local P-wave velocity and Poissons ratio or using known epicenter locations for calibration. For an array the apparent velocity is estimated directly from move-out times; the resolution is poor when the apparent wavelength of the signal greatly exceeds the array aperture, and for NORESS this apply to the entire teleseismic window.

Phase difference between components: We can examine the instantaneous phase difference between the rotated radial and vertical component, or equally between other pairs of components, using the phase information retained in the 3-component analysis. A phase difference of 180° corresponds to pure P wave particle motion, 0° difference represents pure SV wave particle motion while a phase difference of $\pm 90^\circ$ represents elliptical particle motion, as expected for example for Rayleigh waves but also for SV waves with post-critical incident angles.

Array semblance and 3C signal polarity: Our confidence in the above derived signal attributes depends on the associated semblance and polarity estimates. Semblance values (A0 plus C- and D-ring) for random data seldom exceeds 0.2 for the frequency range and time window lengths used. If corresponding values are observed in the coda sections they are considered marginal or not significant unless the associated slowness vector estimates remain stationary over a few cycles. For 3C analysis we have different measures on the extent of polarity of the signals at hand, including the chi-square model fit measure of Christoffersson et al (1988) where the significance is marginal for values below 0.5. To avoid lengthy explanations we use a common denominator for both semblance and polarity measures - the term signal coherency.

Practical considerations: The major difficulty faced in coda analysis is that of dealing with interference resulting from multiple wavelets arriving, at least partly, simultaneously. In such a case the recorded signal involves rapid variations in the polarization, with fluctuations in both calculated azimuth and angle of incidence. The above signal attributes are calculated using a sliding-window approach. Window lengths are around 1-2 cycles (1-2 s) while the updating frequency is 1/3 or 1/4 of this length. Overall we concentrate on separating signals where the polarization, phase, semblance and slowness are such that clearly definable phases exist, examining their consistency over time and their spatial correlation across the NORESS array.

4. Results

Altogether 8 events were subject to analysis and the results would be presented along the classical scattering subdivision of source- and receiver-end contributions. Then appropriate individual event results would be addressed in some detail. Hypocenter information is listed in Table 1 while trace displays are in Fig. 2. In general we have that events to the south and west, that is MAD, LEE, ALA (Fig. 2b) are of relatively low frequency and besides these events also have a relative long P-signal duration. The latter also applies to the HK1 event (Fig. 2a), a Hindu Kush earthquake with a focal depth of 100 km, which appear to be a double/triple event. A quantitative measure of P-signal duration including source-end scattering is given in Table 2 and Fig. 3. Note that the deep events JAP and HK2 and the SEM explosion have a very strong source pulse of 3-5 s duration (Fig 2a),

but the source-end scattering contributions result in a total duration of more than 60 s in terms of coherent P-teleseismic arrivals (Fig. 3).

4.1 Source-end scattering.

The prime characteristics here would be that scattered pulses are P-type when observed at the receiver in the early P-coda and this naturally implies that scattering and complex source pulses are not easily separated. Anyway, 3C techniques were found convenient for source-end scattering analysis, and relevant results here are displayed in Fig. 2. To familiarize the reader with the 3C-results these are discussed in some detail for the Kamchatka (KAM) event (Fig. 2a). The records for site A0 have been bandpass filtered and rotated with the radial component in the source azimuth direction. Processing parameters are explained in the figure caption. An important note is that the azimuth-coherency and velocity plots in the Fig. b and d are based on the assumption of P-wave presence while there is no such assumption on wave-type with the calculated phase shift between vertical and radial components. Note that for wavelets with azimuth directions greatly off 'true' azimuth the observed phase shifts are not directly interpretable in P, S and Rg-types. Signal coherency and hence confidence in azimuth estimates are good for the first 7 s of the signal (5-12 s) as seen in the upper left corner of the figure. A small discontinuity at 8-9 s has a counterpart in the R-Z phase diagram and besides marks a transition to a pronounced drop in apparent velocity. Between 12-13.5 s signal coherency is low (below 0.5) while the phase shift drops toward 90° , implying elliptical particle wave motion. From 13.5 to 15 s the signal coherency is again high and the associated phase shifts are typical P-wave. This contrasts with the values between 17 and 20 s where coherency is good but the phase shifts in Fig. 3c imply elliptical motion. In the remaining parts of the displayed records, signal coherency is mostly low and particle motion is predominantly elliptical, fluctuating mainly between 90° and 270° .

Corresponding velocity estimates are calculated at a lower coherency level (above 0.2), subject to the condition that the standard deviation of the estimate is less than 1.6 of the actual velocity value. The very reliability of the obtained velocity estimate is probably poor, the low coherency representing strong interference from non-P wavelets. To summarize the 3C results for the KAM event, strongly coherent P-wave motion in the first part of the record together with the estimated azimuth and apparent velocity are very close to that expected for the event location. After about 3 s we have a sharp drop in

velocity although the azimuth does not change significantly.

The 3C results from the other 7 events also in Fig. 2 are not much different from those typical for KAM. The common characteristics are as follows; the phase shift results imply that interference starts 3-4 s after P-onset and often are so prominent that velocity and azimuth estimation fails. Also, phase shifts fluctuate between $90-270^\circ$ and thus indicate a dominance of elliptical (Rayleigh) wave motion. Later arriving P-wavelets are seldom although the HK1, MAD, LEE and ALA events have extended P-signal duration. Another feature is that the P-velocity sometimes drop significantly after just 3-5 s (e.g. KAM, LEE, ALA). This is rather puzzling since the time lag between direct P and 'secondary' P-wavelets are small, and thus difficult to explain except for sort of multipathing confined to the azimuth plane. Using the array per se, we have calculated apparent velocities using A0, C-, and D-ring and here the observed velocity decreases are very moderate. However, the 5C results have a counterpart in the displayed traces as the energy on the radial components increase faster than the vertical components after the P-onset. From Table 2 it is obvious that the vertical components are rather coherent across the array compared to the 3C records being far more sensitive to interference. This point is further illustrated in Fig. 3.

4.2 Receiver-end scattering.

From the above discussion and also from Fig. 3 it is clear that source-end contributions are rather energetic. We have removed such effects by forming the beam trace, subtracting this from the single z-traces and then conducting semblance analysis on the residual traces. We have screened the coda in two segments of 40 s (Fig. 2 shows the traces in the first segment) for P (6-8 km/s), Sn (4.5 km/s) and Rg (3.0 km/s). In the first time segment, the coda appears to be dominated by Rg-contributions as shown in Fig. 4. The truly striking features are that the P-to-Rg scattered wavelets mainly come from two principal azimuth directions of 80° and 225° (thin lines in the figure) irrespective of event azimuths. Examples of estimated Rg waveforms are shown in Fig. 5. With the time lags involved, we have located the corresponding scattering source areas to Bronkeberget (Dist~10 km, Azi~ 80°) and Skreikampen (Dist~30 km, Azi~ 225°). These areas have prominent topographic reliefs, and are marked in Fig. 1. Furthermore, the scattering

appears to be multiple in the sense that Pg-wavelets arrive repeatedly from the two azimuth directions. This is perhaps most clearly illustrated for the ALA event where the timelags between scattering pulses on the 80° and 225° azimuths forms a distinct pattern. Seemingly Rg-attenuation is very strong since wavelets from larger distances and other azimuths are hardly observed, not at least in view of mountainous area to the north and west (60 km or more away). Semblance analysis was performed for 4.5 km/s velocity and the main results here (not shown) have many similarities to those in Fig. 4. With this is meant that the two semblance patterns have a considerable overlap probably due to 'true' velocities around 3.6-3.8 km/s typical of Sg-phases. However, from the phase shift results and from a good overlap in azimuth and time we consider Rg-wavelets to dominate. An exception here is the high semblances for ALA at about 50° (30-35 s) which are much stronger in the 4.5 km/s results. A search for crustal P-phases (6-8 km/s velocity range) turned out to be mainly negative. We found a few Pg-phases at 4-6 s after P-onset time but hardly later in the coda. This implies that P-to-P scattering in the general array siting area is weak.

Results from semblance analysis in the second time segment (35-75 s after P-onset) for velocities of 3.0 to 4.5 km/s are shown in Figs. 6 and 7. There are still some Rg-contributions apparent and again mainly along the 80° and 225° azimuth directions. The preference for the above two azimuth directions in Fig. 6 we again take to signify that the scattering is multiple since source-end arrivals are still present far into the coda as shown in Fig. 3. From Fig. 7 we see that S-type scattering dominates in this time segment. This is explained in terms of relative less pronounced S-wave attenuation as compared to Rg, as over time more distant scattering source areas may become activated. Still there is some preference for the 80° and 225° azimuth directions, but also forward scattering appears to be significant, in particular for the two northern events KAM and ALA, but also for SEM and HK events to the east. P-to-P scattering at the receiver-end, tied to crustal velocities in the range 6-8 km/s, remains weak.

5. Discussion and Conclusions

The P-teleseismic coda has also been examined by others, and we would briefly review the outcome of such studies. Already two decades ago Key (1967) identified discrete

arrivals in the P-coda at the Eskdalemuir array in Scotland which suggested P to Rayleigh wave scattering stemming from the local topography. Recently Langston (1989) inferred Rayleigh wave scattering just after the P-arrival in 3C analysis of teleseismic recordings at Pasadena, California. Of most interest for our study is investigations by Dainty and Harris (1989), Dainty (1990) and Gupta et al (1989) on the basis of f-k analysis of NORESS teleseismic codas. Dainty and Harris found evidence of significant low-velocity scattering contributions mostly attributed to Lg and surface waves without detailing azimuth or time dependencies. Gupta et al reported low velocity secondary arrivals in the early P-coda to the east and south-west. Our preference for using the semblance technique in the array data analysis instead of high resolution f-k methods is due to the fact that semblance works well even for short windows (1-2 cycles) and thus the individual slowness estimates can be directly related to arrivals seen in the records. As also demonstrated here, the 3C records are useful for pin-pointing where wave interference take place, and naturally the information potential of the horizontal components should be realized in coda studies.

5.1 Mechanism for NORESS P-coda generation:

Although teleseismic scattering is generally rated a complex problem, the NORESS coda observations as presented in the previous section can be explained fairly simply. Firstly, we consider source-end contributions to be of long duration (more than one minute) even for the deep events like JAP, HK2 and the SEM. At the source end a number of wavelets are generated, the dominant ones stemming from the source per se while the others are secondary ones related to reverberations, reflections, mode conversions etc in the source region (see also Lynnes and Lay, 1989). The common denominator here is apparent velocities appropriate for teleseismic ranges. At the receiver-end, P-to-Rg conversion related to topographic relief appears to be most efficient. Naturally, the scattering areas cannot be too far away due to strong Rg attenuation - in case of NORESS Rg is seldom observed beyond 100 km for local events. Anyway, roughly the first 30 s of the coda is dominated by Rg-wavelets originating from the Bronkeberget and Skreikampen areas. The scattering 'illumination' of NORESS appear to be dependent on event azimuth and is quite weak for some events like LEE and ALA. Although the two mentioned azimuth directions dominates for most of the events, the efficiency of particular scattering sources are obviously related to the geometries involved. The

scattering is multiple in the sense that the various wavelets in the source wavetrain generate specific Rg-wavelets. Since the P-wave energy decrease with time we have a corresponding weakening of the Rg-pulses.

Further into the coda, say 30-70 s, pulses with Sg and Sn velocities become dominant. The area of potential scattering sources increases greatly, but number of significant scatters remain modest. Corresponding bearings are mainly from west to northeast, that is the most mountainous part of S. Norway, but also in the event azimuth direction. The S-wavelets are most probably generated by P-to-S scattering so their later arrivals simply reflect longer travelling distances.

In our analysis we have found very little evidence of P-to-P scattering (6-8 km/s). We take this to imply that structural heterogeneities in the crust/lithosphere are not prominent enough to act as efficient scattering sources. Even the nearby Oslo Rift with an elevated Moho of 3-5 km (Kinck et al, 1990) seemingly do not generate significant P-to-P scattering. Weak lithospheric P-scattering at depths around 100 km as reported by Troitskiy et al (1981) for NORSAR (100 km aperture) are not easily separated from source-end contributions for NORESS (only 3 km aperture). Also, why P-to-Rg, and P-to-S conversions are far more efficient than P-to-P conversions remains somewhat puzzling but these problems would be explored using 3D wavefield synthesis.

The above results and the suggested mechanism for coda generation strictly apply only to NORESS recordings at teleseismic ranges. It was rather surprising to find that about 30-50 % of the coda (Table 2) is tied to wavelets with teleseismic velocities (the coherent part) while 10-30 % appears to be scattered by rough topography in the two mentioned areas near the array. The remaining part is considered to be diffuse scattering at the receiver-end. For local and regional distances other scattering mechanisms may be more relevant since we would be dealing with horizontal travelling waves of shorter wavelengths. An other interesting observation is that Rg- propagation seems to be far more efficient, up to 300 km, in the vicinity of arrays in N. Norway (ARCESS) and Finland (FINESA) according to Toksøz et al (1990).

5.2 Conclusions

In this study we have examined teleseismic P-coda waves as recorded by the NORESS array in SE Norway in the time interval 75 s after P-onset. The essential elements in the data analysis are as follow:

- In 3C analysis the phase shift attribute (Z/R) has proved efficient in indicating where interference takes place.
- Semblance analysis and beamforming proved very valuable in estimating the slowness vector from non-P phases like Rg, Sg and Sn.
- Ideally, 3C NORESS recordings would be more useful for coda studies given additional 3C stations.

The main results obtained are as follow:

- Early P-coda at NORESS shows prominent P-to-Rg scattering from local hills with pronounced topographic relief, namely Bronkeberget (Dist~10 km, Azi~80°) and Skreikampen (Dist~30 km, Azi~225°). Rg-scattering is both forward and backward.
- P-to-S scattering is also quite efficient, continues further into the coda than Rg, but scattering locations are more obscure.
- P-to-P scattering takes place in the immediate vicinity of the array (within 4-5 s from onset) particularly to the east, but is generally weakly developed.
- Source-end scattering could not be separated from extended source pulse duration per se.
- Scattering is multiple in the sense that both the first and later P-phases from the source region result in Rg-scattering mainly from the two mentioned locations. This probably applies also to P-to-S scattering.

Acknowledgements

We appreciated the many stimulating discussions with A. Dainty and P. Troitskiy. A post-doctoral fellowship for S.C.B. from NTNF (Norwegian Technical Research Council) is gratefully acknowledged. This research is supported by the Defence Advanced Research Projects Agency under AFOSR Grant AFOSR-89-0259 monitored by the Air Force Geophysical Laboratory.

References

- Aki, K., 1973. Scattering of P-waves under the Montana LASA. *J. Geophys. Res.*, 78: 1334-1346.
- Aki, K., Christoffersson, A., and Husebye, E.S., 1977. Three-dimensional seismic structure of the lithosphere. *J. Geophys. Res.*, 82: 277-296.
- Berteussen, K.-A., Christoffersson, A., Husebye, E.S., and Dahle, A., 1975. Wave scattering theory in analysis of P-wave anomalies at NORSAR and LASA. *Geophys. J. R. astr. Soc.*, 42:403-417.
- Chernov, L.A., 1960. *Wave Propagation in Random Medium*. McGraw-Hill, New York.
- Christoffersson, A., Husebye, E.S., and Ingate, S.F., 1988. Wavefield decomposition using ML probabilities in modeling single site 3-component records. *Geophys. J. Int.*, 93: 197-213.
- Dainty, A.M. 1989. Studies of coda using array and three-component processing. *PAGEOPH*, in press.
- Dainty, A.M. and Harris, D.B., 1989. Phase velocity estimation of diffusely scattered waves. *Bull. Seism. Soc. Am.*, 79: 1231-1250.
- Flatté, S.M. and Wu, R.S., 1988. Small scale structure in the lithosphere and asthenosphere deduced from arrival time and amplitude fluctuations at Norsar. *J. Geophys. Res.*, 93: 6601-6614.
- Frankel, A., 1989. A review of numerical Experiments on seismic wave scattering. *PAGEOPH*, 131: 639-685.
- Gupta, I.N., Lynnes, C.S., Jih, R.S., and Wagner, R.A., 1989. A study of teleseismic P and P coda from U.S. and Soviet nuclear explosions. Paper presented at the 11th annual

DARPA/AFGL Seismic Research Symposium, San Antonio, Texas.

Haddon, R.A.W., and Husebye, E.S., 1978. Joint interpretation of P-wave travel time and amplitude anomalies in terms of lithospheric heterogeneities. *Geophys. J. R. astr. Soc.*, 55: 263-288.

Herraiz, M., and Espinosa, A.F., 1987. Coda waves: A review. *PAGEOPH*, 125: 499-577.

Husebye, E.S., and Ruud, B.O., 1989. Array seismology - Past, present and future developments. In: *Observatory Seismology*, Editor: Litehiser, J.J., Berkely University press.

Ingate, S.F., Husebye, E.S., and Christoffersson, A., 1985. Regional arrays and optimum processing schemes, *Bull. Seism. Soc. Am.*, 75: 1155-1177.

Jurkevics, A., 1988. Polarization analysis of three-component array data. *Bull. Seism. Soc. Am.*, 78: 1725-1743.

Kennett, B.L.N., 1987. Observational and theoretical constraints on crustal and upper mantle heterogeneity. *Phys. Earth Planet. Inter.*, 47: 319-332.

Key, F.A., 1967. Signal-generated noise recorded at the Eskdalemuir seismometer array station, *Bull. Seism. Soc. Am.*, 57: 27-37.

Kinck, J.J., Husebye, E.S. and Lund, C.-E., 1990. The S. Scandinavia Crust - Structural complexities from seismic reflection and refraction profiles. *Tectonophysics*, in press.

King, D.W., Haddon, R.A.W., and Husebye, E.S., 1975. Precursors to PP. *Physics of the Earth and Planetary Interiors*, 10: 103-127.

Korn, M., 1988. P-wave coda analysis of short-period array data and the scattering and absorptive properties of the lithosphere. *Geophysical Journal*, 93: 437-449.

Langston, C.A., 1989. Scattering of long period Rayleigh waves in western North

- America and the interpretation of coda Q measurements. *Bull.Seism.Soc.Am.*,79: 774-789.
- Lynnes, C.S. and Lay, T., 1989. Inversion of P coda for isotropic scatterers at the Yucca Flat test site. *Bull.Seism.Soc.Am.*, 79: 790-804.
- Nikolaev, A.V., and Troitskiy, P.A., 1987. Lithospheric studies based on array analysis of P-coda and microseisms. *Tectonophysics*, 140: 103-113.
- Park, J., Vernon, F.L. and Lindberg, C.R., 1987. Frequency dependent polarization analysis of high frequency seismograms. *J.Geophys.Res.*, 92: 12664-12674.
- Plesinger, A., Hellweg, M. and Seidl, D., 1986. Interactive high-resolution polarization analysis of broad-band seismograms. *J.Geophys.*, 59: 129-139.
- Roberts, R.G., and Christofferson, A., 1990. Decomposition of complex single-station 3-component seismograms. *Geophys. J. Int.*, in press.
- Toksöz, M.N., Dainty, A.M., and Charrette, E.E., 1990. Coherency of ground motion at regional distances and scattering, *Phys. Earth Planet. Inter.*, in press.
- Troitskiy, P., Husebye, E.S., and Nikolaev, A., 1981. Lithospheric studies based on holographic principles. *Nature* 294: 618-623.
- Vidale, J.E., 1986. Complex polarization analysis of particle motion. *Bull. Seism. Soc. Am.*, 76: 1393-1405.
- Ward, S.N., 1978. Long period reflected and converted upper-mantle phases. *Bull. Seism. Soc. Am.*, 68: 133-153.
- Wu, R-S. and Aki, K., 1988. Introduction: Seismic wave scattering in three-dimensionally heterogeneous earth. In: Wu, R-S., and Aki, K. (eds.). *Scattering and attenuation of seismic waves*, *PAGEOPH*, 128: 1-6.

Table captions.

Table 1: Hypocenter parameters of the events analyzed (from ISC and PDE catalogues); distances and azimuths (in degrees) are calculated relative to the NORESS array. Event regions are: KAM - Kamchatka, JAP - Japan (south of Honshu), SEM - Semipalatinsk (East Kazakh), HK1 and HK2 - Hindu Kush, MAD - NW of Madagascar, LEE - Leeward Island, ALA - Alaska.

Table 2: Shown numbers are percentages of coherent power on the teleseismic beam for different time intervals. Coherent power is calculated as the energy on the beam divided by the average energy of the single channel sensors for the same time interval. Data used are from the A0, C- and D-ring instruments and were filtered in the 1-3 Hz passband. The beam steering directions were those giving the highest coherency in the first 3 s of the signal.

Figure captions.

Fig. 1. The general NORESS array area with scattering locations hatched. The arrows gives the direction of approach of the events analyzed (Table 1). The array configuration is given in the lower right insert where encircled stations indicate 3-component sites.

Fig. 2a. Results from 3-component analysis of the first 4 events in Table 1: Each event is shown in a compartment box of 4 sections, namely:

- i) The 3C seismic traces, rotated into a vertical-radial-tangential (Z,R,T) coordinate system.
- ii) ML probabilities exceeding 0.50 of a P-wave polarization. For all events the sliding window was 1.6s long, incremented in 0.2s in time and 4° in azimuth.
- iii) The phase difference between the radial (R) and vertical (Z) components. The particle motion is pure P, elliptical or pure SV for phase differences of 180° , $\pm 90^\circ$ and 0° , respectively. For cases where the arriving wavelets are not approximately in the radial plane, the phase difference estimate would be unreliable.
- iv) Apparent 3C-velocities including error bars as calculated from angle of incidence estimates.

Fig. 2b. Results from 3-component (3C) analysis of the last 4 events in Table 1. Otherwise caption as in Fig. 2a.

Fig. 3. RMS amplitudes (counts) for average single channel and beam traces for the events analyzed (Table 1). The traces from the A0, C- and D-ring sensors were bandpass filtered 1-3 Hz prior to RMS calculations in a 4 s window. The upper traces are the average single channel amplitudes while the beam amplitudes are shown with shading.

Fig. 4. Outcome of residual trace semblance analysis aimed at identifying Rg-wavelets in the coda. Semblance is shown as a function time and azimuth for a fixed phase velocity of 3.0 km/s. The calculation of residual traces are explained in the text. All traces were filtered in the 1-3 Hz passband and semblance calculations are for a 1.5 s window. The semblance contouring levels start at 0.25 and increase in steps of 0.05. The thin horizontal lines mark azimuths of 80° and 225° , while the thin vertical lines indicate P-onset time.

Fig. 5. Examples of waveforms estimated through beamforming. For each event the 'best' teleseismic beam is shown first followed by Rg waveforms estimated by residual trace beamforming aimed at the two scattering areas. All traces were filter in the 1-3 Hz passband.

Fig. 6. Coda semblance analysis aimed at identifying Rg-wavelets in a 40 sec time segment after that in Fig. 4. The thin horizontal lines mark azimuths of 80° and 225° , while the thin vertical lines indicate 40 s after P-onset time. Caption otherwise as in Fig. 4.

Fig. 7. Coda semblance analysis aimed at identifying Sn-wavelets for the same time segment as in Fig. 6. The fixed phase velocity is here 4.5 km/s - caption otherwise as in Fig. 6. In cases where semblance contours coincide with those in Fig. 6, the true phase velocity is probably of the intermediate Sg-type, that is ca 3.6 km/s.

Event	Date	Origin-time	Lat.	Long.	Dist.	Azi.	Dep.	Mb/Ms
KAM	11 Jan 88	21:07:29.7	54.78N	161.66E	62.1	19.0	43	5.8/4.9
JAP	12 Dec 87	04:51:50.5	29.69N	140.02E	80.3	43.6	164	6.3/ -
SEM	14 Sep 88	04:00:00.0	49.87N	78.82E	37.9	75.2	0	6.0/4.5
HK1	29 Jul 85	07:54:44.5	36.21N	70.90E	44.2	95.7	102	6.5/ -
HK2	7 May 86	23:25:25.9	36.37N	70.71E	44.0	95.8	223	5.6/ -
MAD	14 May 85	13:25:01.2	10.72S	41.26E	75.2	149.8	37	5.8/5.6
LEE	16 Mar 85	14:54:43.7	16.98N	62.46W	67.4	264.6	20	6.1/6.4
ALA	6 Mar 88	22:35:38.1	56.95N	143.03W	60.6	344.4	10	6.8/7.6

Table: 1

Event	Time after P onset (s):			
	0-5	5-10	10-35	35-75
KAM	94	63	44	44
JAP	94	67	34	21
SEM	96	63	45	42
HK1	92	90	63	43
HK2	92	52	26	28
MAD	97	84	75	26
LEE	98	95	90	71
ALA	93	94	61	45

Table: 2

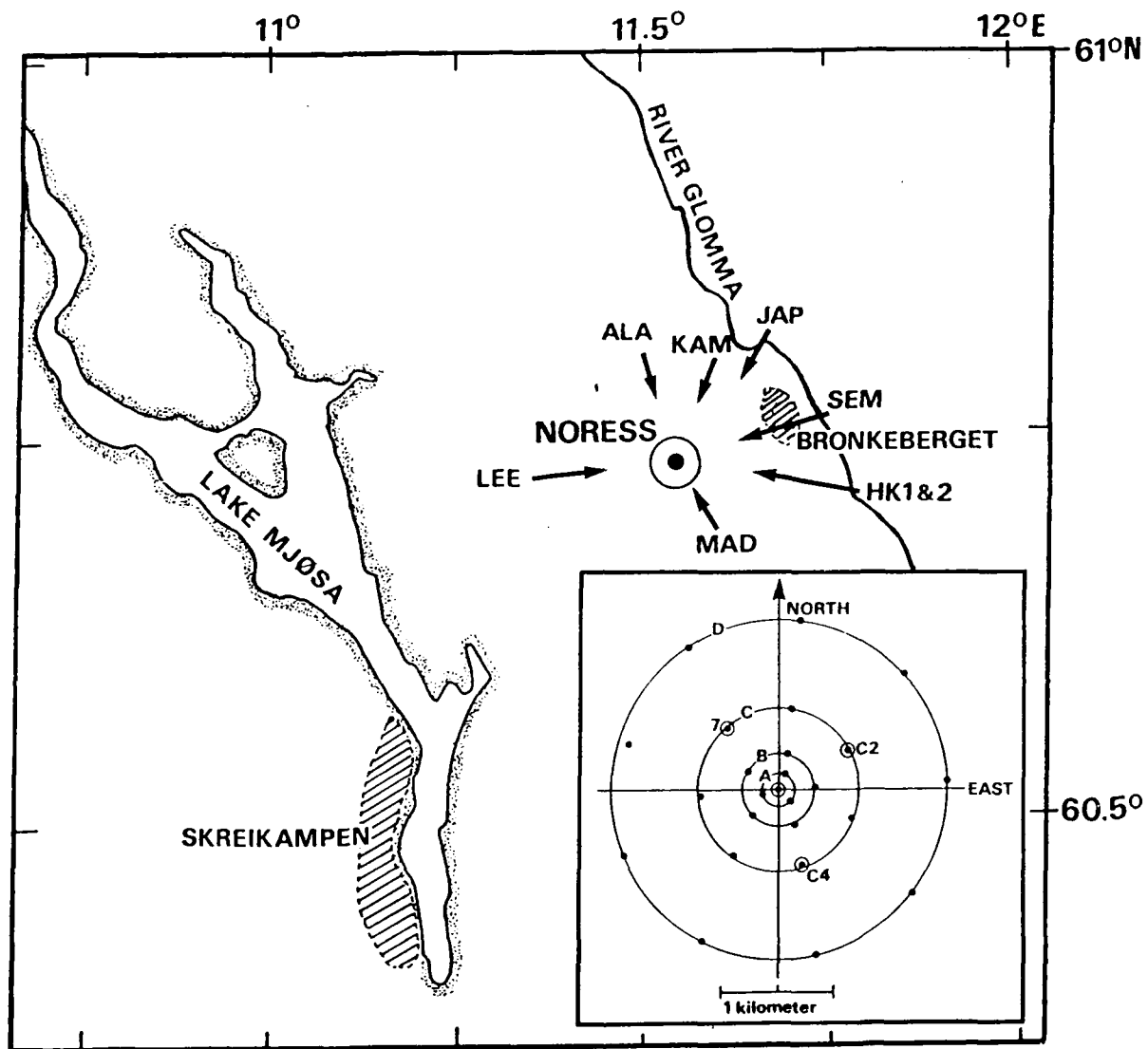


Fig. 1:

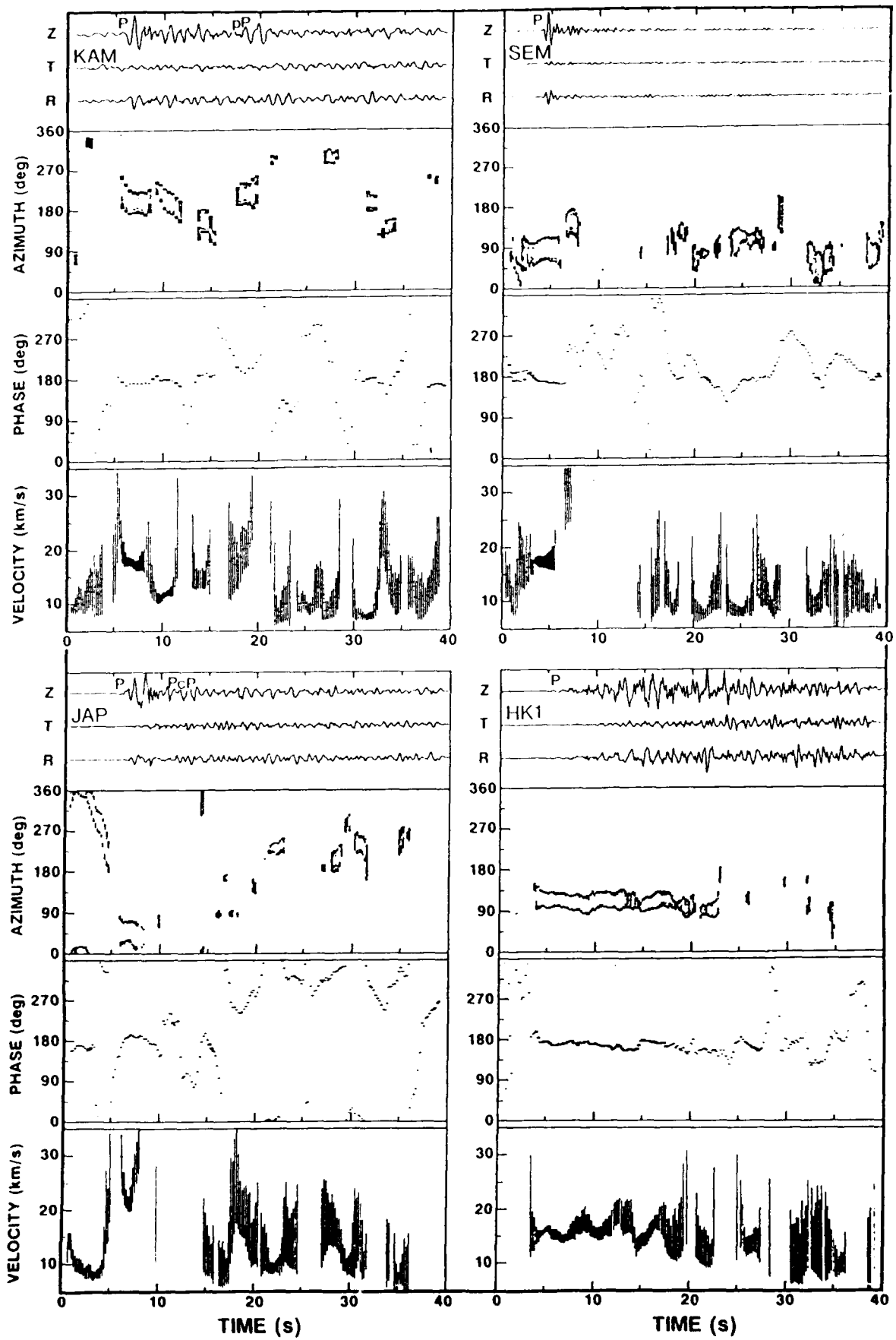


Fig.2a:

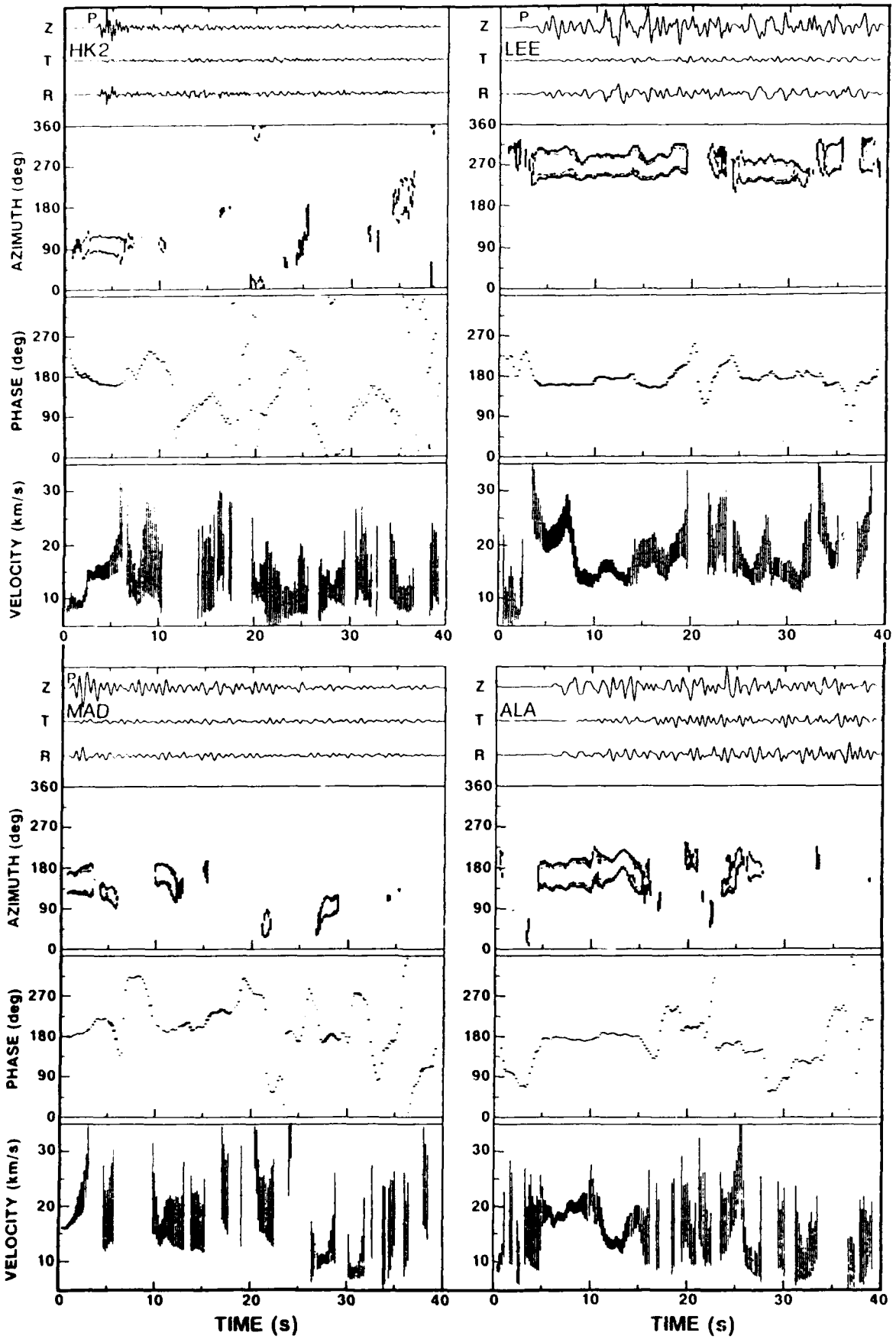


Fig.2b:

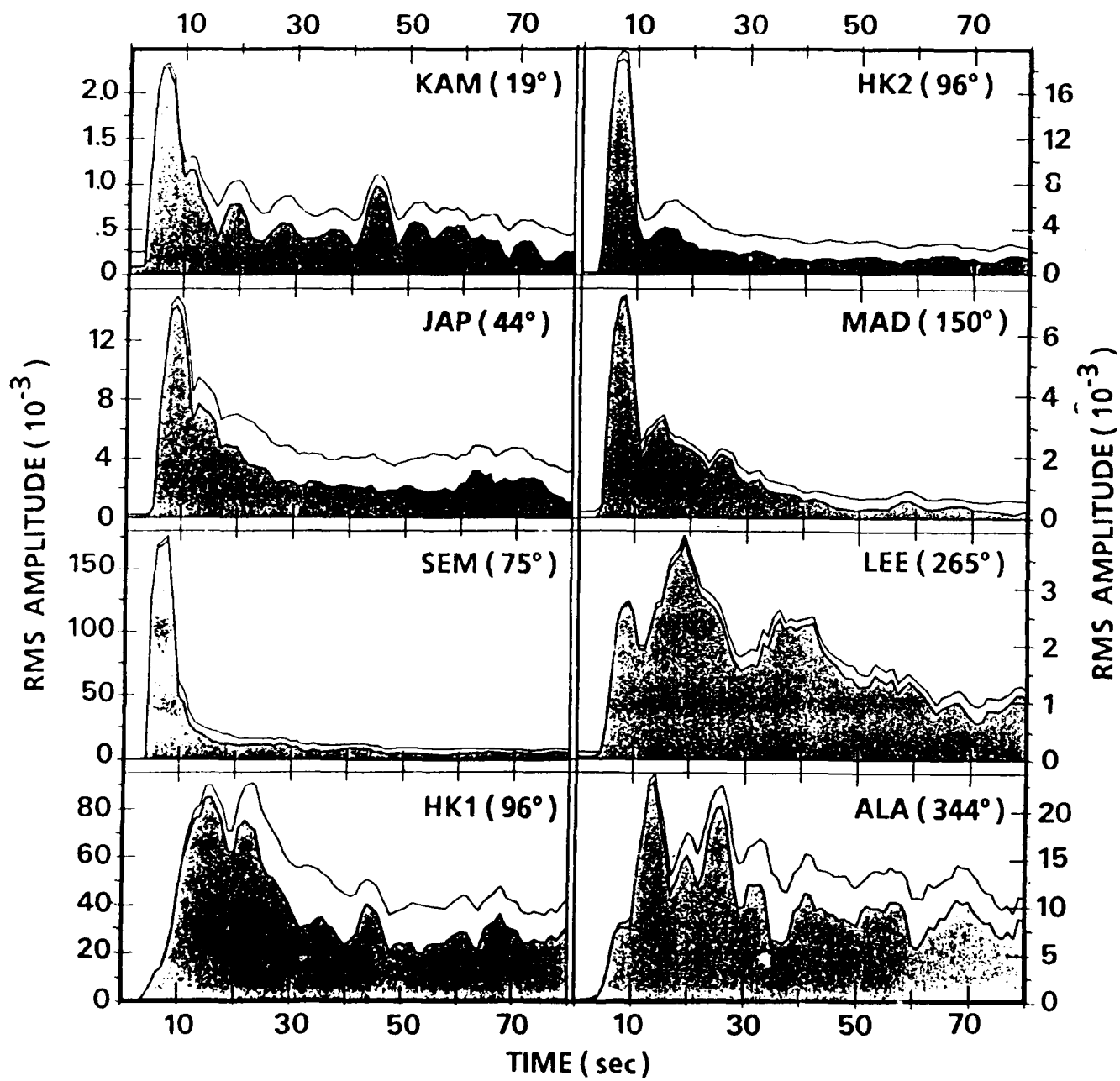


Fig.3:

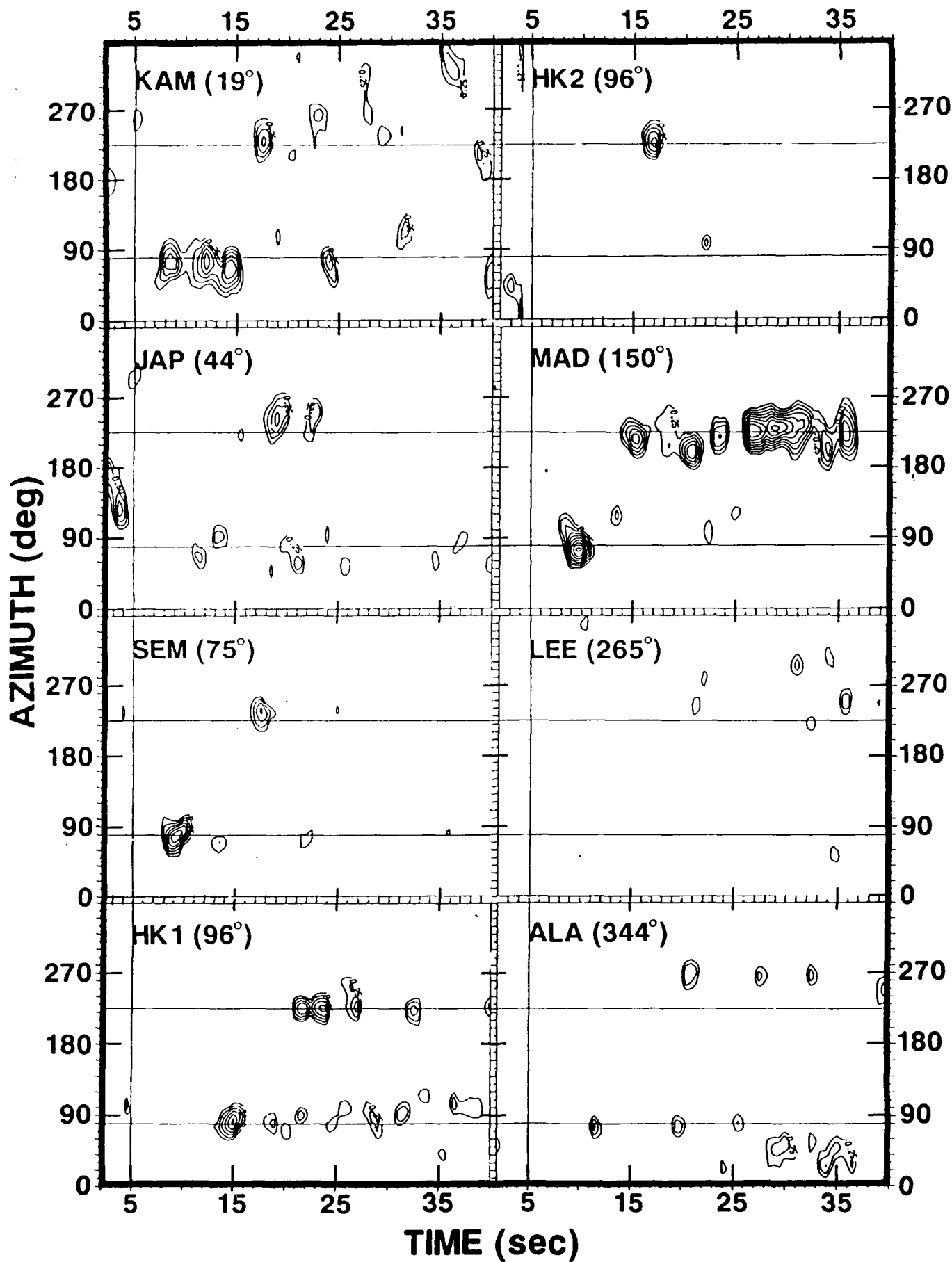


Fig.4:

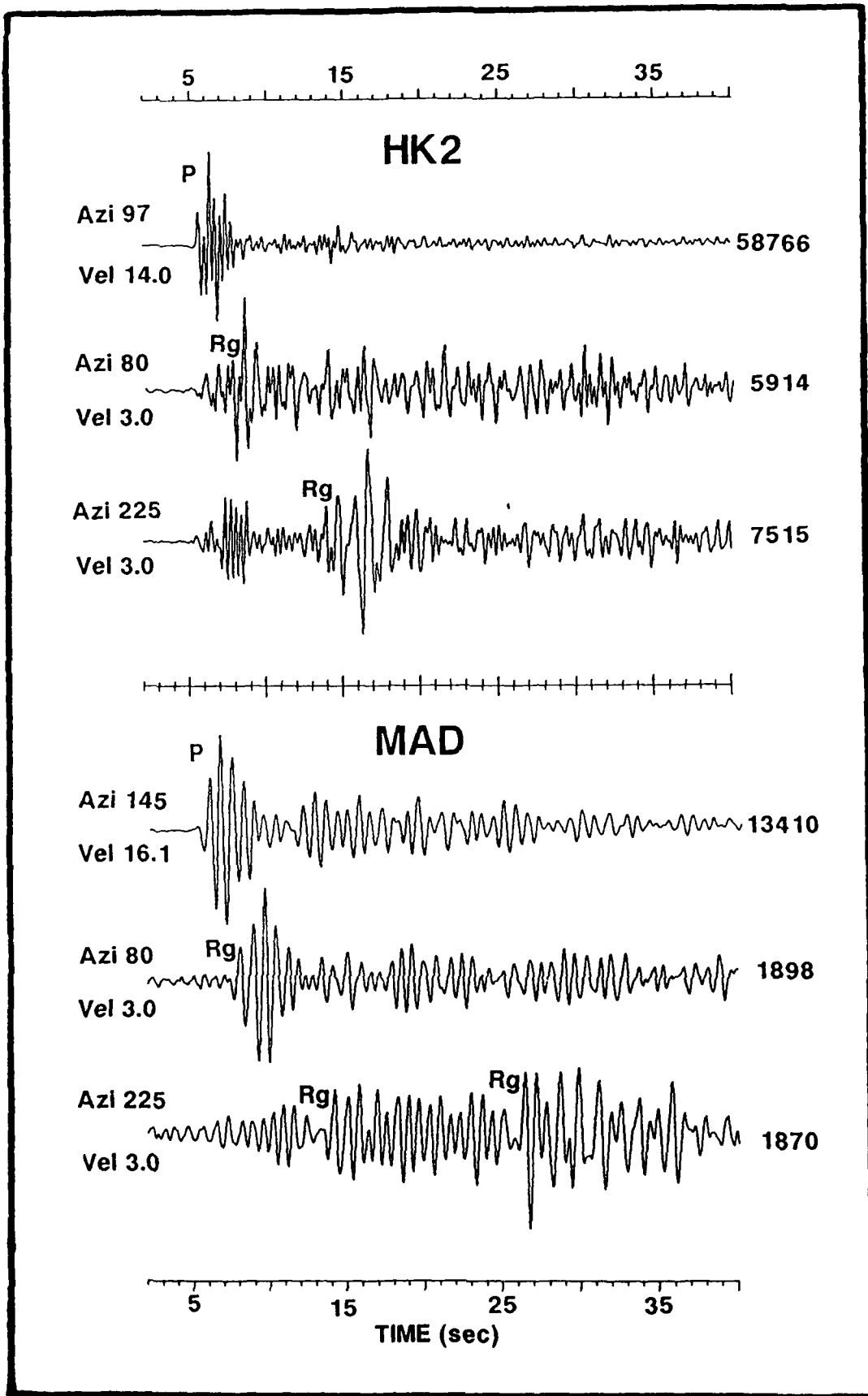


Fig.5:

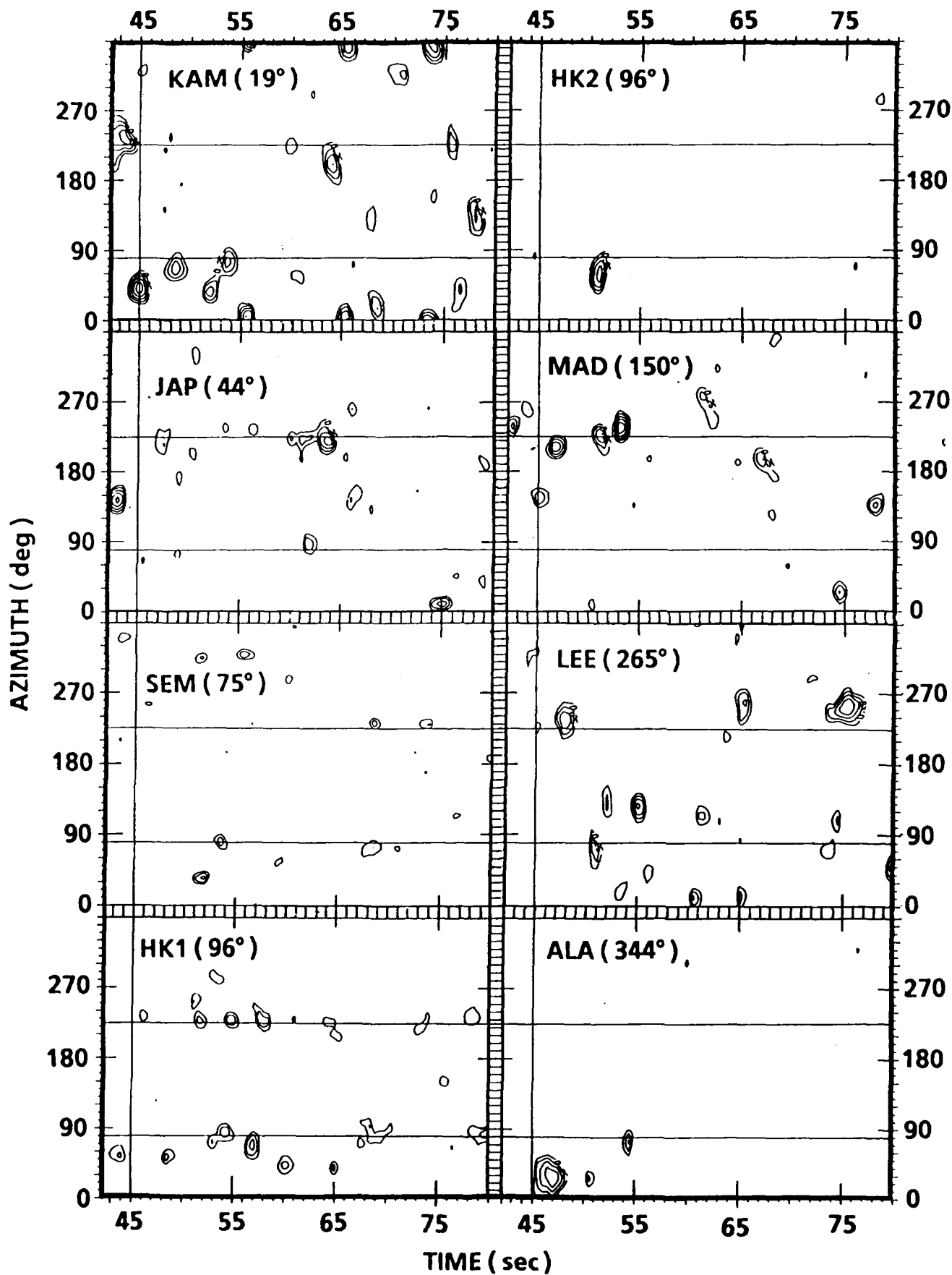


Fig.6:

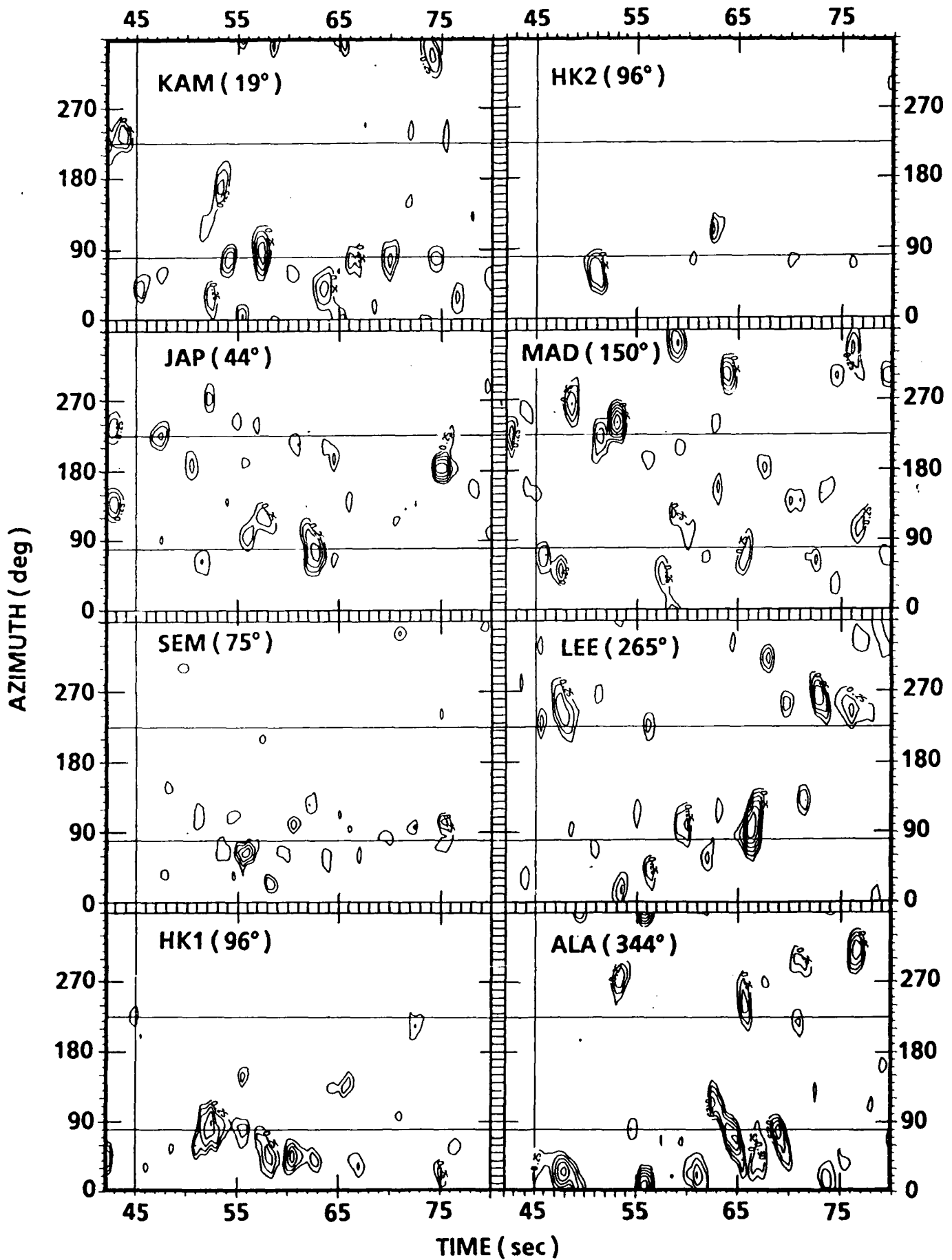


Fig.7:

RESEARCH IMPLICATIONS - FUTURE WORK

We are a bit excited about the new scattering results (Sec.4) and have already taken the first steps towards similar studies for the ARCESS (N Norway) and FINESA (Finland) arrays. A far more difficult study now being considered, namely to compute the response of the NORESS scattering 'hills' on the P-wave recordings using finite element techniques.

The NORESS and ARCESS arrays are equipped with four 3C stations, and we plan to undertake a development of techniques for joint processing of multichannel 3C records. The rationale here is to extract information about wavetype being dominant on the horizontal components. We would continue the work on 3C signal detection where preliminary results so far are promising. For example, for a time span of 16 hours a single 3C station within NORESS (C4) detected 24 local/regional events of which 21 were 'shared' by the array itself. The 3C detector now being tested, operates on low thresholds so a relative large set of rules are being established for eliminating false detections and besides associate secondary coda-detections into event families.

Finally, some of the above research work is undertaken jointly with visiting scientists and colleagues in Norway, Sweden and Finland.

Contractors (United States)

Prof. Thomas Ahrens
Seismological Lab, 252-21
Division of Geological & Planetary Sciences
California Institute of Technology
Pasadena, CA 91125

Prof. Charles B. Archambeau
CIRES
University of Colorado
Boulder, CO 80309

Prof. Muawia Barazangi
Institute for the Study of the Continent
Cornell University
Ithaca, NY 14853

Dr. Douglas R. Baumgardt
ENSCO, Inc
5400 Port Royal Road
Springfield, VA 22151-2388

Prof. Jonathan Berger
IGPP, A-025
Scripps Institution of Oceanography
University of California, San Diego
La Jolla, CA 92093

Dr. Lawrence J. Burdick
Woodward-Clyde Consultants
566 El Dorado Street
Pasadena, CA 91109-3245

Dr. Karl Coyner
New England Research, Inc.
76 Olcott Drive
White River Junction, VT 05001

Prof. Vernon F. Cormier
Department of Geology & Geophysics
U-45, Room 207
The University of Connecticut
Storrs, CT 06268

Professor Anton W. Dainty
Earth Resources Laboratory
Massachusetts Institute of Technology
42 Carleton Street
Cambridge, MA 02142

Prof. Steven Day
Department of Geological Sciences
San Diego State University
San Diego, CA 92182

Dr. Zoltan A. Der
ENSCO, Inc.
5400 Port Royal Road
Springfield, VA 22151-2388

Prof. John Ferguson
Center for Lithospheric Studies
The University of Texas at Dallas
P.O. Box 830688
Richardson, TX 75083-0688

Prof. Stanley Flatte
Applied Sciences Building
University of California
Santa Cruz, CA 95064

Dr. Alexander Florence
SRI International
333 Ravenswood Avenue
Menlo Park, CA 94025-3493

Prof. Henry L. Gray
Vice Provost and Dean
Department of Statistical Sciences
Southern Methodist University
Dallas, TX 75275

Dr. Indra Gupta
Teledyne Geotec
314 Montgomery Street
Alexandria, VA 22314

Prof. David G. Harkrider
Seismological Laboratory
Division of Geological & Planetary Sciences
California Institute of Technology
Pasadena, CA 91125

Prof. Donald V. Helmberger
Seismological Laboratory
Division of Geological & Planetary Sciences
California Institute of Technology
Pasadena, CA 91125

Prof. Eugene Herrin
Institute for the Study of Earth and Man
Geophysical Laboratory
Southern Methodist University
Dallas, TX 75275

Prof. Robert B. Herrmann
Department of Earth & Atmospheric Sciences
St. Louis University
St. Louis, MO 63156

Prof. Bryan Isacks
Cornell University
Department of Geological Sciences
SNEE Hall
Ithaca, NY 14850

Dr. Rong-Song Jih
Teledyne Geotech
314 Montgomery Street
Alexandria, VA 22314

Prof. Lane R. Johnson
Seismographic Station
University of California
Berkeley, CA 94720

Prof. Alan Kafka
Department of Geology & Geophysics
Boston College
Chestnut Hill, MA 02167

Dr. Richard LaCoss
MIT-Lincoln Laboratory
M-200B
P. O. Box 73
Lexington, MA 02173-0073 (3 copies)

Prof Fred K. Lamb
University of Illinois at Urbana-Champaign
Department of Physics
1110 West Green Street
Urbana, IL 61801

Prof. Charles A. Langston
Geosciences Department
403 Deike Building
The Pennsylvania State University
University Park, PA 16802

Prof. Thorne Lay
Institute of Tectonics
Earth Science Board
University of California, Santa Cruz
Santa Cruz, CA 95064

Prof. Arthur Lerner-Lam
Lamont-Doherty Geological Observatory
of Columbia University
Palisades, NY 10964

Dr. Christopher Lynnes
Teledyne Geotech
314 Montgomery Street
Alexandria, VA 22314

Prof. Peter Malin
University of California at Santa Barbara
Institute for Crustal Studies
Santa Barbara, CA 93106

Dr. Randolph Martin, III
New England Research, Inc.
76 Olcott Drive
White River Junction, VT 05001

Dr. Gary McCartor
Mission Research Corporation
735 State Street
P.O. Drawer 719
Santa Barbara, CA 93102 (2 copies)

Prof. Thomas V. McEvelly
Seismographic Station
University of California
Berkeley, CA 94720

Dr. Keith L. McLaughlin
S-CUBED
A Division of Maxwell Laboratory
P.O. Box 1620
La Jolla, CA 92038-1620

Prof. William Menke
Lamont-Doherty Geological Observatory
of Columbia University
Palisades, NY 10964

Stephen Miller
SRI International
333 Ravenswood Avenue
Box AF 116
Menlo Park, CA 94025-3493

Prof. Bernard Minster
IGPP, A-025
Scripps Institute of Oceanography
University of California, San Diego
La Jolla, CA 92093

Prof. Brian J. Mitchell
Department of Earth & Atmospheric Sciences
St. Louis University
St. Louis, MO 63156

Mr. Jack Murphy
S-CUBED, A Division of Maxwell Laboratory
11800 Sunrise Valley Drive
Suite 1212
Reston, VA 22091 (2 copies)

Dr. Bao Nguyen
GL/LWH
Hanscom AFB, MA 01731-5000

Prof. John A. Orcutt
IGPP, A-025
Scripps Institute of Oceanography
University of California, San Diego
La Jolla, CA 92093

Prof. Keith Priestley
University of Cambridge
Bullard Labs, Dept. of Earth Sciences
Madingley Rise, Madingley Rd.
Cambridge CB3 0EZ, ENGLAND

Prof. Paul G. Richards
L-210
Lawrence Livermore National Laboratory
Livermore, CA 94550

Dr. Wilmer Rivers
Teledyne Geotech
314 Montgomery Street
Alexandria, VA 22314

Prof. Charles G. Sammis
Center for Earth Sciences
University of Southern California
University Park
Los Angeles, CA 90089-0741

Prof. Christopher H. Scholz
Lamont-Doherty Geological Observatory
of Columbia University
Palisades, NY 10964

Prof. David G. Simpson
Lamont-Doherty Geological Observatory
of Columbia University
Palisades, NY 10964

Dr. Jeffrey Stevens
S-CUBED
A Division of Maxwell Laboratory
P.O. Box 1620
La Jolla, CA 92038-1620

Prof. Brian Stump
Institute for the Study of Earth & Man
Geophysical Laboratory
Southern Methodist University
Dallas, TX 75275

Prof. Jeremiah Sullivan
University of Illinois at Urbana-Champaign
Department of Physics
1110 West Green Street
Urbana, IL 61801

Prof. Clifford Thurber
University of Wisconsin-Madison
Department of Geology & Geophysics
1215 West Dayton Street
Madison, WI 53706

Prof. M. Nafi Toksoz
Earth Resources Lab
Massachusetts Institute of Technology
42 Carleton Street
Cambridge, MA 02142

Prof. John E. Vidale
University of California at Santa Cruz
Seismological Laboratory
Santa Cruz, CA 95064

Prof. Terry C. Wallace
Department of Geosciences
Building #77
University of Arizona
Tucson, AZ 85721

Dr. Raymond Willeman
GL/LWH
Hanscom AFB, MA 01731-5000

Dr. Lorraine Wolf
GL/LWH
Hanscom AFB, MA 01731-5000

Prof. Francis T. Wu
Department of Geological Sciences
State University of New York
at Binghamton
Vestal, NY 13901

OTHERS (United States)

Dr. Monem Abdel-Gawad
Rockwell International Science Center
1049 Camino Dos Rios
Thousand Oaks, CA 91360

Prof. Keiiti Aki
Center for Earth Sciences
University of Southern California
University Park
Los Angeles, CA 90089-0741

Prof. Shelton S. Alexander
Geosciences Department
403 Deike Building
The Pennsylvania State University
University Park, PA 16802

Dr. Kenneth Anderson
BBNSTC
Mail Stop 14/1B
Cambridge, MA 02238

Dr. Ralph Archuleta
Department of Geological Sciences
University of California at Santa Barbara
Santa Barbara, CA 93102

Dr. Thomas C. Bache, Jr.
Science Applications Int'l Corp.
10210 Campus Point Drive
San Diego, CA 92121 (2 copies)

J. Barker
Department of Geological Sciences
State University of New York
at Binghamton
Vestal, NY 13901

Dr. T.J. Bennett
S-CUBED
A Division of Maxwell Laboratory
11800 Sunrise Valley Drive, Suite 1212
Reston, VA 22091

Mr. William J. Best
907 Westwood Drive
Vienna, VA 22180

Dr. N. Biswas
Geophysical Institute
University of Alaska
Fairbanks, AK 99701

Dr. G.A. Bollinger
Department of Geological Sciences
Virginia Polytechnical Institute
21044 Derring Hall
Blacksburg, VA 24061

Dr. Stephen Bratt
Science Applications Int'l Corp.
10210 Campus Point Drive
San Diego, CA 92121

Michael Browne
Teledyne Geotech
3401 Shiloh Road
Garland, TX 75041

Mr. Roy Burger
1221 Serry Road
Schenectady, NY 12309

Dr. Robert Burrige
Schlumberger-Doll Research Center
Old Quarry Road
Ridgefield, CT 06877

Dr. Jerry Carter
Rondout Associates
P.O. Box 224
Stone Ridge, NY 12484

Dr. W. Winston Chan
Teledyne Geotech
314 Montgomery Street
Alexandria, VA 22314-1581

Dr. Theodore Cherry
Science Horizons, Inc.
710 Encinitas Blvd., Suite 200
Encinitas, CA 92024 (2 copies)

Prof. Jon F. Claerbout
Department of Geophysics
Stanford University
Stanford, CA 94305

Prof. Robert W. Clayton
Seismological Laboratory
Division of Geological & Planetary Sciences
California Institute of Technology
Pasadena, CA 91125

Prof. F. A. Dahlen
Geological and Geophysical Sciences
Princeton University
Princeton, NJ 08544-0636

Prof. Adam Dziewonski
Hoffman Laboratory
Harvard University
20 Oxford St
Cambridge, MA 02138

Prof. John Ebel
Department of Geology & Geophysics
Boston College
Chestnut Hill, MA 02167

Eric Fielding
SNEE Hall
INSTOC
Cornell University
Ithaca, NY 14853

Prof. Donald Forsyth
Department of Geological Sciences
Brown University
Providence, RI 02912

Dr. Cliff Frolich
Institute of Geophysics
8701 North Mopac
Austin, TX 78759

Prof. Art Frankel
Mail Stop 922
Geological Survey
790 National Center
Reston, VA 22092

Dr. Anthony Gangi
Texas A&M University
Department of Geophysics
College Station, TX 77843

Dr. Freeman Gilbert
Inst. of Geophysics & Planetary Physics
University of California, San Diego
P.O. Box 109
La Jolla, CA 92037

Mr. Edward Giller
Pacific Sierra Research Corp.
1401 Wilson Boulevard
Arlington, VA 22209

Dr. Jeffrey W. Given
Sierra Geophysics
11255 Kirkland Way
Kirkland, WA 98033

Prof. Stephen Grand
University of Texas at Austin
Department of Geological Sciences
Austin, TX 78713-7909

Prof. Roy Greenfield
Geosciences Department
403 Deike Building
The Pennsylvania State University
University Park, PA 16802

Dan N. Hagedorn
Battelle
Pacific Northwest Laboratories
Battelle Boulevard
Richland, WA 99352

Kevin Hutchenson
Department of Earth Sciences
St. Louis University
3507 Laclede
St. Louis, MO 63103

Prof. Thomas H. Jordan
Department of Earth, Atmospheric
and Planetary Sciences
Massachusetts Institute of Technology
Cambridge, MA 02139

Robert C. Kemerait
ENSCO, Inc.
445 Pineda Court
Melbourne, FL 32940

William Kikendall
Teledyne Geotech
3401 Shiloh Road
Garland, TX 75041

Prof. Leon Knopoff
University of California
Institute of Geophysics & Planetary Physics
Los Angeles, CA 90024

Prof. L. Timothy Long
School of Geophysical Sciences
Georgia Institute of Technology
Atlanta, GA 30332

Prof. Art McGarr
Mail Stop 977
Geological Survey
345 Middlefield Rd.
Menlo Park, CA 94025

Dr. George Mellman
Sierra Geophysics
11255 Kirkland Way
Kirkland, WA 98033

Prof. John Nabelek
College of Oceanography
Oregon State University
Corvallis, OR 97331

Prof. Geza Nagy
University of California, San Diego
Department of Ames, M.S. B-010
La Jolla, CA 92093

Prof. Amos Nur
Department of Geophysics
Stanford University
Stanford, CA 94305

Prof. Jack Oliver
Department of Geology
Cornell University
Ithaca, NY 14850

Prof. Robert Phinney
Geological & Geophysical Sciences
Princeton University
Princeton, NJ 08544-0636

Dr. Paul Pomeroy
Rondout Associates
P.O. Box 224
Stone Ridge, NY 12484

Dr. Jay Pulli
RADIX System, Inc.
2 Taft Court, Suite 203
Rockville, MD 20850

Dr. Norton Rimer
S-CUBED
A Division of Maxwell Laboratory
P.O. Box 1620
La Jolla, CA 92038-1620

Prof. Larry J. Ruff
Department of Geological Sciences
1006 C.C. Little Building
University of Michigan
Ann Arbor, MI 48109-1063

Dr. Richard Sailor
TASC Inc.
55 Walkers Brook Drive
Reading, MA 01867

Thomas J. Sereno, Jr.
Science Application Int'l Corp.
10210 Campus Point Drive
San Diego, CA 92121

John Sherwin
Teledyne Geotech
3401 Shiloh Road
Garland, TX 75041

Prof. Robert Smith
Department of Geophysics
University of Utah
1400 East 2nd South
Salt Lake City, UT 84112

Prof. S. W. Smith
Geophysics Program
University of Washington
Seattle, WA 98195

Dr. Stewart Smith
IRIS Inc.
1616 North Fort Myer Drive
Suite 1440
Arlington, VA 22209

Dr. George Sutton
Rondout Associates
P.O. Box 224
Stone Ridge, NY 12484

Prof. L. Sykes
Lamont-Doherty Geological Observatory
of Columbia University
Palisades, NY 10964

Prof. Pradeep Talwani
Department of Geological Sciences
University of South Carolina
Columbia, SC 29208

Prof. Ta-liang Teng
Center for Earth Sciences
University of Southern California
University Park
Los Angeles, CA 90089-0741

Dr. R.B. Tittmann
Rockwell International Science Center
1049 Camino Dos Rios
P.O. Box 1085
Thousand Oaks, CA 91360

Dr. Gregory van der Vink
IRIS, Inc.
1616 North Fort Myer Drive
Suite 1440
Arlington, VA 22209

Professor Daniel Walker
University of Hawaii
Institute of Geophysics
Honolulu, HI 96822

William R. Walter
Seismological Laboratory
University of Nevada
Reno, NV 89557

Dr. Gregory Wojcik
Weidlinger Associates
4410 El Camino Real
Suite 110
Los Altos, CA 94022

Prof. John H. Woodhouse
Hoffman Laboratory
Harvard University
20 Oxford St.
Cambridge, MA 02138

Dr. Gregory B. Young
ENSCO, Inc.
5400 Port Royal Road
Springfield, VA 22151-2388

GOVERNMENT

Dr. Ralph Alewine III
DARPA/NMRO
1400 Wilson Boulevard
Arlington, VA 22209-2308

Mr. James C. Battis
GL/LWH
Hanscom AFB, MA 01731-5000

Dr. Robert Blandford
DARPA/NMRO
1400 Wilson Boulevard
Arlington, VA 22209-2308

Eric Chael
Division 9241
Sandia Laboratory
Albuquerque, NM 87185

Dr. John J. Cipar
GL/LWH
Hanscom AFB, MA 01731-5000

Mr. Jeff Duncan
Office of Congressman Markey
2133 Rayburn House Bldg.
Washington, DC 20515

Dr. Jack Evernden
USGS - Earthquake Studies
345 Middlefield Road
Menlo Park, CA 94025

Art Frankel
USGS
922 National Center
Reston, VA 22092

Dr. T. Hanks
USGS
Nat'l Earthquake Research Center
345 Middlefield Road
Menlo Park, CA 94025

Dr. James Hannon
Lawrence Livermore Nat'l Laboratory
P.O. Box 808
Livermore, CA 94550

Paul Johnson
ESS-4, Mail Stop J979
Los Alamos National Laboratory
Los Alamos, NM 87545

Janet Johnston
GL/LWH
Hanscom AFB, MA 01731-5000

Dr. Katharine Kadinsky-Cade
GL/LWH
Hanscom AFB, MA 01731-5000

Ms. Ann Kerr
IGPP, A-025
Scripps Institute of Oceanography
University of California, San Diego
La Jolla, CA 92093

Dr. Max Koontz
US Dept of Energy/DP 5
Forrestal Building
1000 Independence Avenue
Washington, DC 20585

Dr. W.H.K. Lee
Office of Earthquakes, Volcanoes,
& Engineering
345 Middlefield Road
Menlo Park, CA 94025

Dr. William Leith
U.S. Geological Survey
Mail Stop 928
Reston, VA 22092

Dr. Richard Lewis
Director, Earthquake Engineering & Geophysics
U.S. Army Corps of Engineers
Box 631
Vicksburg, MS 39180

James F. Lewkowicz
GL/LWH
Hanscom AFB, MA 01731-5000

Mr. Alfred Lieberman
ACDA/VI-OA'State Department Bldg
Room: 5726
320 - 21st Street, NW
Washington, DC 20451

Stephen Mangino
GL/LWH
Hanscom AFB, MA 01731-5000

Dr. Frank F. Pilotte
HQ AFTAC/TT
Patrick AFB, FL 32925-6001

Dr. Robert Masse
Box 25046, Mail Stop 967
Denver Federal Center
Denver, CO 80225

Katie Poley
CIA-OSWR/NED
Washington, DC 20505

Art McGarr
U.S. Geological Survey, MS-977
345 Middlefield Road
Menlo Park, CA 94025

Mr. Jack Rachlin
U.S. Geological Survey
Geology, Rm 3 C136
Mail Stop 928 National Center
Reston, VA 22092

Richard Morrow
ACDA/VI, Room 5741
320 21st Street N.W.
Washington, DC 20451

Dr. Robert Reinke
WL/NTESG
Kirtland AFB, NM 87117-6008

Dr. Keith K. Nakanishi
Lawrence Livermore National Laboratory
P.O. Box 808, L-205
Livermore, CA 94550

Dr. Byron Ristvet
HQ DNA, Nevada Operations Office
Attn: NVCG
P.O. Box 98539
Las Vegas, NV 89193

Dr. Carl Newton
Los Alamos National Laboratory
P.O. Box 1663
Mail Stop C335, Group ESS-3
Los Alamos, NM 87545

Dr. George Rothe
HQ AFTAC/TGR
Patrick AFB, FL 32925-6001

Dr. Kenneth H. Olsen
Los Alamos Scientific Laboratory
P.O. Box 1663
Mail Stop C335, Group ESS-3
Los Alamos, NM 87545

Dr. Alan S. Ryall, Jr.
DARPA/NMRO
1400 Wilson Boulevard
Arlington, VA 22209-2308

Howard J. Patton
Lawrence Livermore National Laboratory
P.O. Box 808, L-205
Livermore, CA 94550

Dr. Michael Shore
Defense Nuclear Agency/SPSS
6801 Telegraph Road
Alexandria, VA 22310

Mr. Chris Paine
Office of Senator Kennedy
SR 315
United States Senate
Washington, DC 20510

Donald L. Springer
Lawrence Livermore National Laboratory
P.O. Box 808, L-205
Livermore, CA 94550

Colonel Jerry J. Perrizo
AFOSR/NP, Building 410
Bolling AFB
Washington, DC 20332-6448

Mr. Charles L. Taylor
GL/LWG
Hanscom AFB, MA 01731-5000

Dr. Thomas Weaver
Los Alamos National Laboratory
P.O. Box 1663, Mail Stop C335
Los Alamos, NM 87545

DARPA/PM
1400 Wilson Boulevard
Arlington, VA 22209

J.J. Zucca
Lawrence Livermore National Laboratory
Box 808
Livermore, CA 94550

Defense Technical Information Center
Cameron Station
Alexandria, VA 22314 (5 copies)

GL/SULL
Research Library
Hanscom AFB, MA 01731-5000 (2 copies)

Defense Intelligence Agency
Directorate for Scientific &
Technical Intelligence
Washington, DC 20301

Secretary of the Air Force
(SAFRD)

AFTAC/CA
(STINFO)
Patrick AFB, FL 32925-6001

Washington, DC 20330

Office of the Secretary Defense
DDR & E
Washington, DC 20330

TACTEC
Battelle Memorial Institute
505 King Avenue
Columbus, OH 43201 (Final Report Only)

HQ DNA
Attn: Technical Library
Washington, DC 20305

DARPA/RMO/RETRIEVAL
1400 Wilson Boulevard
Arlington, VA 22209

DARPA/RMO/Security Office
1400 Wilson Boulevard
Arlington, VA 22209

Geophysics Laboratory
Attn: XJ
Hanscom AFB, MA 01731-5000

Geophysics Laboratory
Attn: LW
Hanscom AFB, MA 01731-5000

CONTRACTORS (Foreign)

Dr. Ramon Cabre, S.J.
Observatorio San Calixto
Casilla 5939
La Paz, Bolivia

Prof. Hans-Peter Harjes
Institute for Geophysik
Ruhr University/Bochum
P.O. Box 102148
4630 Bochum 1, FRG

Prof. Eystein Husebye
NTNF/NORSAR
P.O. Box 51
N-2007 Kjeller, NORWAY

Prof. Brian L.N. Kennett
Research School of Earth Sciences
Institute of Advanced Studies
G.P.O. Box 4
Canberra 2601, AUSTRALIA

Dr. Bernard Massinon
Societe Radiomana
27 rue Claude Bernard
75005 Paris, FRANCE (2 Copies)

Dr. Pierre Mecheler
Societe Radiomana
27 rue Claude Bernard
75005 Paris, FRANCE

Dr. Svein Mykkeltveit
NTNF/NORSAR
P.O. Box 51
N-2007 Kjeller, NORWAY

FOREIGN (Others)

Dr. Peter Basham
Earth Physics Branch
Geological Survey of Canada
1 Observatory Crescent
Ottawa, Ontario, CANADA K1A 0Y3

Dr. Eduard Rerg
Institute of Geophysics
University of Hawaii
Honolulu, HI 96822

Dr. Michel Bouchon
I.R.I.G.M.-B.P. 68
38402 St. Martin D'Herès
Cedex, FRANCE

Dr. Hilmar Bungum
NTNF/NORSAR
P.O. Box 51
N-2007 Kjeller, NORWAY

Dr. Michel Campillo
Observatoire de Grenoble
I.R.I.G.M.-B.P. 53
38041 Grenoble, FRANCE

Dr. Kin Yip Chun
Geophysics Division
Physics Department
University of Toronto
Ontario, CANADA M5S 1A7

Dr. Alan Douglas
Ministry of Defense
Blacknest, Brimpton
Reading RG7-4RS, UNITED KINGDOM

Dr. Roger Hansen
NTNF/NORSAR
P.O. Box 51
N-2007 Kjeller, NORWAY

Dr. Manfred Henger
Federal Institute for Geosciences & Nat'l Res.
Postfach 510153
D-3000 Hanover 51, FRG

Ms. Eva Johannisson
Senior Research Officer
National Defense Research Inst.
P.O. Box 27322
S-102 54 Stockholm, SWEDEN

Dr. Fekadu Kebede
Seismological Section
Box 12019
S-750 Uppsala, SWEDEN

Dr. Tormod Kvaerna
NTNF/NORSAR
P.O. Box 51
N-2007 Kjeller, NORWAY

Dr. Peter Marshal
Procurement Executive
Ministry of Defense
Blacknest, Brimpton
Reading FG7-4RS, UNITED KINGDOM

Prof. Ari Ben-Menahem
Department of Applied Mathematics
Weizman Institute of Science
Rehovot, ISRAEL 951729

Dr. Robert North
Geophysics Division
Geological Survey of Canada
1 Observatory Crescent
Ottawa, Ontario, CANADA K1A 0Y3

Dr. Frode Ringdal
NTNF/NORSAR
P.O. Box 51
N-2007 Kjeller, NORWAY

Dr. Jorg Schlittenhardt
Federal Institute for Geosciences & Nat'l Res.
Postfach 510153
D-3000 Hannover 51, FEDERAL REPUBLIC OF
GERMANY